The Dissertation Committee for David Nien Kwong Certifies that this is the approved version of the following dissertation:

Towards Two Dimensional Optical Beam Steering with silicon Nanomembrane-Based Optical Phased Arrays

Committee:

Ray T. Chen Supervisor

Seth Bank

Zheng Wang

Gary Hallock

Fabian Pease

Towards Two Dimensional Optical Beam Steering with silicon Nanomembrane-Based Optical Phased Arrays

by

David Nien Kwong, B.S.E.E.; M.S.E.E.

Dissertation

Presented to the Faculty of the Graduate School of

The University of Texas at Austin

in Partial Fulfillment

of the Requirements

for the Degree of

Doctor of Philosphy

The University of Texas at Austin

August 2013

Acknowledgements

I'd like to thank my advisor, Professor Ray T. Chen, for his continuous support and guidance throughout my graduate studies, without which none of this would be possible. I will always be thankful for his advice, and the doors it has opened for me. I also thank my committee members, Professor Fabian Pease, Dr. Seth Bank, Dr. Zheng Wang, and Dr. Hallock for serving on my committee, and their invaluable support and advice on my dissertation.

Many thanks to my colleagues here in the Optical Interconnect Group at the University of Texas at Austin for all their help. Special thanks to Amir Hosseini and John Covey for their technical guidance and collaborations, being great mentors and helping me to excel in my graduate studies. Many thanks also to Yang Zhang and Xiaochuan Xu in their valuable discussions and countless hours in the cleanroom with me.

Finally, I would like to express my gratitude to my family for their love and support throughout my life. Without their constant encouragement and sacrifice, I would not be who I am today.

Towards Two Dimensional Optical Beam Steering with silicon Nanomembrane-Based Optical Phased Arrays

David Nien Kwong, PhD

The University of Texas at Austin, 2013

Supervisor: Ray T. Chen

Silicon based on-chip optical phased arrays are an enabling technology to achieving agile and compact large angle beam steering. In this work, a single layer array is presented, and approaches to multilayer 3D photonic integration for achieving a 2D array are also discussed. Finally, two dimensional optical beam steering is achieved using both thermo-optic and wavelength tuning. Various structures are considered as an alternative to the conventionally used shallow etched surface gratings to achieve narrow beam widths in the far field along with low switching power. The corrugated waveguide interspersed with 2D photonic crystal for crosstalk suppression is presented as a novel structure for coupling to free space that can provide lithographically defined index contrast in a single fabrication step, along with the smallest beam widths presented to date, at 0.25°. In addition, a polysilicon overlay with an oxide etch stop layer on top of a silicon waveguide is also presented as a grating coupler that achieves narrow far field beam widths. With this structure, two dimensional steering of 20° X 15° is demonstrated with a 16 element optical phased array, with a beam width of 1.2° X 0.4° and maximum power consumption of 20mW per channel.

Table of Contents

Table of Contents vi

List of Figures ix

Chapter 1: Research goals 1

Optical Phased Array for Optical Beam Steering 1

Chapter 2: Design of Optical Circuit 7

Design and Optimization of MMI 8

Design and Optimization of an Unequally Spaced OPA 12

Passive and Active Phase Shifting 14

Summary 16

References 17

Chapter 3: 1x12 Even fanout using multimode interference optical beam splitter on silicon nanomembrane 18

Introduction 18

MMI Design 19

Device Fabrication 20

Results and Discussion 21

Summary 22

References 23

Chapter 4: 1x12 Unequally-spaced Waveguide Array for Actively-tuned Optical Phased Array on a Silicon Nanomembrane 24

Introduction 24

Non-Uniform Array Design 25

Device Fabrication 29

Experimental Results and Discussion 31

Summary 34

References 35

Chapter 5: Multilayer Silicon Nanomembranes-Amorphous Silicon 37

Introduction to Amorphous Silicon Photonics 37

Single Layer Amorphous Silicon Characterization 39
Multilayer Amorphous Silicon Structures 42
Summary 46
References 48

Chapter 6: Low Loss Polycrystalline Silicon Waveguides and Devices for Multilayer On-Chip Optical Interconnects 50
Introduction to Polysilicon Photonics 50
Design and fabrication 52
Results and Analysis 57
Summary 61
References 62

Chapter 7: Subwavelength grating couplers on SOI for Fiber-to-chip Coupling with SU-8 Top Cladding 64
Introduction: Coupling to Nanophotonic Circuits 64
Design of a Subwavelength Grating Coupler 65
Results and Discussion 68
References 69

Chapter 8: Corrugated Waveguide based Optical Phased Array with Crosstalk Suppression using 2D Photonic Crystal 70
Introduction 70
Design of Photonic Components 71
Far Field Imaging Results and Discussion 78
Summary 82
References 83

Chapter 9: Two Dimensional Beam Steering Using a Silicon Optical Phased Array with Polycrystalline Silicon Overlay 84
Introduction 84
Design 85
Fabrication 87
Experimental Results and Discussion 89

Summary 95
References 95
Chapter 10: Summary and Future Work 97
Bibliography 101
Publications 106
Journal Papers: 106
Conference Papers: 107

List of Figures

Figure 1-(a) A general schematic of a 1-D optical phased array and (b) Far field pattern when N=9. 4

Figure 2-Maximum steering angle and center to center pixel spacing for recent OPAs, as well as our proposed OPA. 5

Figure 3-Schematic of full device including optical circuit, and thermo-optic phase shifting heaters on top of the oxide cladding. 7

Figure 4-Optical circuit schematic and passive components. 8

Figure 5-Schematic of a 1-by-N symmetric MMI coupler for even N 10

Figure 6- Output phase profile of a 6 port MMI coupler comparing the analytical closed form formula, a Si/SiO2 simulation, and a low index polymer ZPU12-RI MMI. 11

Figure 7- BeamPROP simulation of 1x12 MMI beam splitter showing equal power distribution at the single mode output after tapering. 12

Figure 8-(a) Equally spaced array and (b) unequally spaced array composed of equally spaced sub-arrays. 14

Figure 9-(a) Schematic of thermo-optic heater structure, along with (b) cross section view. 15

Figure 10-(a) Cross-sectional temperature profile of single activated channel in OPA and (b) transient simulation showing the response time to raise the silicon waveguide to reach the temperature for 2π phase shift. 16

Figure 11-(a) Schematic of a 1XN MMI beam splitter. Inset is cross section schematic of the SOI based waveguiding structure. n_{Si}=3.47, n_{SiO2}=1.45, $n_{PECVD(SiO2)}$=1.46. (b) BeamPROP simulation of 1x12 MMI beam splitter showing equal power distribution at the single mode output after tapering. 20

Figure 12- Fabrication process flow (a) start with SOI wafer, (b)light oxidation for oxide etch mask, (c) e-beam lithography, (d) develop, (e) nickel deposition, (f) liftoff for pattern inversion, (g) RIE etch, (h) Piranha clean, (i) PECVD silicon dioxide deposition. 21

Figure 13-(a) Top down SEM picture of 1x12 MMI at the input. (b) Tilted view of the entire MMI. (c) Intensity profile of 12 channel MMI output with top down near field imaging. 22

Figure 14-(a) A schematic of the silicon waveguide based optical phased array. (b) Beam propagation simulation of the photonic circuit. 27

Figure 15-(a) 12-element non-uniform array design with 3 sub-arrays of single-mode silicon waveguides embedded in silicon dioxide, with dimensions of a single waveguide shown in the inset. (b) Theoretical far-field pattern for a non-steered and a steered beam inside the planar guide. The envelope is the far field pattern of a single silicon waveguide embedded in silicon dioxide.....28

Figure 16-(a) Tilted SEM view of the unequally spaced OPA output and silicon nanomembrane planar guide. (b) Optical microscope picture of the 12 thermo-optic heaters with bonding pads. 30

Figure 17-(a) SEM cross section of a heater over its waveguide. (b) COMSOL Multiphysics simulation of the thermal profile of the microheater and waveguide cross section with bread loafing of the oxide. 31
Figure 18- Far field characterization, (a) simulated and measured steering angle versus maximum power per channel. Effective steering angles in free space are determined from measurement data. (b) Power efficiency versus steering angle, (c) side-lobe-level versus steering angle. 33
Figure 19-Propagation loss determined by varying singlemode waveguide lengths.41
Figure 20-Top down near field image of the 12 MMI outputs fabricated on amorphous silicon. 42
Figure 21-Schematic of a multilayer amorphous silicon stack. 43
Figure 22-Cross sectional SEM image of a two layer amorphous silicon structure with interlayer PECVD oxide. 44
Figure 23-5 layer structure of planar slab waveguides formed with amorphous silicon. 45
Figure 24-a) SEM cross section and b) photograph of the completed 5 layer amorphous silicon chip with slab waveguides. 45
Figure 25-a) IR image of the 5 layer amorphous silicon device, with the bottom layer coupling shown. 46
Figure 26-Beam Propagation Method simulation of 10μm waveguide for (a) crystalline silicon and (b) polysilicon with grain boundaries. 54
Figure 27-(a) Schematic of waveguide structure. Not drawn to scale. (b) Schematic of 1x12 polysilicon MMI. 55

Figure 28-(a) Top down SEM image of polysilicon grains after oxidation and BOE, (b) cross sectional SEM of a single mode polysilicon waveguide and (c) microscope image of the completed 1x12 MMI. 56

Figure 29-Propagation loss of various polysilicon and crystalline silicon waveguide widths.. Standard error bars are given for each data measurement. .57

Figure 30-(a) Schematic of experimental setup using an IR CCD to examine the far field emission of the grating coupler. (b) Far field image of a crystalline waveguide and grating. (c) Far field image of polysilicon waveguide and grating identical to that made of crystalline silicon. 59

Figure 31-(a) IR image of the 12 output spots from 1x12 MMI fanout. (b) Output intensities of the 1x12 polysilicon MMI. 61

Figure 32-(a) Schematic of fiber coupling to SWG coupler. (b) Top down schematic of SWG coupler with parameters. (c) Cross sectional schematic of our grating coupler stack. The handle silicon layer is not shown here. ..66

Figure 33-(a) Contour plot of varying grating period and n_{SWG} simultaneously to optimize the power emitted upwards. (b) Varying n_{SWG} with different silicon thicknesses. (c) Effect of BOX thickness on power emitted upwards. 67

Figure 34-(a) SEM image of the SWG coupler region. (b) Setup for testing our grating with 4 degrees of freedom. (c) Output spectrum of a single SWG grating. 69

Figure 35-(a) Schematic of the grating coupled 16 element optical phased array consisting of corrugated waveguides separated by 2D photonic crystal. (b) Closeup view of the subwavelength grating coupler. (c) Closeup of the corrugated waveguides with 2D photonic crystal isolation. 72

Figure 36-(a) Schematic of a single corrugated waveguide with period Λ and widths w_1 and w_2. (b) E_x field profile of a corrugated waveguide emission from a 3D FDTD simulation. (c) Contour plot of the differences in effective index between different values of w_1 and w_2 for the fundamental TE mode.....75

Figure 37-(a) 2D FDTD simulation of 2 corrugated waveguides spaced 4μm apart showing optical crosstalk between the excited waveguide on top and the waveguide on bottom via grating assisted coupling. (b) Transmission spectrum of a plane wave through 5 periods of the 2D photonic crystal slab, with inset showing the band diagram. (c) 2D FDTD simulation of the same structure but with 5 periods of 2D PC between the two corrugated waveguides showing effective crosstalk suppression.....78

Figure 38-Top down SEM of the corrugated waveguide OPA (a) without and (b) with the 2D PC in between array elements. (c) Top down SEM of the input subwavelength grating coupler and (d) the input grating's transmission spectrum.....79

Figure 39-(a) IR CCD image of the far field of a single corrugated waveguide as the wavelength is tuned from 1480nm to 1580nm in 10nm steps. (b) Elevational beam profiles of the steered beam at different wavelengths. (c) Steered angle and FWHM beam width of the corrugated waveguide grating at different wavelengths.....80

Figure 40-Far field of the 16 element corrugated waveguide array (a) without and (b) with 2D PC crosstalk suppression. (c) Azimuthal and elevational beam profiles of the far field with 2D PC. 82

Figure 41 a) Schematic (not to scale) of the overall device. (b) Schematic and (c) SEM of a single waveguide grating with polysilicon overlay and oxide etch stop layer. 86

Figure 42 -(a) Top down SEM of the subwavelength grating coupler. Insets show magnified view (top right) and cross sectional view with oxide cladding (bottom left). (b) Microscope picture of the completed device. (c) Picture of the wirebonded device on the chip carrier plugged into a simple breadboard. 89

Figure 43-(a) Coupling efficiency of the wideband subwavelength grating coupler. (b) Schematic of the testing setup used to achieve 2D beam steering using the OPA. (c) Photograph of the testing setup showing the razor blade to block reflected light from entering the IR CCD. 90

Figure 44- (a) IR CCD images of the single waveguide grating with polysilicon overlay as the wavelength is tuned from 1480nm to 1580nm. (b) Elevational beam profiles in θ of the steered beams. (c) Steering angle and FWHM beam width of the steered beam. 91

Figure 45- a) MZI transmission spectrum vs. electrical power to TO phase shifters. (b) Oscilloscope screenshot of MZI. 92

Figure 46-(a) OPA far field and (b) line profile without thermal tuning. (c) OPA far field and (d) line profile after thermal tuning. 93

Figure 47-(a) 2D beam steering around a 20° X 15° field of view with SLL better than 10dB, and beam widths of 1.2° X 0.5°. 94

Figure 48-2D beam steering around a 20° X 15° field of view with SLL better than 10dB, and beam widths of 1.2° X 0.5°. 94

Chapter 1: Research goals

This thesis will report the results of my research during the past few years as part of the Multidisciplinary University Research Initiative (MURI) program titled "Three Dimensionally Interconnected Silicon Nanomembranes for Optical Phased Array (OPA) and Optical True Time Delay (TTD) Applications." This program is collaborative effort between several research groups from three different universities, and is led by our group, Professor Ray Chen's Optical Interconnect Group. One of the major goals for this project is to realize an optical phased array (OPA) for use in large-angle (>45º) laser beam steering.

This thesis proposal will include the design, fabrication, and experimental results of a single layer silicon nanomembrane based optical phased array for large angle beam steering, as well as efforts towards developing three dimensionally integrated multi-layer silicon nanomembrane based platform. I will conclude with work to be completed in the next year. For the sake of completeness, I will also include discussions of the results of other team members. In this chapter I introduce the project and provide background information, as well as specify the project goals.

OPTICAL PHASED ARRAY FOR OPTICAL BEAM STEERING

Optical beam steering is an enabling technology in a wide range of applications, including optical interconnects and switches, laser printers, optical scanners [2], laser printers, bar code readers, and optical communications [1]. A variety of optical beam steering systems have been developed, including mechanical beam steering, micro-electro-mechanical (MEMS) beam steering, and optical phased array beam steering.

Mechanical beam steering systems have advantages in high light efficiency and large scanning field of view, but suffer from complex and costly high precision rotating stages, limited scanning speed (around ms), and sensitivities to acceleration and vibration which make them unsuitable for military applications . MEMS systems improve upon traditional mechanical systems in terms of power consumption, device size and scanning speed, but are still limited to scanning speeds in the μs to ms range [1].

Optical phased arrays make possible simple, affordable, lightweight, optical sensors offering very precise stabilization, inherently random-access pointing, programmable multiple simultaneous beams, and good optical power handling capability [3]. Compared to their microwave counterparts, optical phased arrays steer a beam that is already formed instead of generating a beam and then steering it. This makes optical phased arrays passive devices, which consists solely of phase shifters, resulting in beam steering [3].

Consider a one-dimensional phased array as shown in Figure 1(a), where each phase element propagates uniformly in all directions and the amplitude is the same for all phase elements as well. Along the plane A-A', the phase difference between adjacent phase elements can be written as $\Delta\Phi = \frac{2\pi}{\lambda} d \sin\theta_0$ where d and λ refer to the separation between adjacent phase elements and the operating wavelength, respectively. In this case, the total complex far field can be simply written as

$$E(\theta) = \frac{\sin\left[\frac{\pi N d}{\lambda}\left(\sin\theta - \sin\theta_0\right)\right]}{\sin\left[\frac{\pi d}{\lambda}\left(\sin\theta - \sin\theta_0\right)\right]} \tag{1}$$

where N is the total number of phase elements in the array. Then, the intensity as a function of angle, θ, in the far field becomes

$$I(\theta) = |E(\theta)|^2 = \left|\frac{\sin\left[\frac{\pi N d}{\lambda}\left(\sin\theta - \sin\theta_0\right)\right]}{\sin\left[\frac{\pi d}{\lambda}\left(\sin\theta - \sin\theta_0\right)\right]}\right|^2 \tag{2}$$

Figure 1(b) shows a sample far field pattern of such an array with N=9. From this a few important points can be observed. First, the direction of the main lobe is at $\theta=\theta_0$, and by controlling the phase distribution among the phase elements, the direction of the main lobe can be tuned and the beam can be steered. In addition to side lobes around the main lobe, there are also grating lobes. These grating lobes occur when the denominator of Equation (2) vanish [1], that is, where

$$\frac{\pi d\left(\sin\theta - \sin\theta_0\right)}{\lambda} = \pm\pi, \pm 2\pi, \pm 3\pi \ldots \tag{3}$$

For the first grating lobe of $\pm\pi$ to be positioned at the horizon (or when $\theta=90^o$ or $\theta=-90^o$) it can be seen that

$$\frac{d}{\lambda} = \frac{1}{1+\left|\sin\theta_0\right|} \tag{4}$$

From Equation (4), this means that the separation between array elements should not be greater than half the wavelength. While this condition is easily satisfied in the

microwave region of the spectrum due to the long wavelength, at near IR wavelengths this is difficult to realize because optical waveguides cannot support modal sizes smaller than half the wavelength [6]. At such spacing, optical coupling between adjacent waveguides occurs, which causes far field pattern distortion [1].

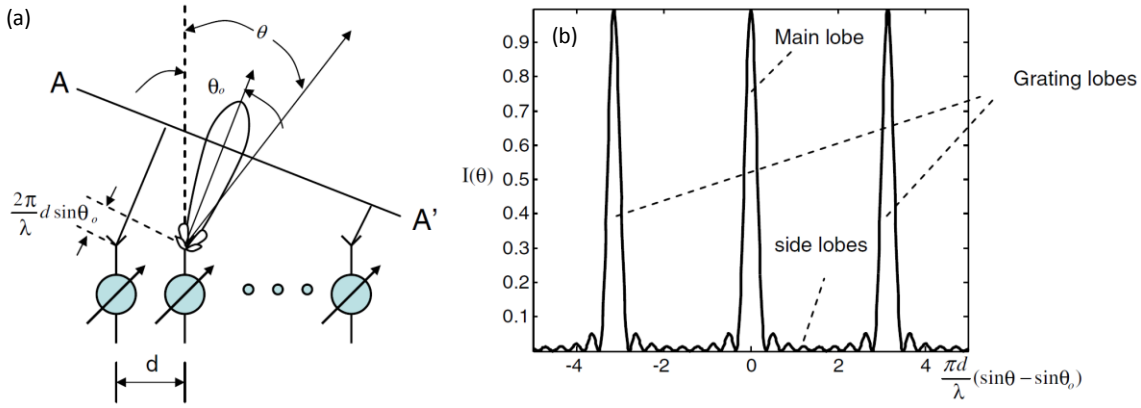

Figure 1-(a) A general schematic of a 1-D optical phased array and (b) Far field pattern when N=9.

The earliest optical phased array beam steering systems were first developed by Meyer in 1971, when he used bulk, lithium tantalite phase shifters in a 46 element array [4]. Shortly afterwards, Ninomiya also demonstrated a 1-D array of lithium niobate electro-optic prism deflectors [5]. In addition, liquid crystal modulators have been pioneered by Paul Mcmanamon, but are not suitable for large angle and high speed (~GHz) high performance applications. Figure 2 below summarizes the recent developments in optical beam steering in terms of maximum steering angle, as well as our proposed OPA. In chapter 2, I briefly review the theory and design from my colleague Amir Hosseini for a single stage optical beam steering system based on optical phased arrays that provides for large steering angle.

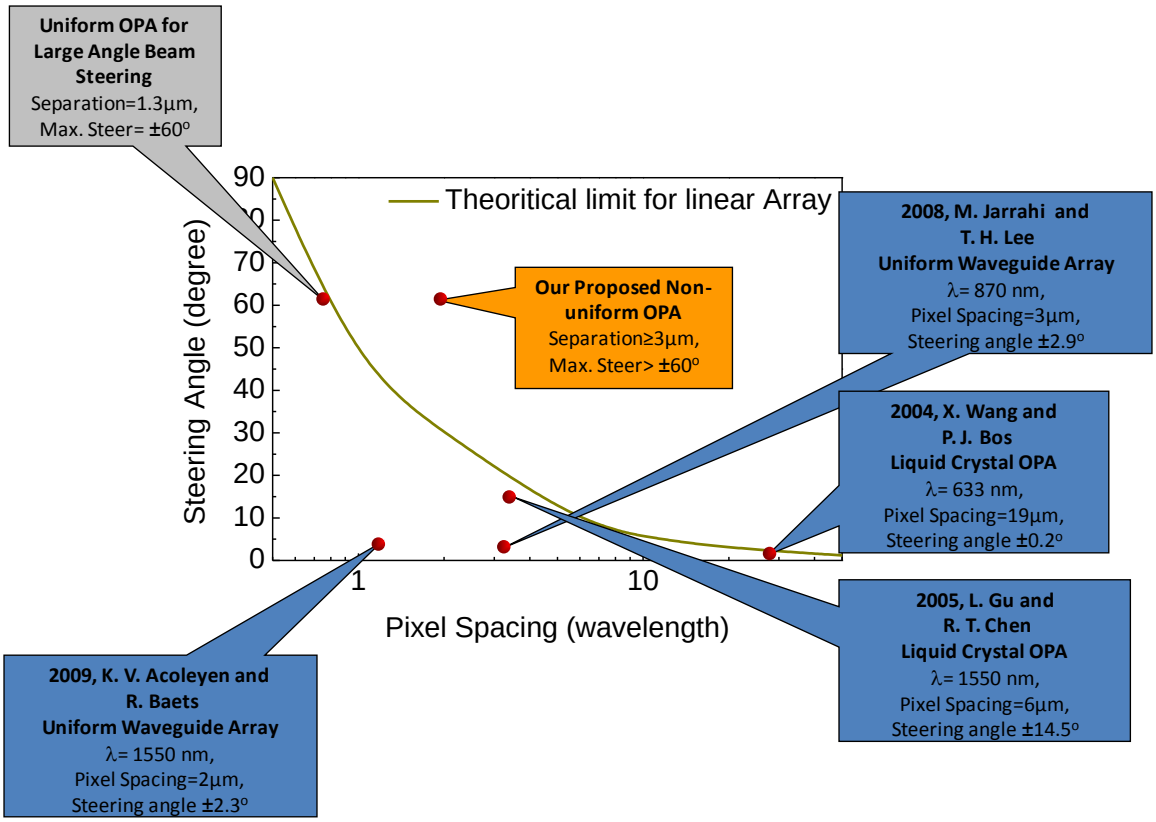

Figure 2-Maximum steering angle and center to center pixel spacing for recent OPAs, as well as our proposed OPA.

A common way to implement an OPA is to use a 1XN coupler to evenly split an optical beam into the desired number of channels, which are then phase modulated, and radiated from the output. It is necessary to know the exact phase profile of the optical beam splitter to determine the amount of active phase modulation needed. Multi-mode interference (MMI) couplers are a common device used to achieve optical beam splitting. While the power distribution at the output ports has been thoroughly investigated, few investigations concerning the phase profile at the MMI output have been performed, but this knowledge is important in beam steering applications because this determines the

amount of active phase shift required. The output phase profile of MMI couplers has been theoretically investigated by my colleague Amir Hosseini and is briefly presented in chapter 2. My technique to achieve active phase modulation is also presented in chapter 2.

Chapter 3 discusses the fabrication and experimental results of a 1x12 multimode interference coupler that provides 12 coherent inputs to the optical phased array. In chapter 4, a single layer silicon nanomembrane based 1x12 optical phased array is presented, by combining the 1x12 MMI with the rest of the photonic circuit, as well as thermo-optic phase shifters. The OPA is tested and experimentally characterized. Chapters 5 and 6 are devoted to amorphous and polysilicon, respectively, and contain my work on realizing multi-layer photonic structures. In chapter 7, a subwavelength grating coupler is presented, and grating couplers in general are discussed for use in optical phased arrays. Chapter 8 summarizes my work, and provides a brief discussion for future work.

Chapter 2: Design of Optical Circuit

In this chapter I will introduce the design of our optical circuit, as done by my colleague Amir Hosseini. I will discuss my contribution for the design of the thermo-optic active phase shifters as well.

Our beam steering device consists of two layers; the first layer contains the passive optical circuit and the second layer is composed of the thermo-optic active phase shifters. These two layers are separated by an oxide cladding layer to prevent loss that would occur from the penetration of the evanescent electromagnetic tail into the metal phase shifter, as shown in Figure 3. Figure 4 shows the optical circuit which consists of the multi-mode interference (MMI) splitter, the s-bend waveguides, and the unequally spaced OPA itself. We have simulated the performance of such an OPA fabricated on SOI wafer [6]. This OPA is fed by a MMI coupler that splits the input signal.

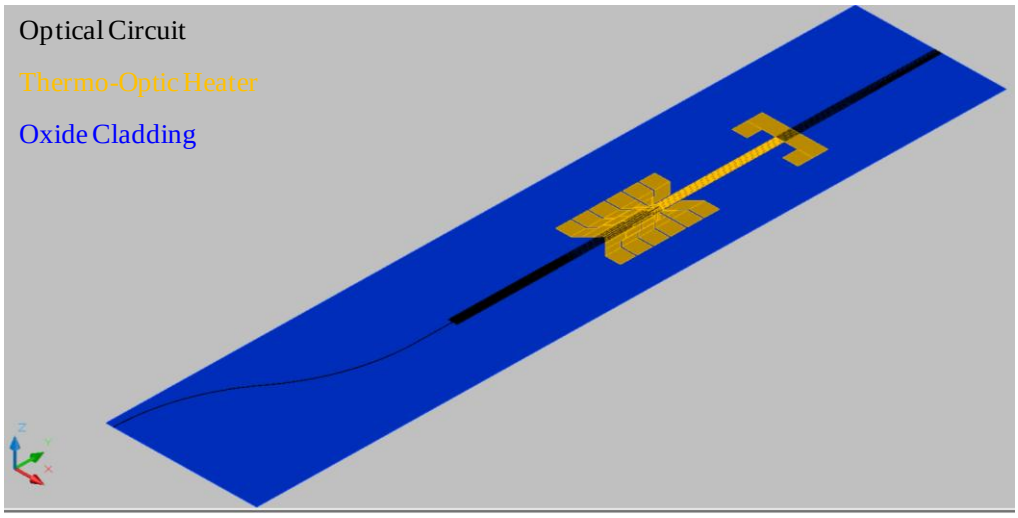

Figure 3-Schematic of full device including optical circuit, and thermo-optic phase shifting heaters on top of the oxide cladding.

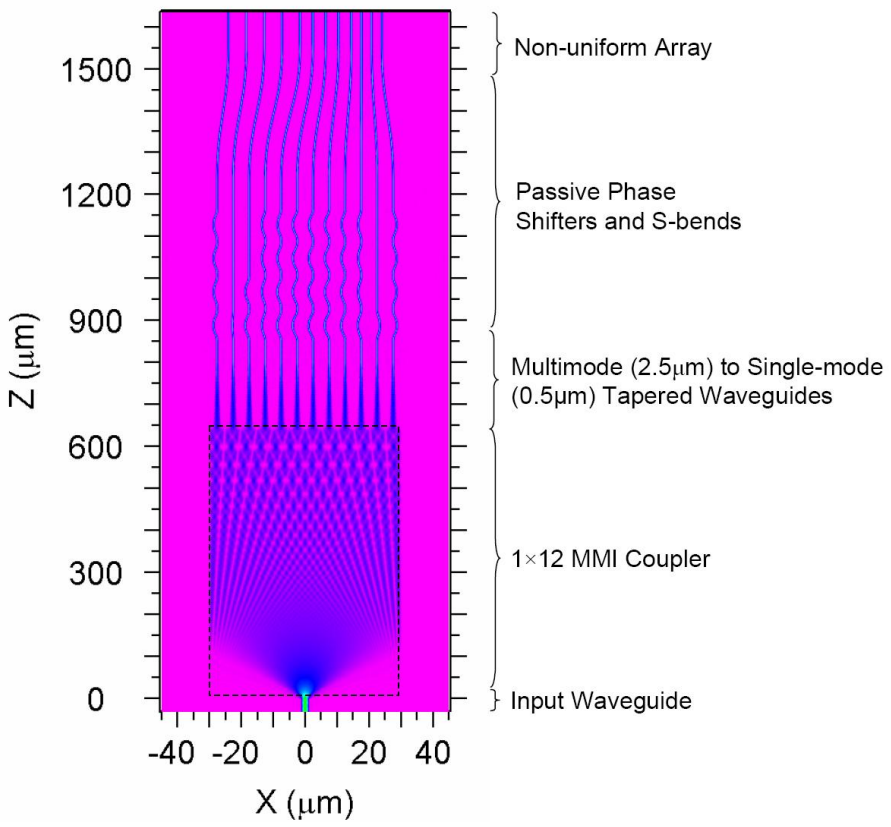

Figure 4-Optical circuit schematic and passive components.

DESIGN AND OPTIMIZATION OF MMI

Multi-mode interference couplers are widely used in photonic integrated circuits (PICs) as power splitters, optical switches, and for other signal routing processes [7]. This is due to the significant advantages that MMI couplers provide through their compact size, low loss, stable splitting ratio, low crosstalk, and imbalance, large optical bandwidth, insensitivity to polarization, ease of production, and good fabrication tolerances [7]. As one of the largest uses of MMI couplers is for power splitters, the power distribution at the output ports has been thoroughly investigated. However, very little is understood about the phase profile at the MMI output, but this knowledge is important in beam steering applications because it determines the amount of active phase

shift required. My colleague Amir Hosseini has derived an analytical closed loop expression for the phase shift at each of the output ports for a 1-by-N MMI coupler [8]. Here I briefly introduce his findings for the sake of completeness.

MMI couplers operate based on the phenomenon of self-imaging in multi-mode waveguides, whereby an input field profile is reproduced in single or multiple images at periodic intervals along the propagation direction of the guide [8]. From Figure 5, the multimode waveguide consists of a core with refractive index n_c and width W, and has N output ports. The multimode section can support a maximum of M+1 modes. For each mode *p*, the dispersion relation is given as

$$\beta_p^2 + \kappa_{yp}^2 = \left(\frac{2\pi n_c}{\lambda_0} \right)^2, \tag{5}$$

where, β_p is the propagation constant of the the pth mode, λ_0 is a free-space wavelength. κ_{yp} is the lateral wavenumber of the pth mode, given as $\kappa_{yp} = (p+1)\pi/W_e$, where W_e is the effective width for mode m including the penetration depth due to the Goose-Hahnchen shift [2]. The propagation constant β_p can be approximated as

$$\beta_p \approx \beta_0 - \frac{p(p-2)}{3L_\pi}, \tag{6}$$

where, $L_\pi = \pi/(\beta_0 - \beta_1) \approx 4n_c W_e^2/3\lambda_0$. Furthermore, each mode accumulates phase according to its own propagation constant, and the field profile at z=L can be written as

$$\begin{aligned} &\exp(-j\beta_0 L)\sum_{p=0}^{M} c_p \phi_p(y) \exp\left(-j(\beta_p - \beta_0)L\right) \approx \\ &\exp(-j\beta_0 L)\sum_{p=0}^{M} c_p \phi_p(y) \exp\left(j\frac{p(p+2)\pi}{3L_\pi}L\right). \end{aligned} \tag{7}$$

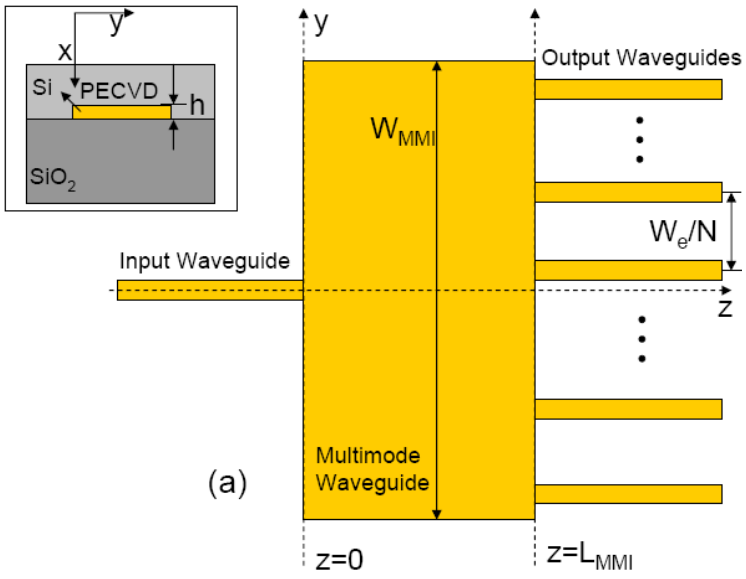

Figure 5-Schematic of a 1-by-N symmetric MMI coupler for even N

At $L = 3rL_\pi$ with r =1, 2, ..., all the exponential terms in the previous equation become in-phase with one another and a single image of the input field profile is formed. Generally, an N-fold image of the input field profile is formed at $L = 3L_\pi/N$. However, by using a symmetric input fed to the center of the multi-mode waveguide, a 4X reduction in the required length of the coupler can be achieved, so that $L = 3rL_\pi/4N$ [8].

For 1-by-N couplers, ideally the ouput power is to be divided equally among the output ports, and thus the field amplitude should be $1/\sqrt{N}$ $\sqrt{N}$. However, the approximation for the propagation constant β_p becomes inaccurate in reality, especially for the higher order modes in low-refractive-index contrast waveguides. This results in an error in the accumulated phase shift of each mode. These modal phase errors are the main cause of non-uniformity in the ouput field amplitudes and output intensity. These errors are more pronounced in low-refractive index contrast waveguides, such as a MMI made of the polymer ZPU12-RI which has a low refractive index contrast [8], and can be seen

in Figure 6. In choosing silicon as our core material, we are able to avoid this error and provide good confinement for the electric field at λ=1.55μm.

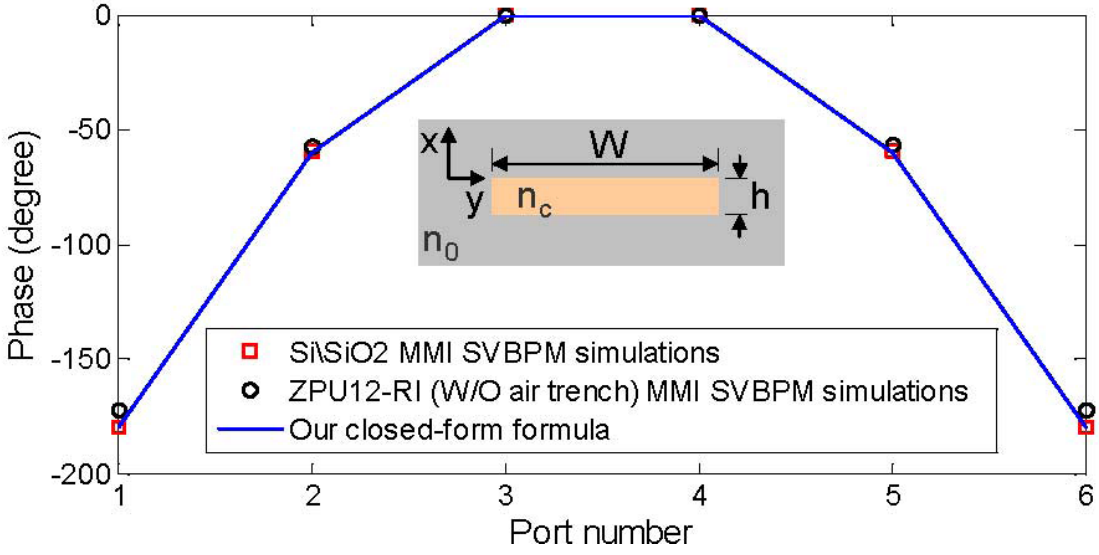

Figure 6- Output phase profile of a 6 port MMI coupler comparing the analytical closed form formula, a Si/SiO2 simulation, and a low index polymer ZPU12-RI MMI.

When we fix the width of the MMI W_{MMI}=60μm, the theoretical prediction of the MMI length is L_{MMI}=553.4μm. We have also chosen the input waveguide width, and hence the output waveguide width as well, to be W_W=2.6μm. At this width, the modal phase errors are greatly reduced, thereby enhancing the output uniformity of our MMI. This technique of optimizing the input and output waveguide width to improve the uniformity of MMIs with large N will be published separately and is forthcoming. The waveguide thickness is only 230nm. We performed a simulation of our MMI device using Rsoft's BeamPROP software based on the beam propagation method to determine its performance. As can be seen from Figure 7, our simulation shows good output uniformity when using TE polarized light at 1550nm, and confirms our theoretical prediction of the MMI length.

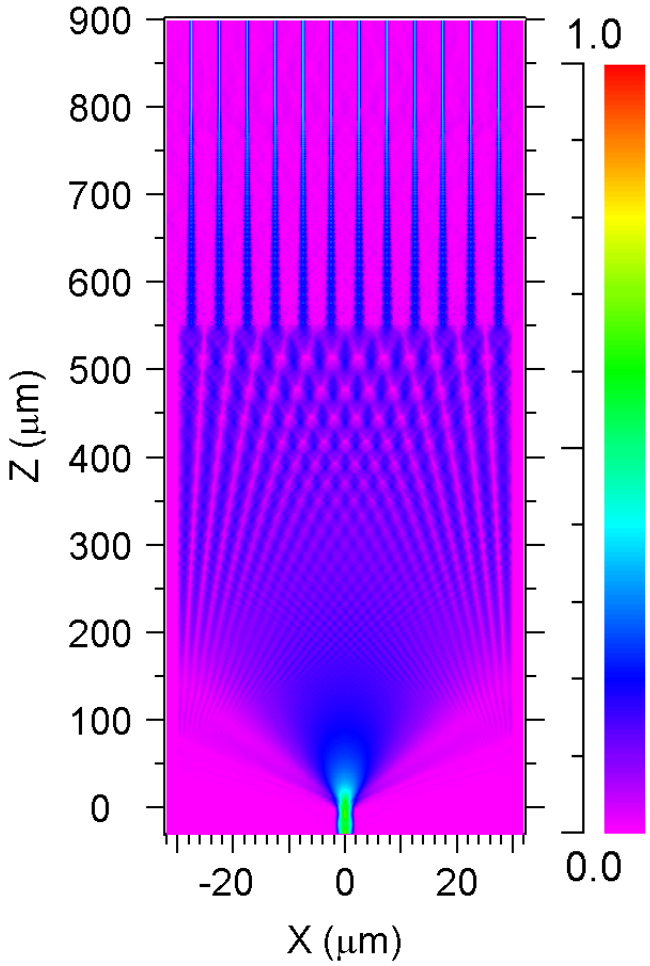

Figure 7- BeamPROP simulation of 1x12 MMI beam splitter showing equal power distribution at the single mode output after tapering.

DESIGN AND OPTIMIZATION OF AN UNEQUALLY SPACED OPA

Optical phased arrays are simply arrays of single-mode waveguides operating at the designated wavelength. Beam steering can be achieved by modulating the phase shift of each waveguide element in the array. To achieve wide steering angles in a uniform array, the waveguide spacing must be reduced to half the wavelength but this result in optical coupling between adjacent waveguides which causes far field pattern distortion.

This has the effect of increasing the side lobe level and thus reducing the power and steering efficiency [6]. A solution is to use an unequally spaced OPA that can relax this half-wavelength requirement. We have previously proposed a design methodology that provides both large angle steering while minimizing the side lobe level caused by optical cross-talk.

Our non-uniform array is realized by placing sub-arrays of equally spaced arrays next to each other, as can be seen in Figure 8(b). Our design methodology is as follows and uses the following definitions:

- N=total number of array elements
- M=number of sub-arrays
- s_i=spacing in sub-array i, for i=1,2,3…
- $s_i=q_i s_0$
- $s_0=\lambda/2$
- q_i is the smallest integer such that the $\gcd(q_i,q_j)=1$ where $i\neq j$

It is important to note that s_0 must be less than $\lambda/2$ so that sub-array grating lobes will not overlap. With this design methodology, the main lobes of each sub-array add up constructively, while there is no overlap between the grating lobes of each sub-array [6]. Our implementation of this design is an array with N=12 elements, which is comprised of M=3 subgroups each with 4 equally spaced elements. The array spacing is as follows:

- λ=1.6µm and s_0=0.8µm
- q_1=4, q_2=5, q_3=7, and s_1=3.2µm, s_2=4µm, s_3=5.6µm.

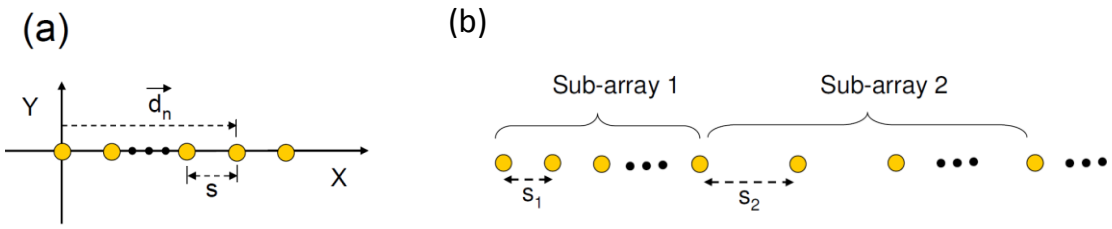

Figure 8-(a) Equally spaced array and (b) unequally spaced array composed of equally spaced sub-arrays.

PASSIVE AND ACTIVE PHASE SHIFTING

We desire to have an output beam that comes out straight, that is, at 0˚ steering, without any active phase shifting. To achieve this, it is necessary to equalize the phase of each output port by equalizing the optical path length with the use of additional s-bends. These s-bend segments serve the dual purposes of converting the equally spaced MMI output to the unequally spaced OPA, while at the same time passively equalizing the phase shifts at each of the MMI output ports.

Active phase shifting is achieved via the use of thermo-optic metal heaters that will utilize silicon's strong thermo-optic coefficient to modulate the refractive index and thereby the accumulated phase at the output of each array element. Our heater is essentially a metal wire whose temperature can be adjusted by changing the current through it. The heater is placed above the waveguide and is separated from the waveguide by a sufficiently thick oxide cladding layer to prevent optical absorption loss from the conductive metal.

In our design we have opted to make the heaters independently controllable; that is, we have (N+1) electrodes to provide for 12 heaters along with a common ground. This provides us the significant advantage of being able to reset after each 2π phase shift. Had we opted to simplify this electrical design by having only two electrodes, there would be

no reset and thus the phase shift required at the end of the array would be impractical to achieve.

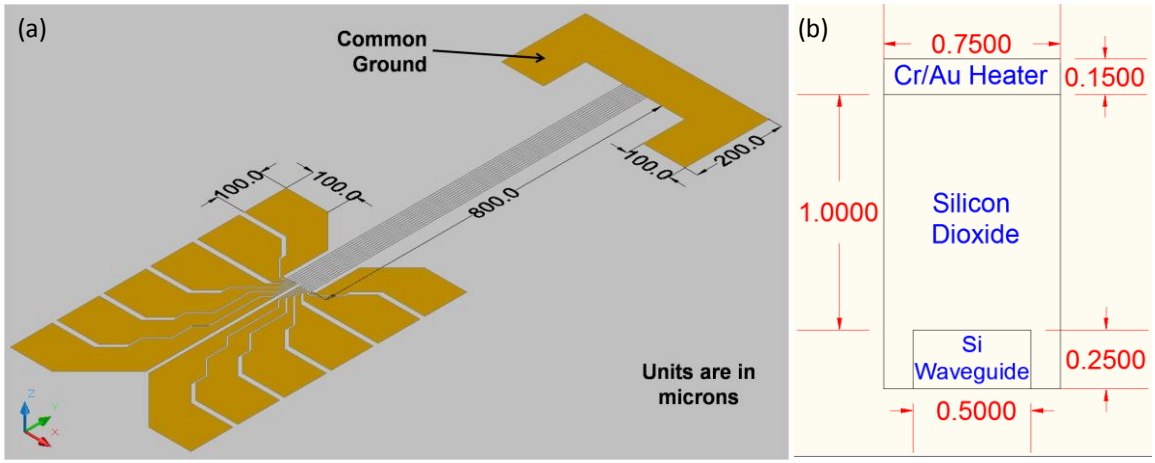

Figure 9-(a) Schematic of thermo-optic heater structure, along with (b) cross section view.

We have chosen the length of the heater region to be 800 μm and determined the necessary temperature change in the waveguide according to the equation below.

$$\Delta\phi = \frac{2\pi}{\lambda}\left(\frac{dn}{dT}\right)_{Si} \cdot \Delta T \cdot L_H \qquad (8)$$

where $\Delta\varphi$ is the desired phase shift of 2π, λ is the wavelength of light (1550nm), dn/dT is the thermo-optic coefficient of silicon (1.86E-4), ΔT is the temperature change in the waveguide, and L_H is the length of the heater. Thus, we need to raise the temperature of the silicon waveguide by 10.4 degrees.

Figure 9 shows the schematic layer structure of the heater, along with a cross sectional view. Figure 10(a) shows the thermal profile of an activated heater over a waveguide, while figure 10(b) shows the transient simulation of the response time necessary to achieve 2π phase shift.

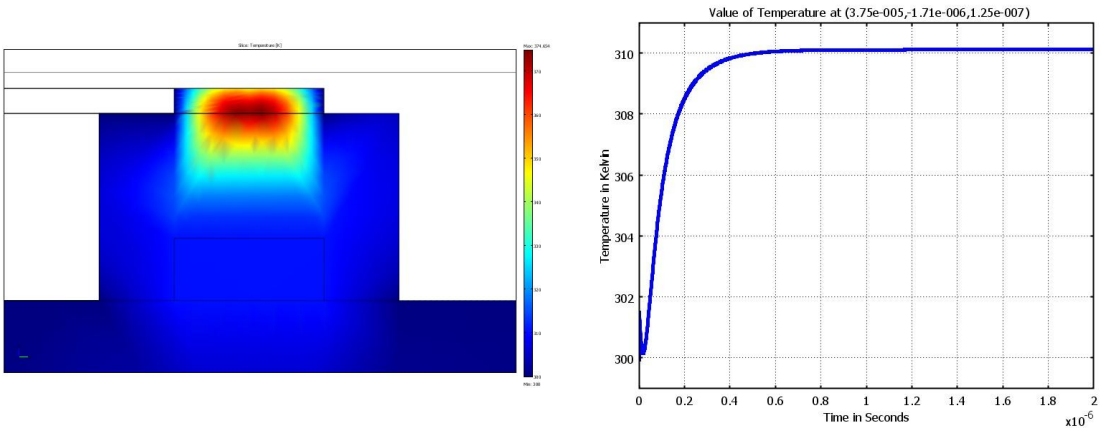

Figure 10-(a) Cross-sectional temperature profile of single activated channel in OPA and (b) transient simulation showing the response time to raise the silicon waveguide to reach the temperature for 2π phase shift.

SUMMARY

In this chapter I have introduced the design of our beam steering system. Our passive optical circuit consists of a 1x12 MMI coupler that acts as a beam splitter that feeds the OPA. S-bend waveguides equalize the output phase profile, as well as convert the equally spaced MMI output into our unequally spaced OPA output, so that under no excitation our beam is steered at 0º. Thermo-optic phase shifters have been designed to provide active phase shifting in which each array element can be independently controlled to enable large angle beam steering.

REFERENCES

[1] Stuart (Shizhuo) Yin, Jae Hun Kim, Fei Wu, Paul Ruffin, Claire (Fang) Luo, Ultra-fast speed, low grating lobe optical beam steering using unequally spaced phased array technique, Optics Communications, Volume 270, Issue 1, 1 February 2007, Pages 41-46.

[2] Jarrahi, Mona; Pease, R. Fabian W.; Miller, David A. B.; Lee, Thomas H.; , "Optical switching based on high-speed phased array optical beam steering," Applied Physics Letters , vol.92, no.1, pp.014106-014106-3, Jan 2008.

[3] McManamon, P.F.; Dorschner, T.A.; Corkum, D.L.; Friedman, L.J.; Hobbs, D.S.; Holz, M.; Liberman, S.; Nguyen, H.Q.; Resler, D.P.; Sharp, R.C.; Watson, E.A.; , "Optical phased array technology," Proceedings of the IEEE , vol.84, no.2, pp.268-298, Feb 1996

[4] R. A. Meyer, "Optical Beam Steering Using a Multichannel Lithium Tantalate Crystal," Appl. Opt. 11, 613-616 (1972)

[5] Ninomiya, Y.; , "Ultrahigh resolving electrooptic prism array light deflectors," Quantum Electronics, IEEE Journal of , vol.9, no.8, pp. 791- 795, Aug 1973

[6] Amir Hosseini, David N Kwong, and Ray T. Chen, Wide steering angle optical phased array based on silicon nano-membrane, Proc. SPIE 7221, 72210T (2009)

[7] Amir Hosseini, David N. Kwong, Che-Yun Lin, Beom Suk Lee, and Ray T. Chen, Output Formulation for Symmetrically-Excited one-to-N Multimode Interference Coupler, IEEE Journal of selected topics in quantum electronics, to appear (2010)

[8] L. Soldano and E. Pennings, “Optical multi-mode interference devices based on self-imaging: Principles and applications,” J. Lightw. Technol., vol. 13, no. 4, pp. 615–627, Apr. 1995.

Chapter 3: 1x12 Even fanout using multimode interference optical beam splitter on silicon nanomembrane

INTRODUCTION

Efficient optical beam splitters are a key component in photonic integrated circuits (PICs). Multimode interference (MMI) couplers have the advantage of compact size, low loss, stable splitting ratio, large optical bandwidth, and good fabrication tolerances [1,2]. One of the major applications of MMI couplers is power splitters. To date, high performance in output uniformity is difficult to achieve for MMIs with a large number of output ports N due to the modal phase errors, which have been shown to scale with N [3]. Acoleyen et al have shown a 16 port optical phased array but this is achieved by cascading 1x2 MMI couplers, thereby creating multiple stages of MMIs [4].

The majority of MMI couplers based on SOI have used a ridge waveguide structure. Until recently, few devices employing a strip waveguide structure for the input and output have been presented. Using strip waveguides, submicron cross-sectional areas of the waveguide core are possible while still maintaining single mode operation at 1550nm wavelength due to the large refractive index contrast between silicon (n_{Si}=3.5) and silicon dioxide (n_{SiO2}=1.45) which provides excellent light confinement. In addition, the strong lateral confinement of strip waveguides allows the bending radius to be shrunk down to micron range [5], whereas the slab region of ridge waveguides does not provide such confinement and thus requires large bending radius to achieve low loss propagation. Ultimately, the overall device size is increased by using ridge waveguides and this limits their use in ultra-compact photonic integrated circuits, such as on chip optical interconnects. In this paper, we demonstrate a single stage optical beam splitter with large number of outputs that avoids multiple insertion loss by using a 1x12 MMI on SOI with a

rib waveguide structure, which shows the smallest device size for a 1x12 waveguide beam splitter at a wavelength of 1550nm.

MMI DESIGN

MMI devices operate based on the phenomenon of self imaging in multimode waveguides whereby an input field profile is reproduced in single or multiple images at periodic intervals along the propagation direction of the guide [6,7]. From Figure 11(a), the multimode waveguide consists of a core with refractive index nc and width WMMI, length L_{MMI}, and N output ports. The MMI length is given as $L_{MMI}=n_{eff}W_e^2/\lambda_0 N$, which is $L_{MMI}=553.4\mu m$ for a $W_{MMI}=60\mu m$. Here, n_{eff} is the effective refractive index of the fundamental mode in the multimode section, W_e is the effective width including the penetration depth due to the Goose-Hahnchen shift, and λ_0 is the wavelength, which is 1550nm in this paper. The input/output access waveguide width is $W_W=2.6\mu m$. At this width, the modal phase errors are greatly reduced, thereby enhancing the output uniformity of our MMI. The derivation of the optimum MMI access waveguide width will presented separately. We performed a simulation of our MMI device using Rsoft's BeamPROP software based on the beam propagation. As can be seen from Figure 11(b), our simulation shows good output uniformity when using TE polarized light at 1550nm.

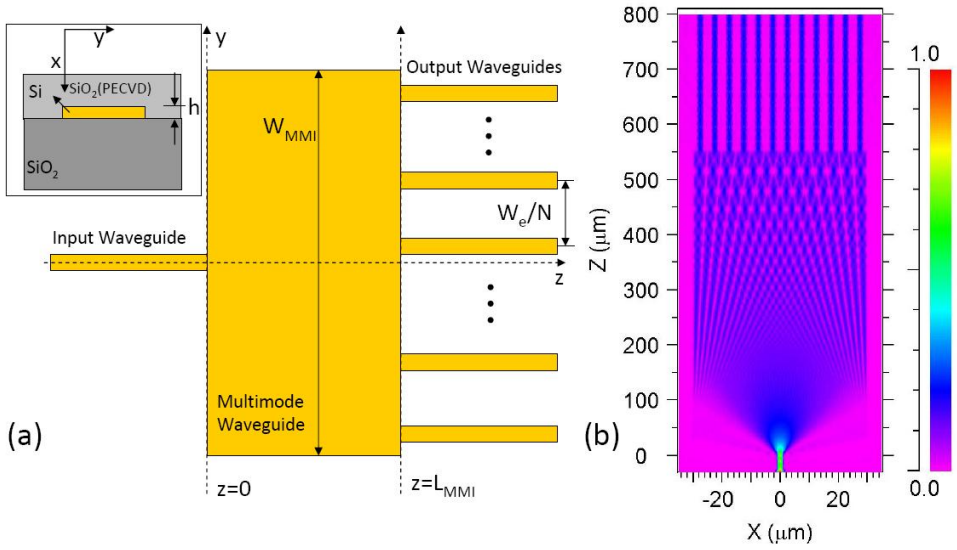

Figure 11-(a) Schematic of a 1XN MMI beam splitter. Inset is cross section schematic of the SOI based waveguiding structure. n_{Si}=3.47, n_{SiO2}=1.45, $n_{PECVD(SiO2)=}$1.46. (b) BeamPROP simulation of 1x12 MMI beam splitter showing equal power distribution at the single mode output after tapering.

DEVICE FABRICATION

We fabricated 1x12 MMIs (W_{MMI} =60μm, L_{MMI} =553.4μm) with W_W=2.6μm. The output waveguides were tapered down from 2.6μm to 0.5μm for single mode operation. The MMIs were fabricated on commercially available SOI from SOITEC with 3μm buried oxide layer (BOX) and 250nm top silicon layer. The silicon was first oxidized to create a 45nm thick top oxide layer which serves as a hard mask for the silicon etch. This oxidation consumes 20nm of silicon, leaving a final silicon thickness of 230nm.

The MMIs were patterned using a JEOL JBX600 electron beam lithography system. A nickel liftoff step was used to invert the pattern, and subsequently transferred to the top silicon layer via an HBr/Cl_2 based reactive ion etching (RIE). A subsequent piranha clean has the dual purpose of providing a clean sample, but more importantly, removing the nickel etch mask that would cause large absorption loss from penetration of the electromagnetic tail into the metal layer. A schematic of this process flow can be

found in Figure 12. SEM pictures of the fabricated 1x12 MMI at this stage can be seen in Figure 13(a) and (b). Afterwards, a 1μm film of plasma-enhanced chemical vapor deposition (PECVD) silicon dioxide was deposited using the Plasmatherm 790 system for top cladding as well as passivation. The refractive index of the PECVD Si02 film was found to be $n_{PECVD(Si02)}$=1.46.

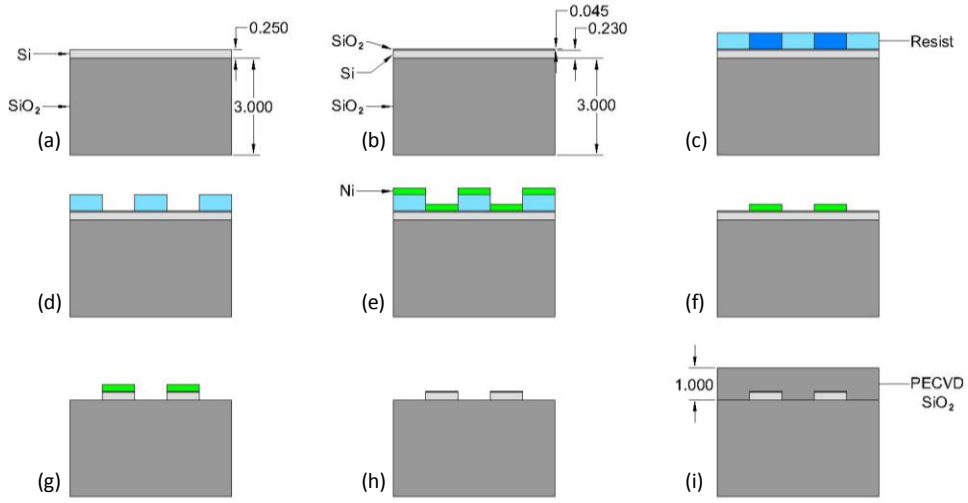

Figure 12- Fabrication process flow (a) start with SOI wafer, (b)light oxidation for oxide etch mask, (c) e-beam lithography, (d) develop, (e) nickel deposition, (f) liftoff for pattern inversion, (g) RIE etch, (h) Piranha clean, (i) PECVD silicon dioxide deposition.

RESULTS AND DISCUSSION

A six-axis automated aligner system with a 50nm precision in movement was used to couple TE polarized light at 1547nm from a polarization maintaining lensed fiber (PMF) with a 2.5μm output mode diameter into the input. A CCD camera connected to a variable objective lens captured the top-down near field images of the cleaved output waveguides' facets.

In order to clearly resolve the 12 spots in the near field image, a fanout design was used to increase the separation of each channel to 30μm. Figure 13(c) show the top

down intensity profile of the near field image. In addition, we used a single mode lensed fiber (SMF) to scan each output channel to determine the output power of each channel and evaluate the performance of our MMI. To determine the uniformity we used $10\log(I_{max}/I_{min})$, where I_{max} and I_{min} are the maximum and minimum intensities of the MMI output channels, respectively. The insertion loss of an MMI is defined as $-10\log[(\Sigma I_i)/I_{in}]$, where I_i is the intensity of each output channel, and I_{in} is the output power of a straight waveguide. The device has an insertion loss of 1.13dB, and a uniformity of up to 0.72dB.

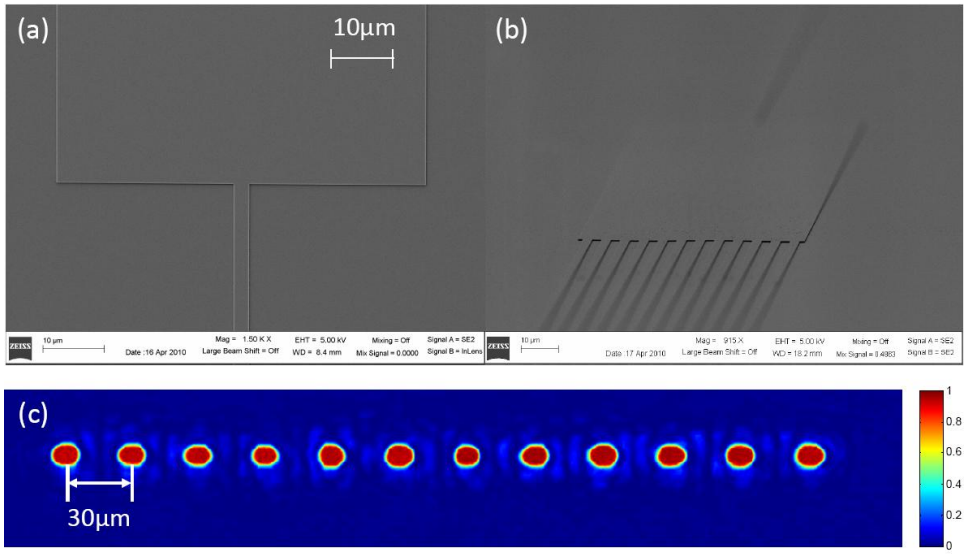

Figure 13-(a) Top down SEM picture of 1x12 MMI at the input. (b) Tilted view of the entire MMI. (c) Intensity profile of 12 channel MMI output with top down near field imaging.

SUMMARY

An optical beam splitter with a large number of outputs has been successfully demonstrated using a 1x12 MMI fabricated on a silicon nanomembrane on an SOI wafer

with a rib waveguide based structure. This MMI has high uniformity of 0.72dB and exhibits low loss of 1.13dB using TE polarized light.

REFERENCES

1 Rajarajan, M., Rahman, B. M. A., And Grattan, K. T. V.: 'Accurate Numerical Analysis of Multimode-Interference-Based 3-dB Couplers', Appl. Opt., 1998, 37, pp. 5672-5678

2 Ulrich, R., And Kamiya, T.: 'Resolution of self-images in planar optical waveguides', J. Opt. Soc. Am., 1978, 68, pp. 583-592

3 Huang, J.Z., Scarmozzino, R., And Osgood Jr., R.M.: 'A new design approach to large input/output number multimode interference couplers and its application to low-crosstalk WDM routers', IEEE Photonics Technology Letters IEEE, 1998, 10, 9, pp. 1292-1294

4 Acoleyen, K.V., Bogaerts, W., Jágerská, J., Le Thomas, N., Houdré, R., And Baets, R.: 'Off-chip beam steering with a one-dimensional optical phased array on silicon-on-insulator', Opt. Lett., 2009, 34, pp. 1477-1479

5 Vlasov, Y., And Mcnab, S.: 'Losses in single-mode silicon-on-insulator strip waveguides and bends', Opt. Express, 2004, 12, pp. 1622-1631

6 Soldano, L., And Pennings, E.: 'Optical multi-mode interference devices based on self-imaging: principles and applications', J. Lightwave Technology, 1995, 13, 4, pp. 615–627

7 Hosseini, A., Kwong, D.N., Lin, C.Y., Lee, B. S., And Chen, R.T.: 'Output Formulation for Symmetrically-Excited one-to-N Multimode Interference Coupler', IEEE Journal of Selected Topics in Quantum Electronics, 2010, 6, 1, pp. 53-60

Chapter 4: 1x12 Unequally-spaced Waveguide Array for Actively-tuned Optical Phased Array on a Silicon Nanomembrane

INTRODUCTION

Traditionally, optical beam steering has been achieved through mechanically controlled MEMS system [1] and liquid crystal (LC) based optical phased arrays (OPAs) [2-4]. While mechanical beam steering provides high steering efficiency and relatively large scanning angles, high precision rotating stages are required, which increase the device complexity and are not fast enough for high speed applications. LC OPAs are capable of beam steering without expensive and complex mechanical systems but suffer from low steering speed (~10ms) and limited steering angle (<10º) [4]. Also, increased steering angle causes degradation of the side-lobe level (SLL) and prohibitively coarse angular resolution [5]. OPAs can also be implemented using waveguide arrays. A 2-element waveguide array on GaAs with GHz steering speed was demonstrated with a maximum steering angle of ~6º [6]. A thermo-optically controlled waveguide array fabricated on silicon-on-insulator (SOI) demonstrated a steering angle of 2.3° at a wavelength of 1550 nm [7].

For uniform OPAs capable of large angle beam steering, an inter-element spacing of about one-half the operating wavelength is required which would result in strong coupling between adjacent waveguides in the array. In order to overcome this trade-off between the maximum steering angle and waveguide spacing for linear uniform arrays, we proposed a non-uniform array consisting of uniform sub-arrays with non-overlapping grating lobes [5]. Also, compared to a uniform array with half-wavelength spacing, the larger total aperture of such an array results in narrower beam width in the far field, which is advantageous for scanning

applications [5]. In this letter we report the implementation of a non-uniform optical array for large angle beam steering.

NON-UNIFORM ARRAY DESIGN

A schematic of the OPA device on SOI is shown in Figure 14(a), showing both photonic and electronic layers vertically separated by a layer of silicon dioxide for optical isolation. The beam propagation simulation of the photonic circuitry of Figure 14(a) at λ=1.55μm is shown in Figure 14(b). The optical input power is uniformly divided into 12 waveguides using a 1x12 multimode interference (MMI) beam splitter, which has a width and length of 60μm and 553.4μm, respectively. The input and output access waveguides' widths are 2.6μm, which has been optimized for high MMI performance [8]. The MMI output access waveguides' widths are adiabatically tapered down to 500nm over 250μm length using a linear taper for single mode operation. Previously, we reported that this MMI coupler has an insertion loss of 1.13dB, and uniformity fluctuation within 0.72dB [9]. The input light is transverse-electrically (TE) polarized that provides higher optical mode confinement compared to the transverse-magnetic (TM) polarization for 500nm x230nm single mode silicon waveguides [Fig. 15(a)]. Also, due to the large index discontinuity at the top and bottom waveguide faces, the TM mode profile has larger vertical spread that reaches the micro-heaters and result in high propagation loss with a 1μm top cladding of SiO_2.

There are 12 independently addressed 800nm wide and 500μm long thermo-optic (TO) phase modulators, as depicted in Fig. 14(a), to provide continuous phase tuning needed for beam steering. Independent phase shifters enable us to reset with modulo 2π phase shifts ($2m\pi+\Delta\theta_n=$

$\Delta\theta_n$, where m is a positive integer and $\Delta\theta_n$ is the phase shift of the n^{th} element) [10]. The following passive s-bend phase shifters [Figure 14(b)] compensate for the quadratic MMI beam splitter output phase profile [11] and change the separation of the uniform MMI outputs to that of the non-uniform array. This phase compensation allows the output beam to be steered at 0^o when no heat is applied to the 12 phase shifters. The waveguides are then arranged in a non-uniform 12-element array, consisting of 3 four-element uniform sub-arrays, as shown in Figure 15(a). The spacing of each i^{th} sub-array s_i is chosen such that there is no overlap of its far-field grating lobes with those of the other sub-arrays [5]. The smallest inter-element spacing is 3.1μm and the total array size is A=46.5μm.

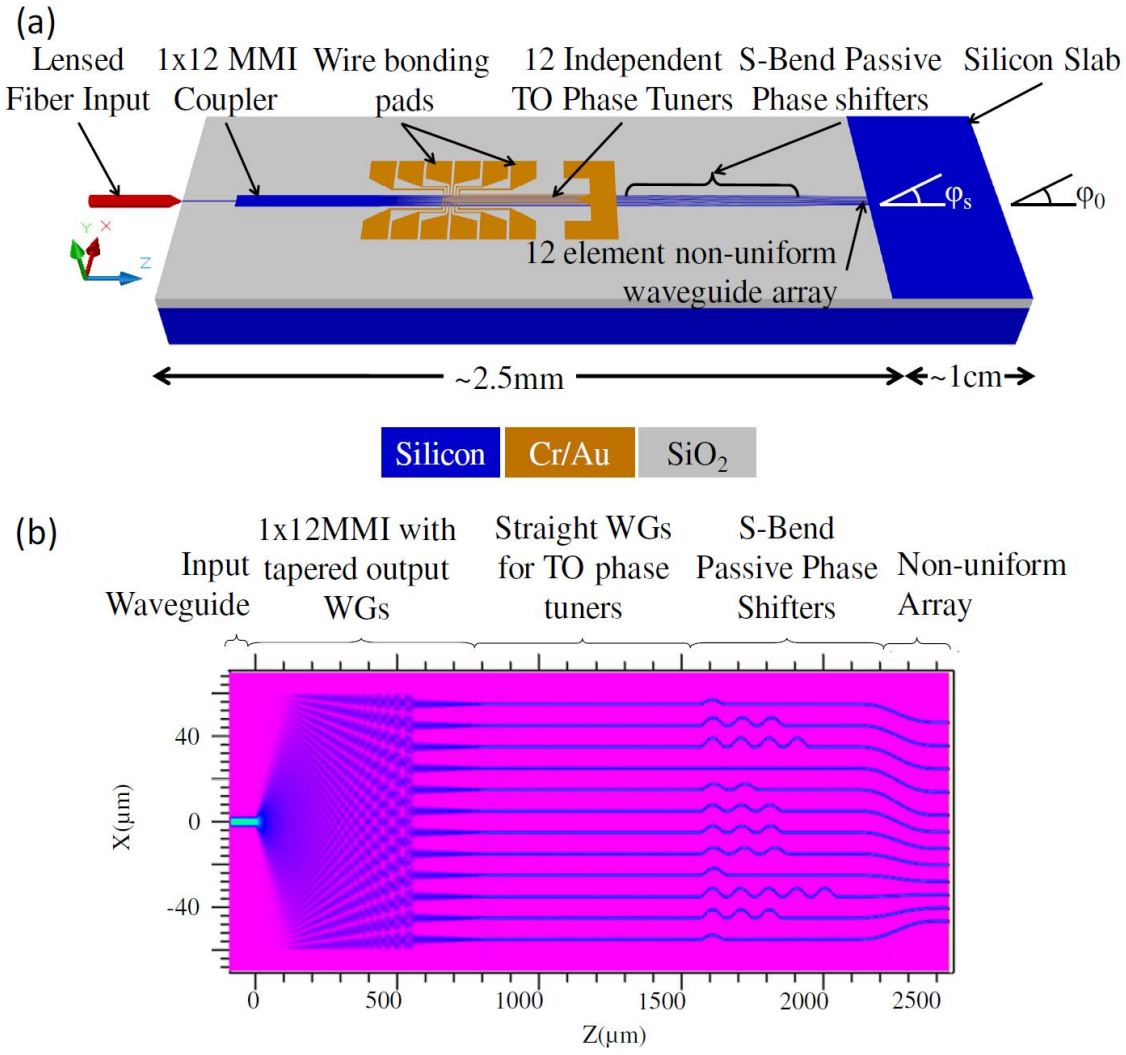

Figure 14-(a) A schematic of the silicon waveguide based optical phased array. (b) Beam propagation simulation of the photonic circuit.

The OPA output waveguides are terminated at a 1cm long silicon planar guide, in which the interference of the light from the 12-channel array results in beam steering at the far field zone. The steering angle is observed along the exit side of the planar guide at the chip edge [Figure 14(a)]. For the far field condition to be satisfied, $\beta_\rho \frac{|\bar{\rho}|^2}{2|\bar{\rho}|} \ll 1$is required [12], where A is the aperture size of the OPA, λ is the operating wavelength, and D is the distance of the observation

point from the array (here the length of the silicon planar guide), and n_{eff} is the effective refractive index of propagation inside the silicon slab. Similar to the uniform array, the non-uniform array is linearly phased, that is for any n^{th} array element, $\gamma_n / \left|\overline{d_n}\right| = r$, where ψ_n is the phase applied to the n^{th} element, $\overline{d_n}$ is the position vector of the n^{th} element, and r is a constant. The steering angle inside the silicon planar guide is given as $\varphi_s = \arcsin\left(\omega\sqrt{\mu\varepsilon_{eff}} / r\right)$. Note that as the beam reaches the end of the slab and enters free space, its direction is governed by Snell's Law. The theoretical far field patterns for steered and non-steered beams are shown in Figure 15(b).

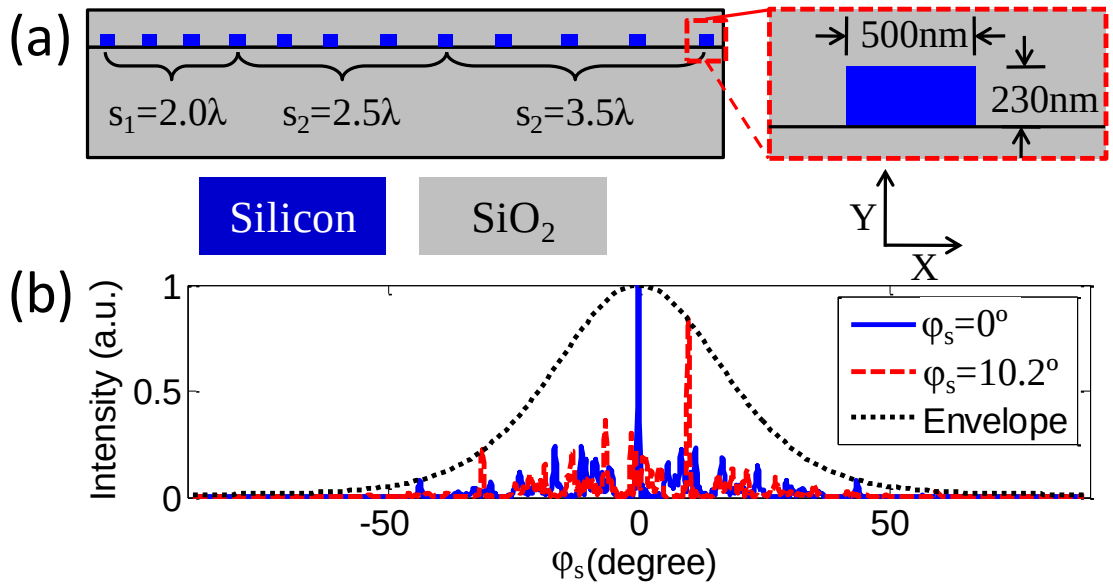

Figure 15-(a) 12-element non-uniform array design with 3 sub-arrays of single-mode silicon waveguides embedded in silicon dioxide, with dimensions of a single waveguide shown in the inset. (b) Theoretical far-field pattern for a non-steered and a steered beam inside the planar guide. The envelope is the far field pattern of a single silicon waveguide embedded in silicon dioxide.

DEVICE FABRICATION

We used SOI from SOITEC with 3μm buried oxide (BOX) and 250nm top silicon layer, which is thermally oxidized to create an oxide etch mask, leaving a final silicon thickness of 230nm. Electron beam lithography and reactive ion etching is used to pattern this layer to form the photonic circuitry. A scanning electron microscope (SEM) picture of the interface between the unequally spaced OPA and silicon nanomembrane planar guide is shown in Figure 16(a). Using the Plasmatherm 790, a 1μm thick film of plasma-enhanced chemical vapor deposition (PECVD) silicon dioxide (325ºC, 80W, 400mTorr, 42sccm N_2O, 21sccm SiH_4) was deposited as top cladding, which is sufficient to isolate the TE guided modes from the electrodes to prevent high optical loss. Metal heaters are patterned over the waveguides by e-beam lithography and thermal evaporation and liftoff of 150nm of Cr/Au [10/140] film. An optical microscope picture of the heaters aligned over the output waveguides and 12 bonding pads is shown in Figure 16(b).

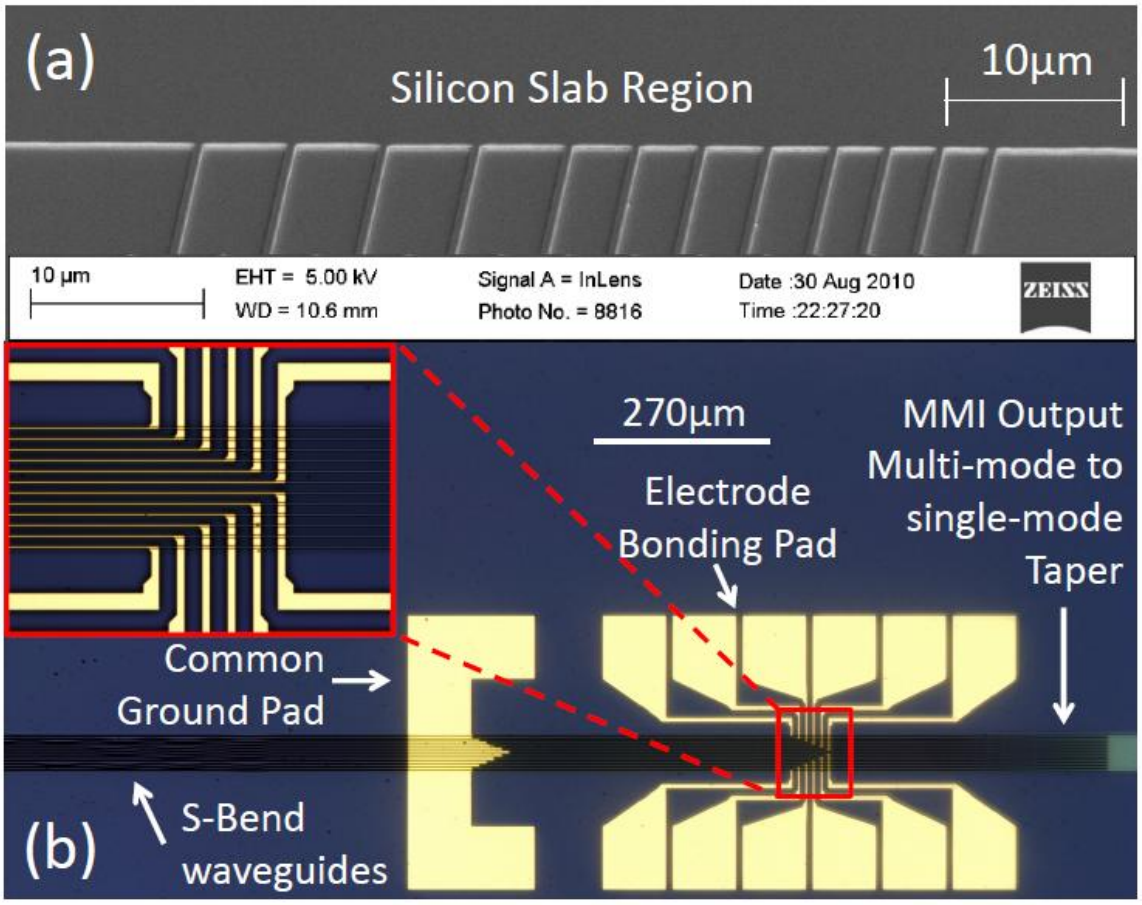

Figure 16-(a) Tilted SEM view of the unequally spaced OPA output and silicon nanomembrane planar guide. (b) Optical microscope picture of the 12 thermo-optic heaters with bonding pads.

We engineered the "bread loafing" effect in which self-aligned voids are formed during PECVD oxide deposition, and are shown in Figure 17(a). COMSOL Multiphysics simulations in Figure 17(b) indicate the effectiveness of these voids in directing the generated heat toward the silicon waveguides by reducing lateral heat transfer, and therefore reducing the required power for phase shifting. To accurately characterize the phase perturbations of the thermo-optical modulators, we fabricated Mach-Zehnder (MZ) modulators alongside the OPA devices with

dimensions identical to the OPA with regard to waveguide and heater geometry. We experimentally confirmed a switching power of P_{π}=12.4mW along with a switching time of 9.8μs which corresponds to a steering speed of 100kHz.

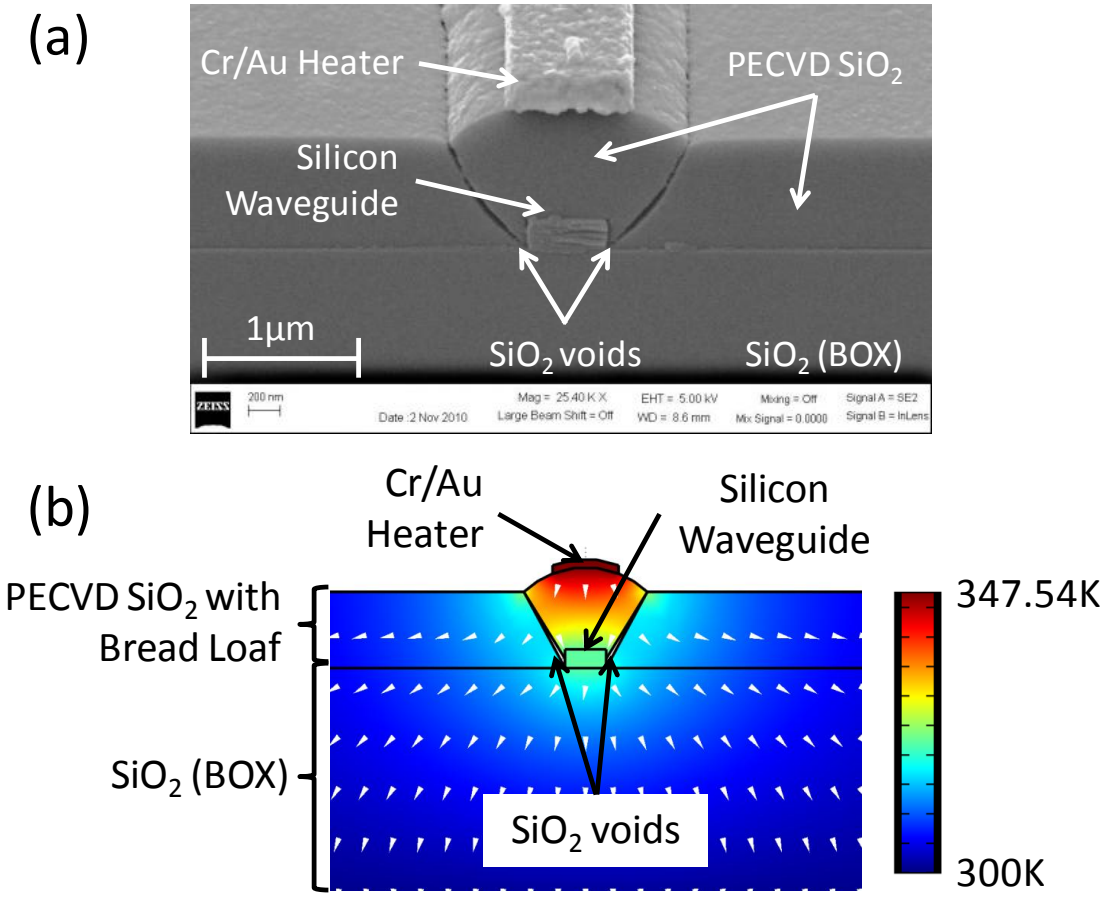

Figure 17-(a) SEM cross section of a heater over its waveguide. (b) COMSOL Multiphysics simulation of the thermal profile of the microheater and waveguide cross section with bread loafing of the oxide.

EXPERIMENTAL RESULTS AND DISCUSSION

TE polarized light at 1550nm from a polarization maintaining lensed fiber (PMF) with a 2.5μm output mode diameter was coupled into the input waveguide. An infrared (IR) camera

connected to a variable objective lens captured the top-down far field image at the end of the silicon planar guide.

For active beam steering, we first set the input voltages to thermo-optically modulate the array phases in such a way that the electrical power applied to the micro-heaters, and therefore the applied phase shift of the corresponding array element, is linearly proportional to the distance of the element from the origin. Figure 18(a) demonstrates the measured beam steering angle at the edge of the silicon planar guide, along with the theoretical steering angles as a function of the electrical power to the outermost array element, which needs the largest phase shift. The required electrical input power is calculated using the phase shift data from the MZ test. As shown in Figure 18(a), when the steering angle increases, the power required for beam steering without reset becomes prohibitively large for our voltage source and limits us to a steering angle of 2.5º inside the silicon planar guide. Figure 18(a) also shows beam steering angles achieved with reset by applying modulo 2π phase shifts to the independently controlled electrodes. We were able to steer the beam at 10.2º inside the silicon planar guide equivalent to an effective angle of 31.9º in air as predicted by Snell's Law, with SLL better than -3dB, while limiting the maximum power per channel to less than $P_{2\pi}$=24.8mW.

Using a similar technique as [12], the OPA far field is observed and is used to characterize its output performance. Figures 18(b) and 18(c) demonstrate the OPA performance characterization based on the power efficiency and SLL as functions of the measured steering angle, respectively. The power efficiency is calculated by integrating the intensity over the angle interval that constitutes the main lobe (within $1/e^2$ of the maximum beam intensity). The resulting is then normalized to intensity integrated over -90^0 to $+90^0$. From the simulations, we expect -

4dB SLL at 10.2º. The degradation in the performance is due to the variation in $P_{2\pi}$ of the micro-heaters, which results in increasing inaccuracies in the applied phase shift as the number of resets increases at larger steering angles. Using the effective index of the planar guide, n_{eff} =2.9, we determine that the 10.2° steering in the planar guide corresponds to a steering angle in free space of 31.9°.

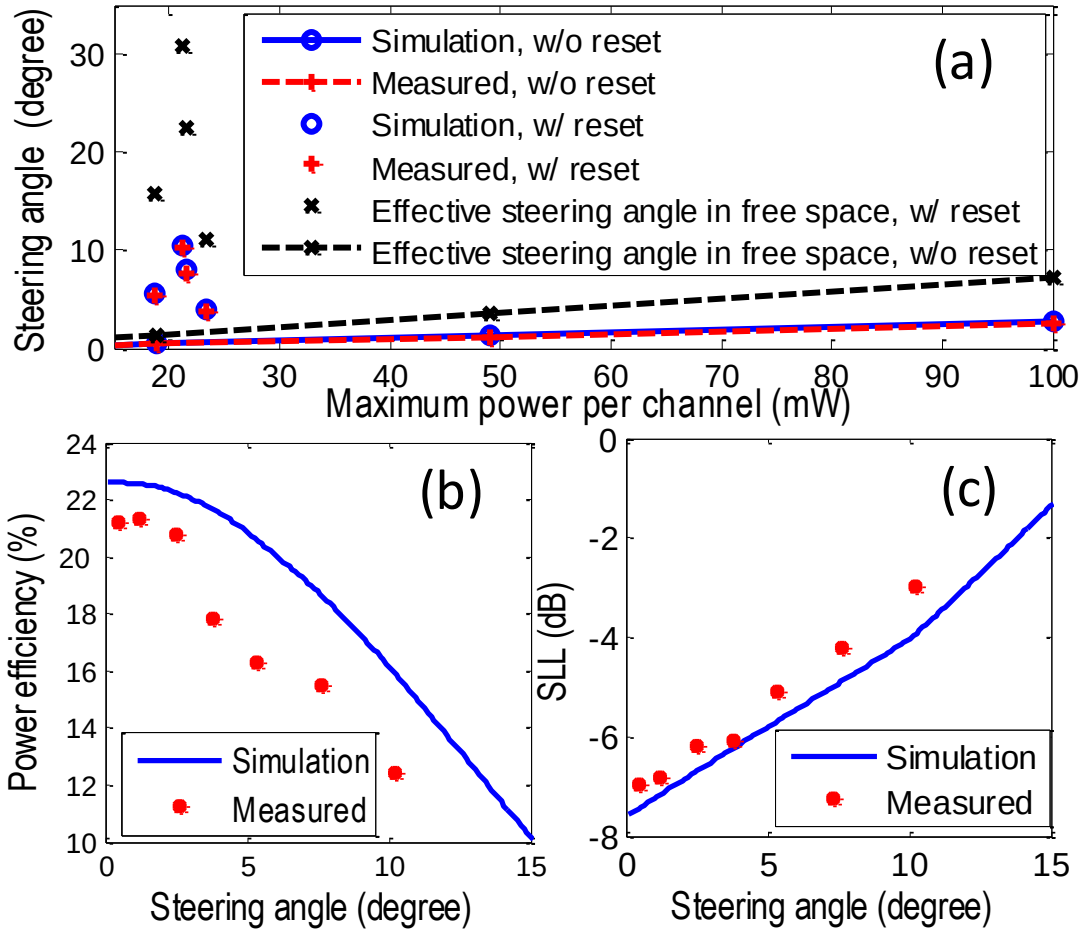

Figure 18- Far field characterization, (a) simulated and measured steering angle versus maximum power per channel. Effective steering angles in free space are determined from measurement data. (b) Power efficiency versus steering angle, (c) side-lobe-level versus steering angle.

SUMMARY

In summary, using a silicon nanomembrane based unequally spaced 1x12 waveguide array for actively tuned OPA that relaxes the strict waveguide spacing requirement for large angle beam steering, we have demonstrated a steering angle in free space of 31.9º at 1.55μm wavelength. Our optical beam steering system is fabricated on SOI using CMOS compatible processes. Phase modulation is achieved thermo-optically via the use of thin-film metal heaters that are independently controlled. We have demonstrated that low-power optical beam steering is possible by applying modulo 2π phase shifts to the independently controlled electrodes. The steering speed is determined by the TO phase shifting mechanism and is 100KHz using the TO effect, which is 2 orders of magnitude larger than LC OPAs.

REFERENCES

[1] Y. Pétremand, P.-A. Clerc, M. Epitaux, R. Hauffe, W. Noell, and N. F. de Rooij, Proc. SPIE 6715, 671502 (2007).

[2] P.F. McManamon, T. A. Dorschner, D. L. Corkum, L. J. Friedman, D. S. Hobbs, M. Holz, S. Liberman, H. Q. Nguyen, D. P. Resler, R. C. Sharp, and E. A Watson, Proc. IEEE 84(2), 268–298 (1996).

[3] X. Wang, B. Wang, J. Pouch, F. Miranda, J. E. Anderson, and P. J. Bos, Opt. Eng. 43, 2769-2774 (2004).

[4] X. Wang X., B. Wang B., P. Bos, P. F. McManamon, J. J. Pouch , F. A. Miranda, and J. E. Anderson, J. Appl. Phys. 98, 073101 (2005).

[5] A. Hosseini, D. N. Kwong, Y. Zhao, Y. –S Chen, F. Crnogorac, R. F. W. Pease, and R. T. Chen, IEEE J. Sel. Topics Quant. elect. 15(5), 1439-1446 (2009).

[6] M. Jarrahi, R. F. W. Pease, D. A. B. Miller, and T. H. Lee, J. Vac. Sci. Technol. B 26, 2124-2126 (2008).

[7] K. V. Acoleyen, W. Bogaerts, J. Jágerská, N. Le Thomas, R. Houdré, and R. Baets, Opt. Lett. 34, 1477-1479 (2009).

[8] A. Hosseini, H. Subbaraman, D. N. Kwong, Y. Zhang, and R. T. Chen, Opt. Lett. 35, 2864-2866 (2010).

[9] D. N. Kwong, Y. Zhang, A. Hosseini, Y. Liu, and R. T. Chen, IET Electronics Letters, 46(18), 1281-1283, (2010).

[10] I. M. Soganci, T. Tanemura, K. A.Williams, N. Calabretta, T. de Vries, E. Smalbrugge, M. K. Smit, H. Dorren, and Y. Nakano, IEEE Photonics Technology Letters, 22(3), 143-145 (2010).

[11] A. Hosseini , D. N. Kwong, Ch.-Y. Lin,B. S. Lee, and R. T. Chen, IEEE J. Sel. Topics Quant. elect. 16(1), 61-69 (2010).

[12] A. Hosseini, D. N. Kwong, Y. Zhang, A. Alu, and R. T. Chen, Appl. Opt. 50(13), 1822-1826 (2011).

Chapter 5: Multilayer Silicon Nanomembranes-Amorphous Silicon

INTRODUCTION TO AMORPHOUS SILICON PHOTONICS

In this chapter I will discuss my work on using hydrogenated amorphous silicon as a way to create multi-layer silicon stacks, thereby enabling us to create a three-dimensionally integrated OPA that can provide steering in 2 directions. I will begin by introducing the material, our experimental results for characterizing our material, and our results for creating multi-layer stacks of amorphous silicon. Unfortunately, due to a tool contamination issue, I was unable to complete the characterization and we were unable to continue with this method for our multi-layer schemes anymore. Therefore, only preliminary results are presented here.

Three dimensional integration of multiple photonic layers is a possible way to increase both the complexity and density of integrated photonic devices. While the crystalline silicon-on-insulator (SOI) substrates typically used for conventional single layer photonic devices are a well-established and superior silicon photonic platform for high index contrast waveguiding, it does not allow for flexible multi-layer stacking due to the inability to deposit crystalline silicon. In contrast, other forms of silicon, such as amorphous or polycrystalline silicon can be deposited using standard CMOS processing and provides the freedom for low-cost multi-layer silicon photonic devices [1]. However, polysilicon typically requires a high thermal budget (≥1000°C) for solid phase crystallization (SPC) of amorphous silicon that is required to reduce the propagation loss to ~6-10 dB/cm [2-4], thereby restricting it to front end of line processing to prevent shifting the doping profile. However, hydrogenated amorphous silicon (a-Si:H) can be

easily deposited using Plasma Enhanced Chemical Vapor Deposition (PECVD) at much lower temperatures of ~200-400°C, making it more flexible in the process flow. PECVD is particularly well suited for depositing hydrogenated amorphous silicon, as the plasma can provide full dissociation of the SiH_4 gas used and thus provide a hydrogen rich environment during the deposition, thereby ensuring that the silicon dangling bonds are passivated.

However, the reported propagation losses for single mode amorphous silicon waveguides range from ~3.46 dB/cm [5] to ~7.5 dB/cm [6], indicating that certain factors can significantly impact the propagation loss. In order to investigate the cause of such a large range in reported propagation losses, Zhu et al [1] examined the dependence of fabrication process and the thermal stability of hydrogenated amorphous silicon waveguides. Specifically, they found that exposing the hydrogenated amorphous silicon waveguides to temperatures above ~300°C increases the propagation loss, and that higher temperatures result in higher losses. This is due to hydrogen out-diffusion. It is well known that amorphous silicon waveguides require the dangling silicon bonds to be passivated with hydrogen, as the absorption due to an unpassivated silicon bond is very strong near 1550nm. However, the Si-H bond is a weak bond, and can easily be broken, allowing the hydrogen to diffuse out. Therefore, it is important that the hydrogenation of the dangling bonds is not jeopardized.

However, it is possible to re-passivate the dangling bond if hydrogen out-diffusion has already occurred. Using a standard Forming Gas Anneal consisting of 10% H_2 and 90%N_2 at 450°C, the larger partial pressure of hydrogen in the forming gas will

drive hydrogen into the amorphous silicon and repassivate the bonds, even though the FGA takes place at 450°C, which is above the hydrogen out-diffusion temperature of ~300°C. In this way, it is possible to replenish the hydrogen in the event that the Si-H bonds are broken and the hydrogen has diffused out.

As such, amorphous silicon seems to be a suitable candidate for 3D integration for a multilayer OPA. We begin by trying to find a suitable recipe to produce a high quality hydrogenated amorphous silicon here on the Plasmatherm 790 PECVD system. Our final optimized recipe is as follows: 50sccm of SiH_4(10% diluted in He), 100sccm Ar, 300°C, 700mTorr chamber pressure, and 150W RF power. Ar is a heavy, but inert gas, and as such it provides extra energy to provide even more dissociation of SiH_4 gas by ion bombardment.

SINGLE LAYER AMORPHOUS SILICON CHARACTERIZATION

We fabricated single layer hydrogenated amorphous silicon waveguides to characterize the propagation loss of our material. We use a standard cutback structure, in which different lengths of single mode waveguides are measured and compared. The input waveguide is 2.5μm wide, which matches the mode field diameter of a lensed fiber. This is tapered down to a single mode width of 500nm using a 500μm long linear taper that is sufficient adiabatic tapering. The waveguide is then tapered back up to 2.5μm for output coupling to another lensed fiber.

Starting with a bare silicon wafer, we use PECVD to deposit 2μm of SiO_2, which serves as the Buried Oxide (BOX) and is thick enough to provide optical isolation from the handle silicon wafer. Using the aforementioned recipe, we deposit 230nm of

hydrogenated amorphous silicon, followed by 45nm of PECVD silicon dioxide which serves as a hard mask for etching. Patterning was achieved by e-beam lithography, followed by Reactive Ion Etching (RIE). A 1μm layer of PECVD silicon dioxide was deposited as top cladding.

Optical Characterization of Single Layer a-Silicon Devices

Optical testing was performed on a six-axis automated aligner system with a 50 nm precision in movement. A polarization maintaining lensed fiber (PMF) with a 2.5μm output mode diameter was used to couple TE polarized light at 1550 nm into the input waveguide. The output was collected by a single mode lensed fiber also with 2.5μm mode diameter. From the cutback structure, we measure the propagation loss of our amorphous silicon waveguides to be 13dB/cm, which is shown below in Figure 19. As this propagation loss is very close to the propagation loss (11dB/cm) that we've measured for the same structure on crystalline silicon waveguides, we conclude that our deposition condition is suitably optimized, and that there is a sufficient degree of hydrogenation, that is, that all of the silicon dangling bonds are hydrogen terminated.

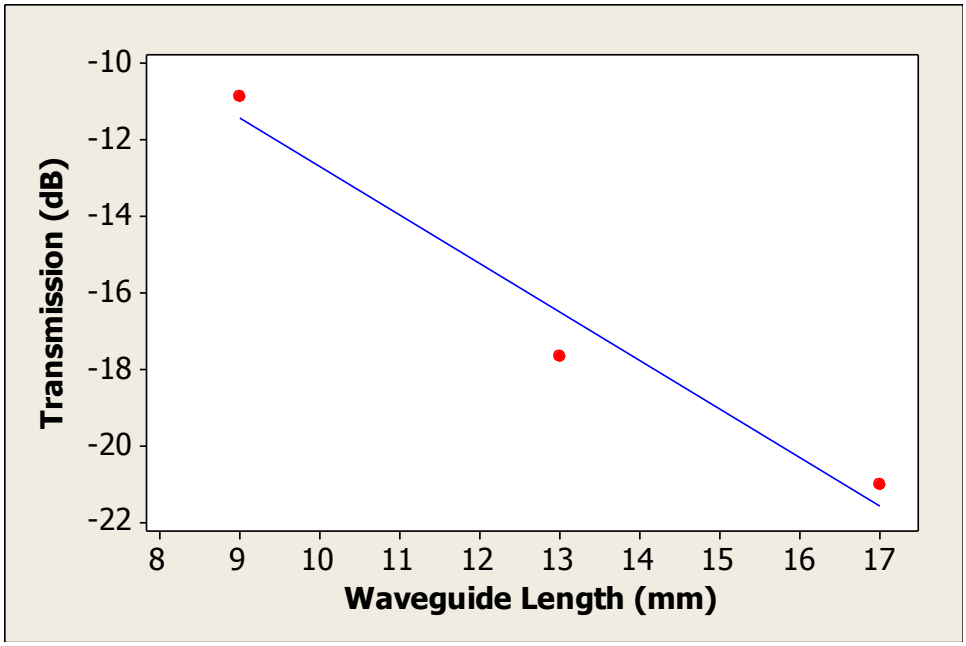

Figure 19-Propagation loss determined by varying singlemode waveguide lengths.

We also fabricated 1x12 MMIs, as described in [7] with L_{MMI}=553.4µm and W_{MMI}=60µm. The access waveguides are W_w=2.6µm. Using a top down IR camera, we can capture the near field image of the MMI outputs, which is shown in Figure 22 below. The top channel is faint due to the presence of a particle defect on the waveguide. Unfortunately, this is the only type of characterization that was obtained, as future samples suffered from a tool contamination issue. With the exception of the blocked channel, we can see good uniformity, indicating that the amorphous silicon material is of high quality.

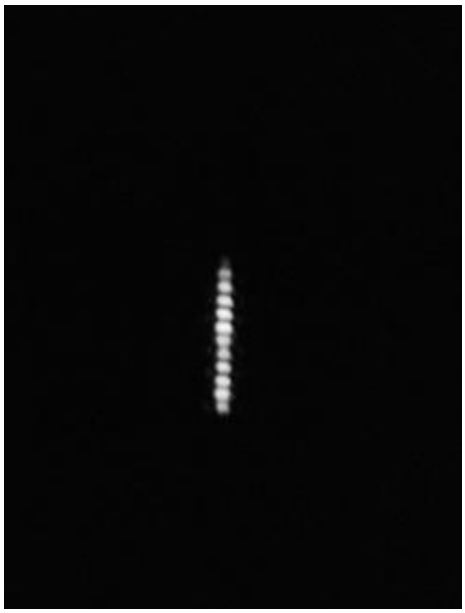

Figure 20-Top down near field image of the 12 MMI outputs fabricated on amorphous silicon.

Although we have demonstrated the feasibility of using hydrogenated amorphous silicon as a suitable photonic layer using a single layer, it is necessary to verify its feasibility in a multi-layer structure.

MULTILAYER AMORPHOUS SILICON STRUCTURES

Fabrication of Staircase Planar Guides

To determine the suitability of amorphous silicon in a multi-layer structure, we use planar slab guides as a means to quickly and efficiently verify. Slab waveguides allow us to determine if each layer can guide light, but without the complexity and long fabrication steps needed if we were to do patterning on each layer. We propose using the slab waveguide structure below, in conjunction with top down IR camera imaging. In a

multilayer stack of slab waveguides, if each slab is terminated with an offset relative to the slab below it, the output of each slab can clearly be seen.

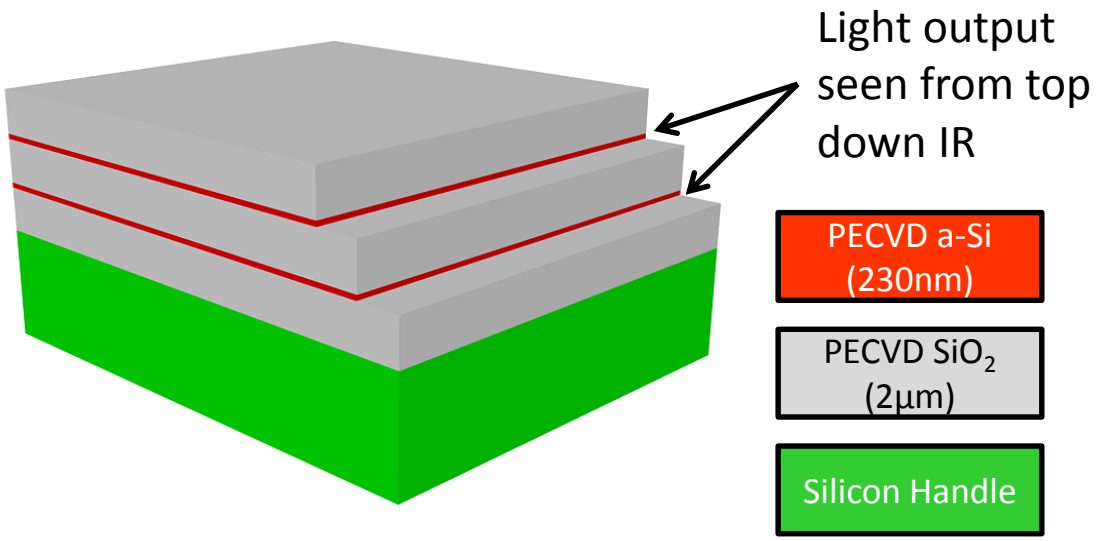

Figure 21-Schematic of a multilayer amorphous silicon stack.

In this way it can easily be seen if each amorphous silicon layer guides light. We then fabricate the structure by alternating between depositing 2µm of PECVD oxide and 230nm of PECVD hydrogenated amorphous silicon. The different slab terminations were created by RIE etching with a photoresist mask. The area to be etched away was exposed by simply using a q-tip dipped in acetone to remove the photoresist from that area. A cross sectional SEM image is shown below in Figure 24 that shows two layers of amorphous silicon separated by 2µm of PECVD oxide.

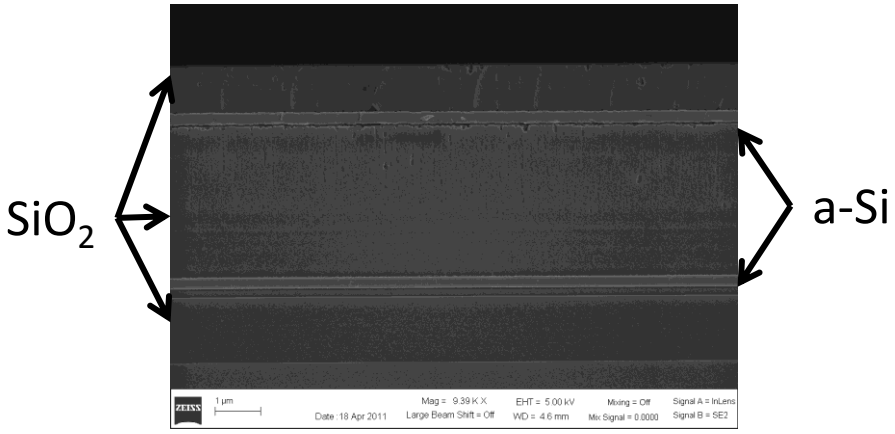

Figure 22-Cross sectional SEM image of a two layer amorphous silicon structure with interlayer PECVD oxide.

With this structure, we can couple light into either top or bottom layer, and observe the scattering from the slab waveguide termination. Top down IR images showing the lensed fiber couple to the top and bottom layers separately, and both layers simultaneously as well. The presence of strong scattering at the slab waveguide edges indicates that the hydrogen passivation of the silicon dangling bonds is still present, otherwise there would be strong absorption and the loss would be too high to observe this. This result further indicates that amorphous silicon is a suitable material for multilayer photonic structures.

Because the goal of our MURI program is to make an 8 layer device, we further extended this 2 layer device to 5 layers, again using planar waveguides with terminated edges that are offset for top down IR imaging. The schematic is shown below, which is just an extension of the 2 layer device.

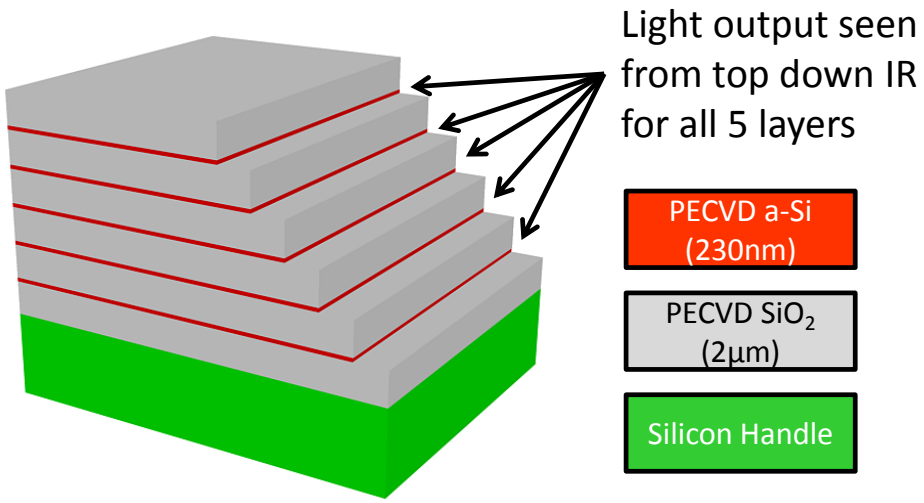

Figure 23-5 layer structure of planar slab waveguides formed with amorphous silicon.

The same fabrication process previously described was used here, and a cross sectional SEM of the 5 layer structure, as well as a photograph of the finished chip is shown below.

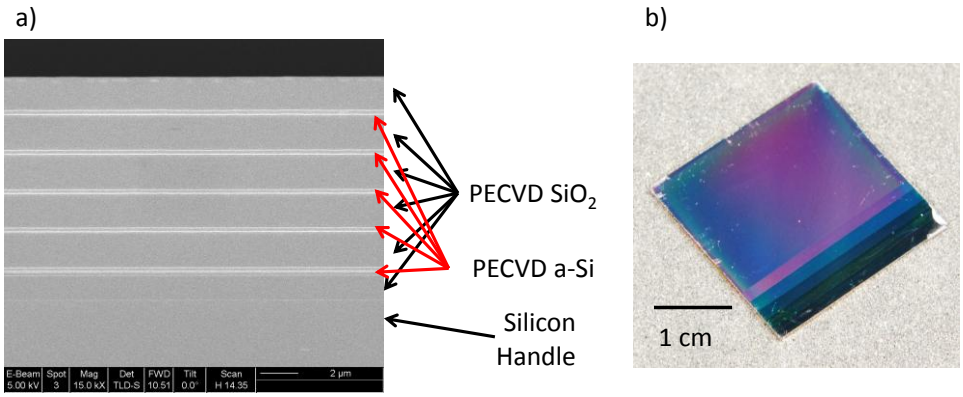

Figure 24-a) SEM cross section and b) photograph of the completed 5 layer amorphous silicon chip with slab waveguides.

Afterwards, the chip was cleaved and lensed fiber was used for coupling. Using an IR camera mounted at a tilt, we can observe the entire chip while testing and see the light coupled to the first amorphous silicon layer.

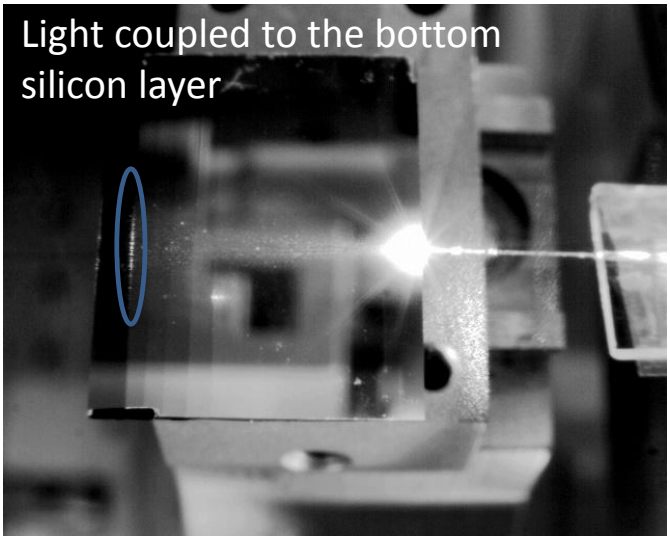

Figure 25-a) IR image of the 5 layer amorphous silicon device, with the bottom layer coupling shown.

SUMMARY

We have demonstrated amorphous silicon as a possible photonic layer for multi-layer applications by fabricating a 1x12 MMI on a single layer device, as well as determine via the cutback method, our propagation loss of ~13dB/cm. While this result is much higher than published works, we compare with the propagation loss of our crystalline silicon and find that the values are very close, thereby showing that the higher loss value is not due to the amorphous silicon material itself, but rather to other parts of

our fabrication process, such as the line edge roughness of the ebeam lithography, or the sidewall roughness of the RIE etch.

We investigate the feasibility of using amorphous silicon in a multilayer structure by fabricating both double layer and 5 layer structures of slab waveguides with the edges offset from each other so as to view each layer with top down IR. These results which shows light coupling to each layer individually, indicate that amorphous silicon can be used for multi-layer applications.

However, soon after these results were obtained, the PECVD tool started producing inconsistent results and our optical testing indicated that all our samples had very high propagation loss and showed no output. We determined that the refractive index of our material was unstable between depositions, and that there was some sort of leak that was allowing either oxygen or nitrogen, or some other contaminant, to be incorporated into our films. A chamber leak that was letting in atmosphere was later found to be responsible for this.

During this period, we also found that the refractive index of the amorphous silicon film is dependent on the degree of hydrogenation, or the percent of hydrogen in the film [8,9]. In particular, Selvaraja et al. also found that the output spectrum of a Mach Zehnder Interferometer (MZI) begins to shift at a critical temperature of T_c=200°C, indicating a hydrogen content dependence of the effective refractive index [8].

In addition, it is well known in the solar cell community that amorphous silicon as a photovoltaic material suffers from light induced degradation, or the Staebler-Wronski Effect (SWE). While the exact mechanics of this phenomenon are still under study, it is

generally agreed that under exposure to light, the defect density in amorphous silicon films increases. This increase in defect density is due to the breaking of the Si-H bond, and indicates that the film does not possess any long term stability.

While this light-induced degradation can be reversed by annealing, such as using a Forming Gas Anneal (FGA), such repeated anneals are not feasible, especially for any commercialized photonic device. Furthermore, we also found that the hydrogen mobility at silicon/silicon dioxide interfaces is reduced by more than 4 orders of magnitude [10]. As there are numerous silicon/oxide interfaces in a multi-layer structure, the time for the hydrogen to reach the bottom layer amorphous silicon layer would be prohibitive and impractical. This indicates that while an FGA can restore the passivation of the silicon dangling bonds for a single layer structure, it is not feasible for multilayer structures.

Our findings that both the refractive index and the propagation loss is dependent on the hydrogen concentration in the film. Combined with the long term instability of the amorphous silicon film and the impracticality of trying to re-hydrogenate the film indicates that amorphous silicon may not be such a suitable candidate for our application after all. While simple waveguides can be made using hydrogenated amorphous silicon, it may not suitable for photonic devices that depends on the refractive index for operation, such as an MMI, or ring resonator. In short, the stability of the film jeopardizes its use for silicon photonics devices.

REFERENCES

[1] Shiyang Zhu, G. Q. Lo, and D. L. Kwong, "Low-loss amorphous silicon wire waveguide for integrated photonics: effect of fabrication process and the thermal stability," Opt. Express **18**, 25283-25291 (2010).

[2] S. Y. Zhu, Q. Fang, M. B. Yu, G. Q. Lo, and D. L. Kwong, “Propagation losses in undoped and n-doped polycrystalline silicon wire waveguides,” Opt. Express 17(23), 20891–20899 (2009).
[3] S. Y. Zhu, G. Q. Lo, J. D. Ye, and D. L. Kwong, “Influence of RTA and LTA on the optical propagation loss in polycrystalline silicon wire waveguides,” IEEE Photon. Technol. Lett. 22(7), 480–482 (2010).
[4] Q. Fang, J. F. Song, S. H. Tao, M. B. Yu, G. Q. Lo, and D. L. Kwong, "Low loss (~6.45dB/cm) sub-micron polycrystalline silicon waveguide integrated with efficient SiON waveguide coupler," Opt. Express 16, 6425-6432 (2008) .
[5] S. K. Selvaraja, E. Sleeckx, M. Schaekers, W. Bogaerts, D. V. Thourhout, P. Dumon, and R. Baets, “Low-loss amorphous silicon-on-insulator technology for photonic integrated circuitry,” Opt. Commun. 282(9), 1767–1770 (2009).
[6] T. Lipka, A. Harke, O. Horn, J. Amthor, and J. Muller, “Amorphous waveguides for high index photonic circuitry,” in Optical Fiber Communication Conference, OSA Technical Digest (CD) (Optical Society of America, 2009), paper OMJ2.
[7] D. N. Kwong, Y. Zhang, A. Hosseini, Y. Liu, and R. T. Chen, “1x12 even fanout using multimode interference optical beam splitter on silicon nanomembrane,”IET Electronics Letters, 46(18), 1281-1283, (2010).
[8] Shankar Kumar Selvaraja, Wim Bogaerts, Dries VanThourhout, and Marc Schaekers, “Thermal trimming and tuning of hydrogenated amorphous silicon nanophotonic devices,” Appl. Phys. Lett. 97, 071120 (2010)
[9] T. Lipka, A. Harke, O. Horn, J. Amthor, and J. Muller, “Amorphous Silicon as High Index Photonic Material,” Proceedings Proc. SPIE 7366, 73661Z (2009)
[10] N.H. Nickel, W.B. Jackson, I.W. Wu, C.C. Tsai, and A. Chiang, “Hydrogen permeation through thin silicon oxide films,” Phys. Rev. B 52, 7791–7794 (1995).

Chapter 6: Low Loss Polycrystalline Silicon Waveguides and Devices for Multilayer On-Chip Optical Interconnects

INTRODUCTION TO POLYSILICON PHOTONICS

On-chip photonic networks are a promising solution for the interconnect bottleneck in high performance microelectronics. Crystalline silicon-on-insulator (SOI) is the most commonly used photonics platform due to its large index contrast with silicon dioxide ($\Delta n \sim 2.02$), which enables submicron waveguides and small bending radii. In addition, SOI exhibits excellent material properties such as low bulk absorption at telecom wavelengths and high electronic carrier mobility. While crystalline SOI is the most desirable, photonic devices would be restricted to the electronic layer. Furthermore, silicon photonics requires a thick Buried Oxide (BOX) layer (typically a few micrometers) for optical isolation from the substrate, but SOI for electronics requires a thin oxide layer ranging from tens to hundreds of nanometers to allow thermal flow into the substrate [1]. Although it has been shown that SOI for electronics can also be used for photonics [2], it comes generally at the cost of more real estate and adds greater complexity and cost to the standard CMOS fabrication process. A multi-layer platform would enable photonic device versatility, as footprint and separation issues are mitigated.

In order to maximize such a platform's design flexibility, CMOS compatible silicon deposition methods are strongly desired. As it is not currently possible to deposit crystalline silicon, alternative materials must be considered. Silicon nitride is a low loss material that has been used for multilayer photonic integration [1], but its lower index contrast increases device footprint, and it also lacks any mechanism for high-speed modulation, limiting nitride to either passive devices or slower devices using the thermo-optic (TO) effect. Hydrogenated amorphous silicon deposited by Plasma-Enhanced

Chemical Vapor Deposition (PECVD) is a low loss material that has been used in multilayer stacks[3], but sufficient and stable hydrogenation of the silicon dangling bonds are critical to maintaining its low loss property. Zhu et al have demonstrated that the propagation loss for hydrogenated amorphous silicon waveguides starts to increase rapidly at temperatures above 300°C [4], and Selvaraja et al have shown that the refractive index change measured from a Mach-Zehnder Interferometer (MZI) starts to occur at 200°C [5]. In addition to thermal stability of hydrogenated amorphous silicon, another significant challenge is that the charge mobility is very low due to the amorphous structure of the film, thereby limiting its application in high-speed applications.

Deposition of polycrystalline silicon (polysilicon) is a mature, CMOS compatible process that is easy to deposit on a variety of substrates. In addition, it can be easily doped to realize electrically active photonic devices due to its relatively high (~100cm2/V-s) [6] electronic carrier mobility. Propagation loss has remained a significant challenge for polysilicon waveguides, which is dominated by scattering and absorption at the polycrystalline grain boundaries. Low loss (~6.45dB/cm) single mode polysilicon waveguides, [7, 8] high quality factor ring resonators [9], and high speed electro-optic modulators [10] formed by Solid Phase Crystallization (SPC) of Low Pressure Chemical Vapor Deposition (LPCVD) amorphous silicon have been demonstrated. Compared to direct deposition of LPCVD polysilicon, SPC of LPCVD amorphous silicon yields superior film qualities, such as smoother surfaces to reduce interfacial scattering and larger grains that result in fewer absorbing and scattering boundaries, further lowering the propagation loss [11].

To date, photonic polysilicon research has focused on waveguides and devices in the single mode region with thicknesses of 200-250nm and widths of 300-500nm, where narrower waveguides result in lower loss due to less confinement of light in the

polysilicon core, indicating that attenuation is dominated by bulk loss [7]. Indeed, efforts to further reduce the overlap of the optical mode with the waveguide cross section have been made by forming polysilicon waveguides in the same step as the polysilicon transistor gate for electronics, resulting in core geometries of 120nm X 350nm and a propagation loss of 6.2 dB/cm at 1550nm [12]. Unfortunately, little work exists for wider, multimode polysilicon devices. Liao et al have reported that thicker and wider polysilicon waveguides suffer from higher propagation losses due to increased optical confinement [11]. However, for key photonic components such as multimode interference couplers (MMI) for beam splitting and arrayed waveguide gratings (AWG) for wavelength division multiplexing (WDM), device dimensions can span tens to hundreds of microns in width [13, 14]. Characterizing the loss of polysilicon at such widths is necessary to determine if these devices can be formed without prohibitively high losses.

In this paper, we demonstrate the lowest propagation loss to date of 0.56dB/cm to date in polysilicon waveguides, and experimentally confirm modal conversion due to polysilicon grain boundary scattering by examining the far field emission of a polysilicon grating coupler. In addition, we also demonstrate the first 1x12 polysilicon MMI with an insertion loss of -1.29dB and a uniformity of 1.07dB.

DESIGN AND FABRICATION

We have used the beam propagation method (BPM) from Rsoft to simulate 10μm wide waveguides for both crystalline silicon and polysilicon with grain boundaries, which is shown in Figure 26 (a) and (b), respectively. Figure 26(a) shows the 10μm wide crystalline silicon waveguide excited by the fundamental mode, which propagates through the waveguide undisturbed. In contrast, a polysilicon waveguide is simulated by adding grain boundaries. The grain boundaries scatter light into higher order modes that

are still guided by the wide waveguide. For narrower waveguides, the grain boundaries scatter light into radiative modes, as higher order modes are not guided. Therefore, the number of guided modes in a given waveguide geometry determines the propagation loss due to grain boundary scattering.

In order to investigate the effect of the waveguide width on the propagation loss of polysilicon waveguides, the waveguide width is varied by using the structure shown in Figure 27(a). Grating couplers are used for input and output coupling. Due to the phase matching condition for grating couplers, the higher order modes excited by polysilicon grain boundary scattering will diffract out at different angles due to their different propagation constants. The details of this grating coupler will be reported separately. After the grating coupler, we first adiabatically taper all waveguide widths to 500 nm in order to filter out higher order modes and achieve single mode propagation. The waveguide is then adiabatically tapered to the desired waveguide width, which ranges from 400 nm to 10 μm. After 5 mm of propagation, all waveguides are then tapered back to the output waveguide width. The same structures are also fabricated on crystalline silicon as a reference. By having the exact same structure and fabrication process, our results can only arise from the differences between the two materials.

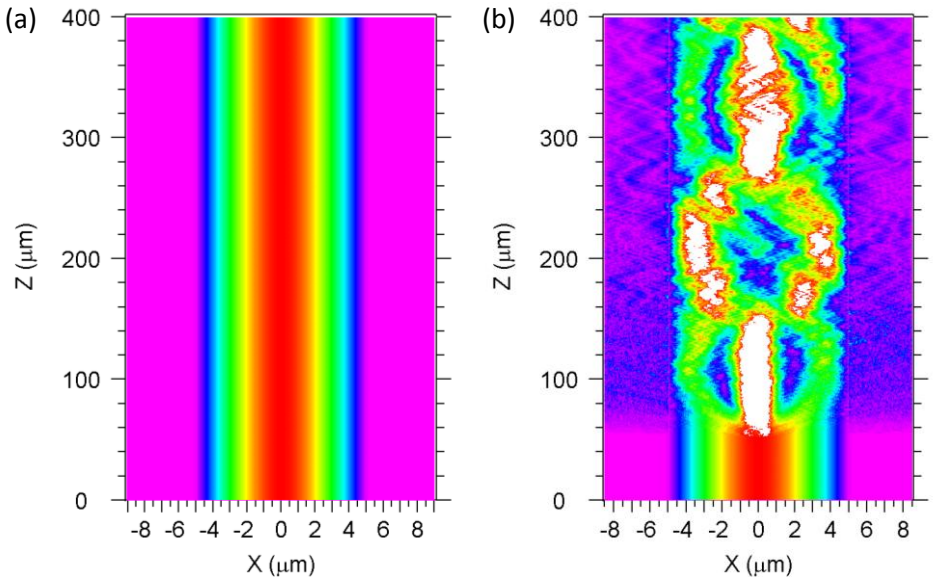

Figure 26-Beam Propagation Method simulation of 10μm waveguide for (a) crystalline silicon and (b) polysilicon with grain boundaries.

In addition, we also designed a 1x12 Multimode Interference (MMI) optical beam splitter to further demonstrate large multimode polysilicon devices. The length and width of the multimode region are L_{MMI}=563.4 μm and W_{MMI}=60 μm respectively. The input and access waveguides are both 2.6 μm wide. To clearly resolve the individual output spots in the near field, a fanout design was used to separate the 12 MMI output channels to 30 μm. A schematic of the 1x12 MMI can be seen in Figure 27(b).

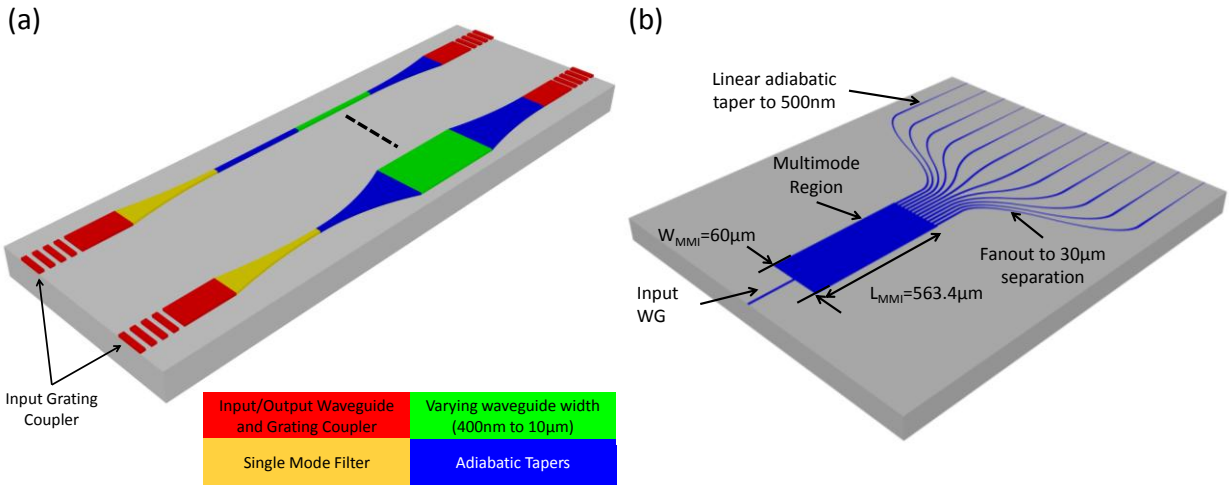

Figure 27-(a) Schematic of waveguide structure. Not drawn to scale. (b) Schematic of 1x12 polysilicon MMI.

In our experiment, we thermally oxidize a bare silicon wafer to create 2.0μm of SiO_2 which acts as the BOX layer and is thick enough to prevent optical leakage into the substrate. Afterwards, a 250nm thick layer of amorphous silicon was deposited using Low Pressure Chemical Vapor Deposition (LPCVD) at 550°C. From [15], we find that the deposition rate should be sufficiently high to minimize the number of nucleation sites, which results in increased grain size. Consequently, we use an increased silane gas flow of 150sccm to achieve a deposition rate of 3.3nm/minute. After the amorphous silicon deposition, we briefly dip the wafers in Piranha solution to form a native oxide layer. This thin native oxide layer stabilizes the top surface of the amorphous silicon and prevents increased surface roughness during future anneal treatments [16]. The wafers are then annealed using a two-step annealing process. The first anneal is a low temperature anneal that is done at 600°C N_2 for 40 hours, and the purpose of this anneal is for gradual grain nucleation, which results in large grains. The second anneal is a 5 hour 1000°C also in N2, and this step is to crystallize the individual polysilicon grains.

In order to estimate our grain size, we use dry oxidation at 900°C for 30 minutes to oxidize the top surface of our polysilicon film. Because polysilicon grains will preferentially oxidize along grain boundaries, we can use Buffered Oxide Etch (BOE) to remove the oxide and then use Scanning Electron Microscopy (SEM) to visualize our grains. A picture of such an SEM image is shown in Figure 28(a), and we estimate the grain sizes to be ~300nm.

The waveguides were patterned using electron beam lithography and Reactive Ion Etching (RIE). Afterwards, a 1µm thick film of SiO2 for top cladding was deposited using PECVD. A cross section view of a single mode polysilicon waveguide is shown in Figure 28(b), and a microscope image of the 1x12 MMI is shown in Figure 28(c).

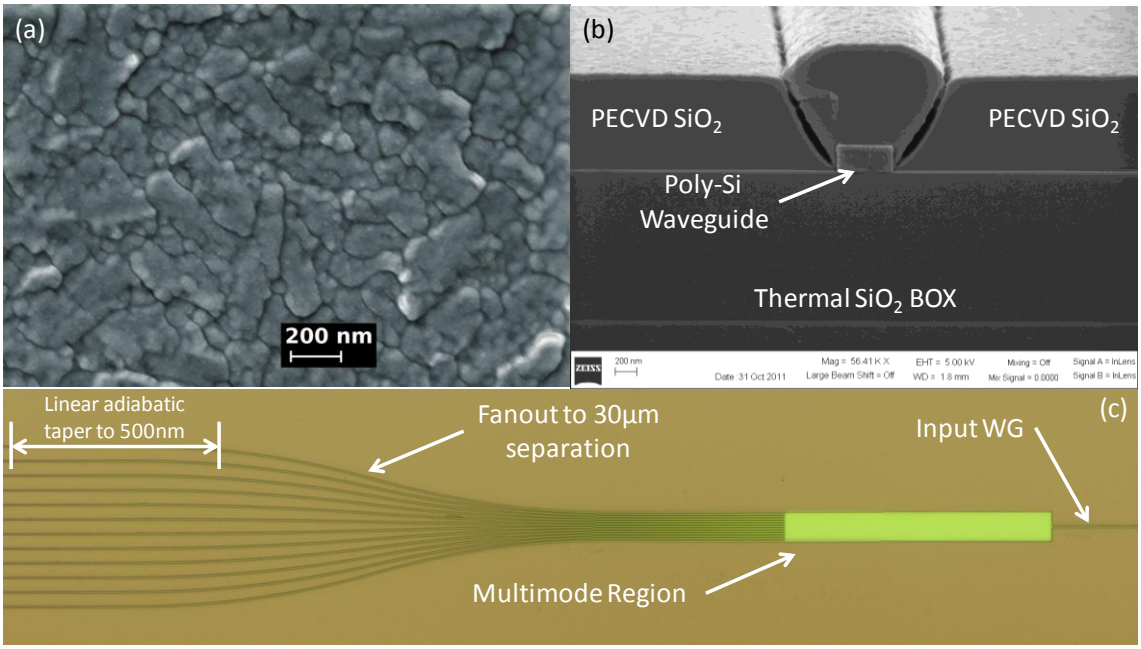

Figure 28-(a) Top down SEM image of polysilicon grains after oxidation and BOE, (b) cross sectional SEM of a single mode polysilicon waveguide and (c) microscope image of the completed 1x12 MMI.

RESULTS AND ANALYSIS

Transverse Electric (TE) polarized light at 1550nm was coupled into the input grating coupler using a polarization maintaining fiber (PMF) and collected from the output grating by standard single mode fiber (SMF). The propagation loss of various waveguide widths for both crystalline and polysilicon are shown below in Figure 29.

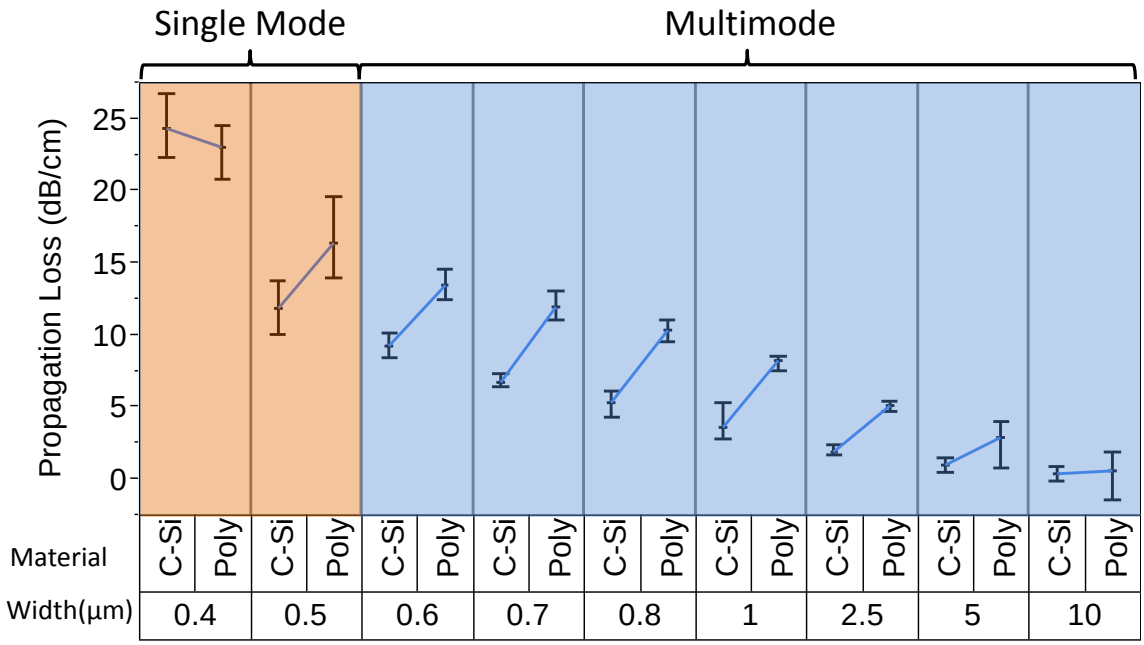

Figure 29-Propagation loss of various polysilicon and crystalline silicon waveguide widths.. Standard error bars are given for each data measurement.

The propagation loss decreases for both crystalline silicon and polysilicon as the waveguide width increases. At a waveguide width of 400nm, the propagation losses of crystalline and polysilicon are virtually the same, but as the waveguide width increases, the loss difference between the two also increases. For waveguide widths above 2.5µm, the difference in propagation loss between crystalline and polysilicon decreases until they have nearly identical propagation losses at 10µm. For crystalline silicon, this behavior is well known and is due to decreasing sidewall interaction of the fundamental mode of the

waveguide [17]. However, the grain boundaries present in polysilicon cause scattering to either radiation modes or higher order modes depending on whether the waveguide width supports the higher modes. This scattering into radiation modes causes the additional loss between polysilicon and crystalline waveguides of the same width.

The presence of the higher order modes has been experimentally confirmed using the setup shown in Figure 30(a) in which light at 1550nm is coupled out of the grating coupler and the far field image is observed on the IR CCD suspended 5cm above the grating. The higher order modes that are excited by the grain boundaries and can still be guided by the waveguide will have different propagation constants, and therefore will be emitted from the grating coupler at different angles according to the phase matching condition. The far field image for a crystalline silicon waveguide and grating can be seen in Figure 30(a), in which a single peak can be seen, which is due to only the fundamental mode of the waveguide being emitted. This can be contrasted with the far field of a polysilicon waveguide and grating with identical dimensions to that of crystalline silicon, which is shown in Figure 30(b). It can clearly be seen that there is not a single peak, but instead continuous emission across a multitude of angles, which indicates the presence of higher order modes each with their different propagation constants, and hence different emission angles. Such a result experimentally demonstrates the existence of mode conversion due to polysilicon grain boundary scattering.

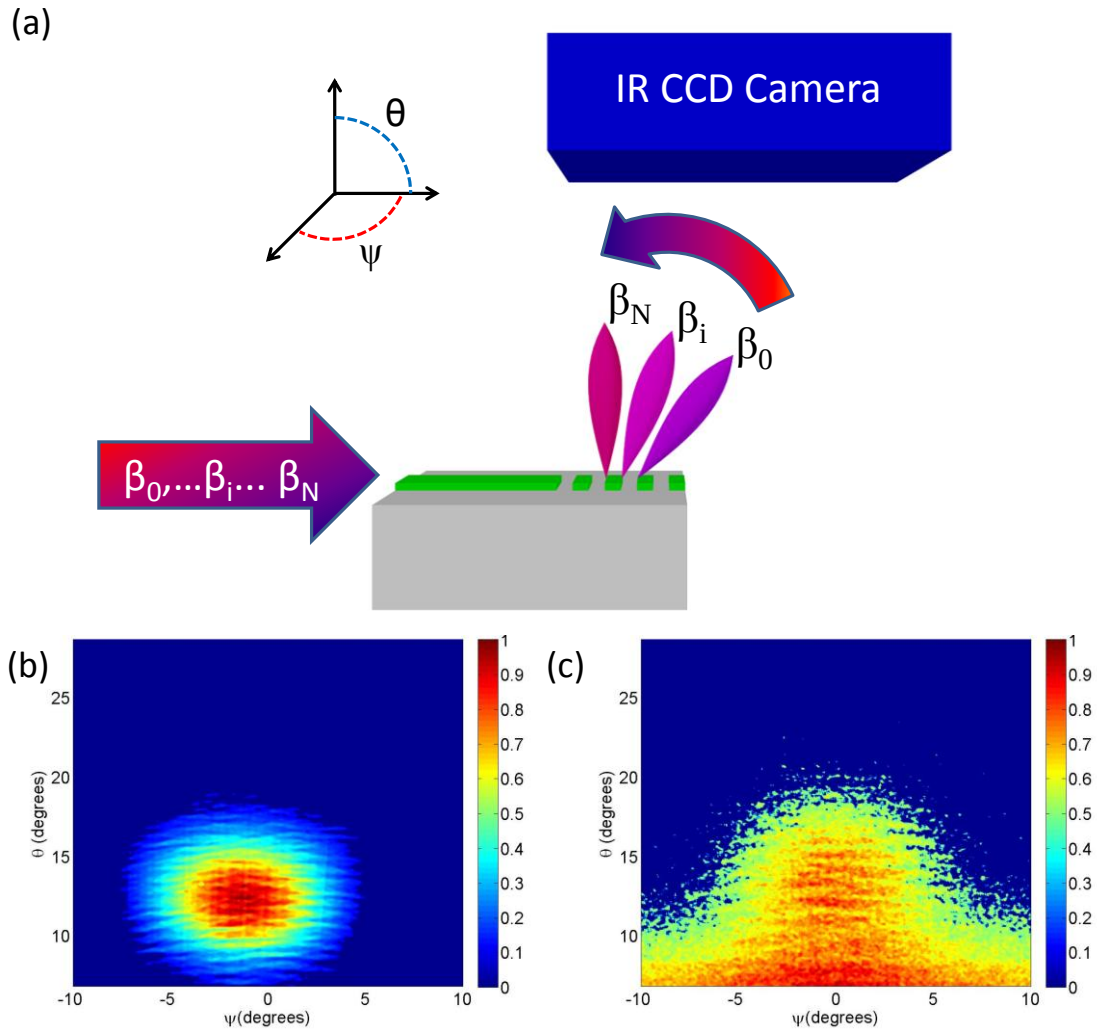

Figure 30-(a) Schematic of experimental setup using an IR CCD to examine the far field emission of the grating coupler. (b) Far field image of a crystalline waveguide and grating. (c) Far field image of polysilicon waveguide and grating identical to that made of crystalline silicon.

It is important to note that at a 10μm waveguide width, both polysilicon and crystalline silicon waveguides have the lowest losses of 0.56dB/cm and 0.31dB/cm, respectively. To our knowledge, this value is the lowest propagation loss for a polysilicon waveguide to date. Furthermore, it indicates that there is very little bulk absorption from the polysilicon grain boundaries. This behavior of decreasing propagation loss with

increasing waveguide width validates the use of large polysilicon waveguides in photonic integrated circuits whenever bandwidth-density is affordable [18].

We fabricated the first polysilicon based 1x12 MMI and experimentally confirmed the functionality of such a 60μm wide polysilicon device. As before, TE polarized light at 1550nm was coupled into the 1x12 MMI. Using an IR camera, 12 output spots are imaged from the MMI fanout, which are shown in Figure 31(a). To characterize the performance of this 1x12 MMI, we used standard SMF to collect each of the 12 output intensities from the output grating couplers, which is shown in Figure 31(b). The performance of an MMI can be described by output uniformity and insertion loss. The uniformity is calculated as $10\log\left(I_{\max}/I_{\min}\right)$, where I_{max} and I_{min} are the maximum and minimum output intensities of the MMI, respectively. The insertion loss of the MMI is defined as $-10\log\left(\sum I_i/I_{in}\right)$, where I_i is the output intensity of the i^{th} output channel, and I_{in} is the intensity of a straight waveguide with the same dimensions of the MMI input waveguide. For our polysilicon 1x12 MMI, we determine a uniformity of 1.07dB and an insertion loss of -1.29dB. This is due to the presence of the multimode region of the MMI, which is 60μm wide and 563.4μm long and has a much lower loss compared to the much narrower input waveguide. We have previously demonstrated a 1x12 MMI on crystalline silicon with comparable performance [19].

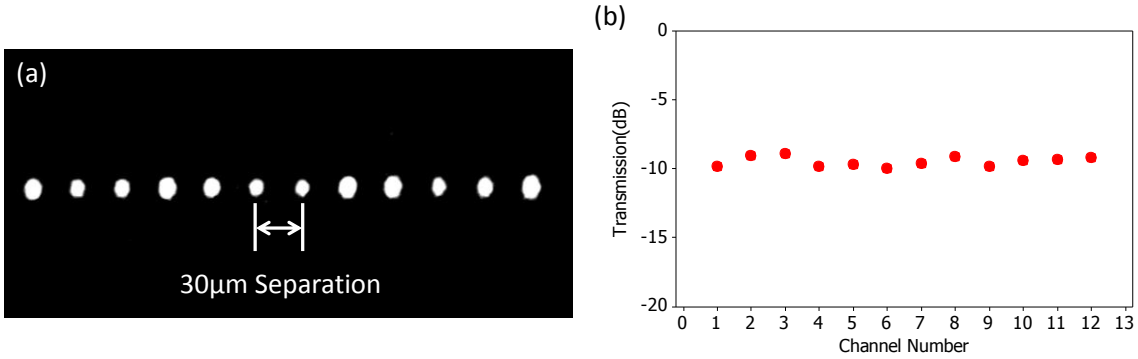

Figure 31-(a) IR image of the 12 output spots from 1x12 MMI fanout. (b) Output intensities of the 1x12 polysilicon MMI.

SUMMARY

We have investigated the feasibility of multimode polysilicon waveguides to demonstrate the suitability of polysilicon as a candidate for multilayer photonic applications. SPC with a maximum temperature of 1000°C is used to create polysilicon on thermal SiO_2. We then measure the propagation losses for various waveguide widths on both polysilicon and crystalline silicon platforms. We find that as the width increases for polysilicon waveguides, the propagation loss decreases similarly to crystalline silicon waveguides. The difference in loss between the two platforms for a given waveguide width is due to the scattering from the polysilicon grain boundaries, which excites higher order modes. Depending on the waveguide width, these modes either propagate as higher order modes or are lost as radiation modes. Mode conversion due to grain boundary scattering is experimentally confirmed by observing the far field image of the grating coupler, in which the higher order modes are emitted at different angles according to their different propagation constants. We also find that at a waveguide width of 10µm, the polysilicon propagation loss of 0.56dB/cm is very close to the crystalline silicon propagation loss of 0.31dB/cm, indicating that there is little bulk absorption from the polysilicon. This result validates the use of polysilicon waveguides in photonic integrated

circuits. We further demonstrate this with a 1x12 polysilicon MMI that has a low insertion loss of -1.29dB and a high uniformity of 1.07dB. Together, we present the lowest propagation loss for polysilicon waveguides to date of 0.56dB/cm as well as the first 1x12 polysilicon MMI.

REFERENCES

[1] Nicolás Sherwood-Droz and Michal Lipson, "Scalable 3D dense integration of photonics on bulk silicon," Opt. Express **19**, 17758-17765 (2011).

[2] C. W. Holzwarth, J. S. Orcutt, H. Li, M. A. Popovic, V. Stojanovic, J. L. Hoyt, R. J. Ram, and H. I. Smith, "Localized Substrate Removal Technique Enabling Strong-Confinement Microphotonics in Bulk Si CMOS Processes," in Conference on Lasers and Electro-Optics/Quantum Electronics and Laser Science Conference and Photonic Applications Systems Technologies, OSA Technical Digest (CD) (Optical Society of America, 2008), paper CThKK5.

[3] JoonHyun Kang, Yuki Atsumi, Manabu Oda, Tomohiro Amemiya, Nobuhiko Nishiyama and Shigehisa Arai, "Low-Loss Amorphous Silicon Multilayer Waveguides Vertically Stacked on Silicon-on-Insulator Substrate," Jpn. J. Appl. Phys. **50,** 120208 (2011).

[4] Shiyang Zhu, G. Q. Lo, and D. L. Kwong, "Low-loss amorphous silicon wire waveguide for integrated photonics: effect of fabrication process and the thermal stability," Opt. Express **18**, 25283-25291 (2010).

[5] Shankar Kumar Selvaraja, Wim Bogaerts, Dries VanThourhout, and Marc Schaekers, "Thermal trimming and tuning of hydrogenated amorphous silicon nanophotonic devices," Appl. Phys. Lett. **97**, 071120 (2010).

[6] T. Kamins, Polycrystalline Silicon for Integrated Circuits and Displays, 2nd ed. (Kluwer, 1998).

[7] Shiyang Zhu, Q. Fang, M. B. Yu, G. Q. Lo, and D. L. Kwong, "Propagation losses in undoped and n-doped polycrystalline silicon wire waveguides," Opt. Express **17**, 20891-20899 (2009).

[8] Q. Fang, J. F. Song, S. H. Tao, M. B. Yu, G. Q. Lo, and D. L. Kwong, "Low loss (~6.45dB/cm) sub-micron polycrystalline silicon waveguide integrated with efficient SiON waveguide coupler," Opt. Express **16**, 6425-6432 (2008).

[9] Kyle Preston, Bradley Schmidt, and Michal Lipson, "Polysilicon photonic resonators for large-scale 3D integration of optical networks," Opt. Express **15**, 17283-17290 (2007).

[10] Kyle Preston, Sasikanth Manipatruni, Alexander Gondarenko, Carl B. Poitras, and Michal Lipson, "Deposited silicon high-speed integrated electro-optic modulator," Opt. Express **17**, 5118-5124 (2009).

[11] L. Liao, D. R. Lim, A. M. Agarwal, X. Duan, K. K. Lee, and L. C. Kimerling, "Optical transmission losses in polycrystalline silicon strip waveguides: effects of

waveguide dimensions, thermal treatment, hydrogen passivation, and wavelength," J. Electron. Mater. **29**(12), 1380–1386 (2000).

[12] Jason S. Orcutt, Sanh D. Tang, Steve Kramer, Karan Mehta, Hanqing Li, Vladimir Stojanović, and Rajeev J. Ram, "Low-loss polysilicon waveguides fabricated in an emulated high-volume electronics process," Opt. Express **20**, 7243-7254 (2012).

[13] Hosseini, A.; Kwong, D.N.; Yang Zhang; Subbaraman, H.; Xiaochuan Xu; Chen, R.T., "1xN multimode interference beam splitter design techniques for on-chip optical interconnections," IEEE Jounal of Selected Topics in Quantum Electronics **17**, 510-515 (2011).

[14] P. Dumon, W. Bogaerts, D. Van Thourhout, D. Taillaert, R. Baets, J. Wouters, S. Beckx, and P. Jaenen, "Compact wavelength router based on a Silicon-on-insulator arrayed waveguide grating pigtailed to a fiber array," Opt. Express **14**, 664-669 (2006).

[15] Hatalis, Miltiadis K.; Greve, David W.; , "Large grain polycrystalline silicon by low-temperature annealing of low-pressure chemical vapor deposited amorphous silicon films," Journal of Applied Physics, **63,** 2260-2266, (1988).

[16] Effiong Ibok and Shyam Garg, "A Characterization of the Effect of Deposition Temperature on Polysilicon Properties," J. Electrochem. Soc. **140**, 2927 (1993).

[17] Yurii Vlasov and Sharee McNab, "Losses in single-mode silicon-on-insulator strip waveguides and bends," Opt. Express **12**, 1622-1631 (2004).

[18] Mauro J. Kobrinsky, Bruce A. Block, Jun-Fei Zheng, Brandon C. Barnett, Edris Mohammed, Miriam Reshotko, Frank Robertson, Scott List, Ian Young, Kenneth Cadien, "On-Chip Optical Interconnects," Intel Technology Journal, **8**, 129-142 (2004).

[19] Kwong, D.; Zhang, Y.; Hosseini, A.; Liu, Y.; Chen, R.T.; , "1 X 12 even fanout using multimode interference optical beam splitter on silicon nanomembrane," Electronics Letters, **46**, 1281-1283 (2010).

Chapter 7: Subwavelength grating couplers on SOI for Fiber-to-chip Coupling with SU-8 Top Cladding

INTRODUCTION: COUPLING TO NANOPHOTONIC CIRCUITS

In this section I discuss my work on using grating couplers as a means for coupling from single mode fibers to silicon nanophotonic circuits. We use a subwavelength grating (SWG) structure. The applications of grating couplers will be discussed here, but also in the next section on future work, as we intend to use grating couplers for beam steering as well.

The SOI platform provides a high index contrast between silicon due to the difference in refractive indexes ($\Delta n \sim 2.02$), and enables ultra-compact photonic devices and high integration density in photonic circuits. However, coupling light to and from single mode fibers remains a challenge due to the large mode mismatch. Even with lensed fiber coupling, the mode mismatch is still significant. Techniques such as inverted tapers, in which a small tip is created to expand the mode size to match that of the fiber, is an effective way to improve the coupling, but the fabrication can be challenging depending on the type of lithography used to create the small tip. Furthermore, inverted tapers require precise cleaving of the chip at the location of the tip. Not only is this a high risk process, but it also makes wafer scale testing impossible.

Grating couplers are possible solution to this, as it requires no post-fabrication processing, and wafer scale testing is possible. However, previous grating couplers have required complicated fabrication processes, such as shallow etching with multiple lithography steps [1], bottom reflectors, epitaxial silicon overlay [2]. It is desirable to pattern the grating coupler in the same step as the rest of the nanophotonic circuit, that is, to have a single-etch grating coupler. However, a through etch grating can be problematic in that the refractive index contrast between

silicon and the cladding material (typically air or oxide) is too high, and therefore the grating is too strong. This results in a large back-reflection, and the coupling efficiency is jeopardized. It is desirable to reduce the index contrast to reduce the back-reflection and enhance the coupling efficiency, which is what a shallow etched grating achieves. Another solution is the use of subwavelength grating structures. Using these subwavelength structures enables us to create an effective index that can be tuned between the index of silicon and the cladding material, thereby essentially placing an artificial high index material in the grating and reducing the index contrast.

In addition, most grating couplers so far have used an air top cladding, but for a commercialized product in most applications, some sort of top cladding will be required for passivation purposes. We present a through etch grating with an SU-8 top cladding using a subwavelength grating structure that achieves ~20% coupling efficiency and a 3dB bandwidth of 53nm with a center wavelength of ~1550nm.

DESIGN OF A SUBWAVELENGTH GRATING COUPLER

The grating diffraction is governed by the phase matching condition, which is given by $k_0 n_{eff} = k_0 n_c \sin\theta + q\frac{2\pi}{\Lambda}$, where $k_0 = 2\pi/\lambda$, n_c is the refractive index of the cladding, θ is the angle of the output light, n_{eff} is the average effective index for the optical mode in the grating, and q is an integer representing the diffraction order, which is 1 in this section, and Λ is the period of the grating.

A schematic of a SWG coupler is shown below in Figure 32, where W_{SWG} and L_{SWG} are the widths and lengths of the subwavelength trench, respectively. Λ_{GRAT} is the

period of the grating, and Λ_{SWG} is the period of the subwavelength region, perpendicular to the direction of propagation.

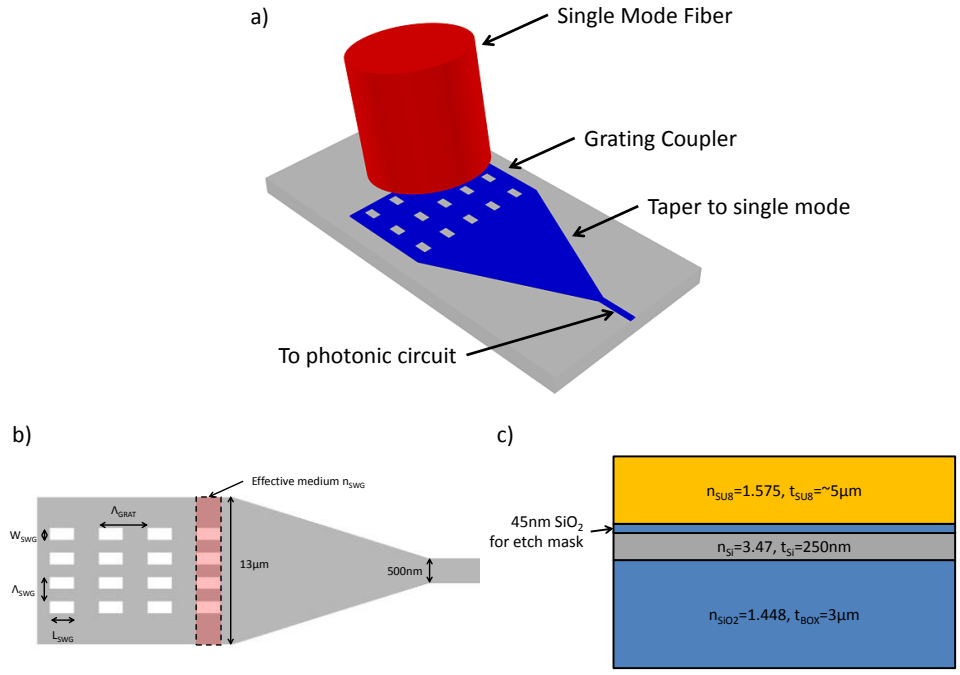

Figure 32-(a) Schematic of fiber coupling to SWG coupler. (b) Top down schematic of SWG coupler with parameters. (c) Cross sectional schematic of our grating coupler stack. The handle silicon layer is not shown here.

We first use the open source simulation package CAMFR, which is based on eigenmode expansion, to optimize our grating design by assuming an artificial index of n_{SWG} as the index of the SWG region, and also optimize the grating period Λ_{GRAT} and fill factor. We determine that the optimum fill factor is 50%, Λ_{GRAT}=735nm, and n_{SWG}=2.15, as shown in Figure 33(a). We also determine that layer thicknesses of both the silicon layer and the BOX layer can be optimized, as shown in Figure 33(b) and (c), respectively. The SOI available to our group has a top silicon layer thickness of 250nm, and a BOX thickness of 3µm. Although we typically oxidize the top silicon layer to create an oxide hard mask for RIE etching, it can be seen that higher efficiencies can be reached, and at

lower n_{SWG} for thicker top silicon layers. This is because the index contrast between the silicon and the SWG area is increased. For the BOX thickness, there is resonance seen, and this is due to either a constructive or destructive interference of the light emitted downwards and reflected by the silicon handle wafer. Unfortunately for us, 3µm BOX results in almost complete destructive interference. However, using deposited silicon, or silicon nanomembrane transfer, we can create silicon layers on top of properly optimized BOX thickness.

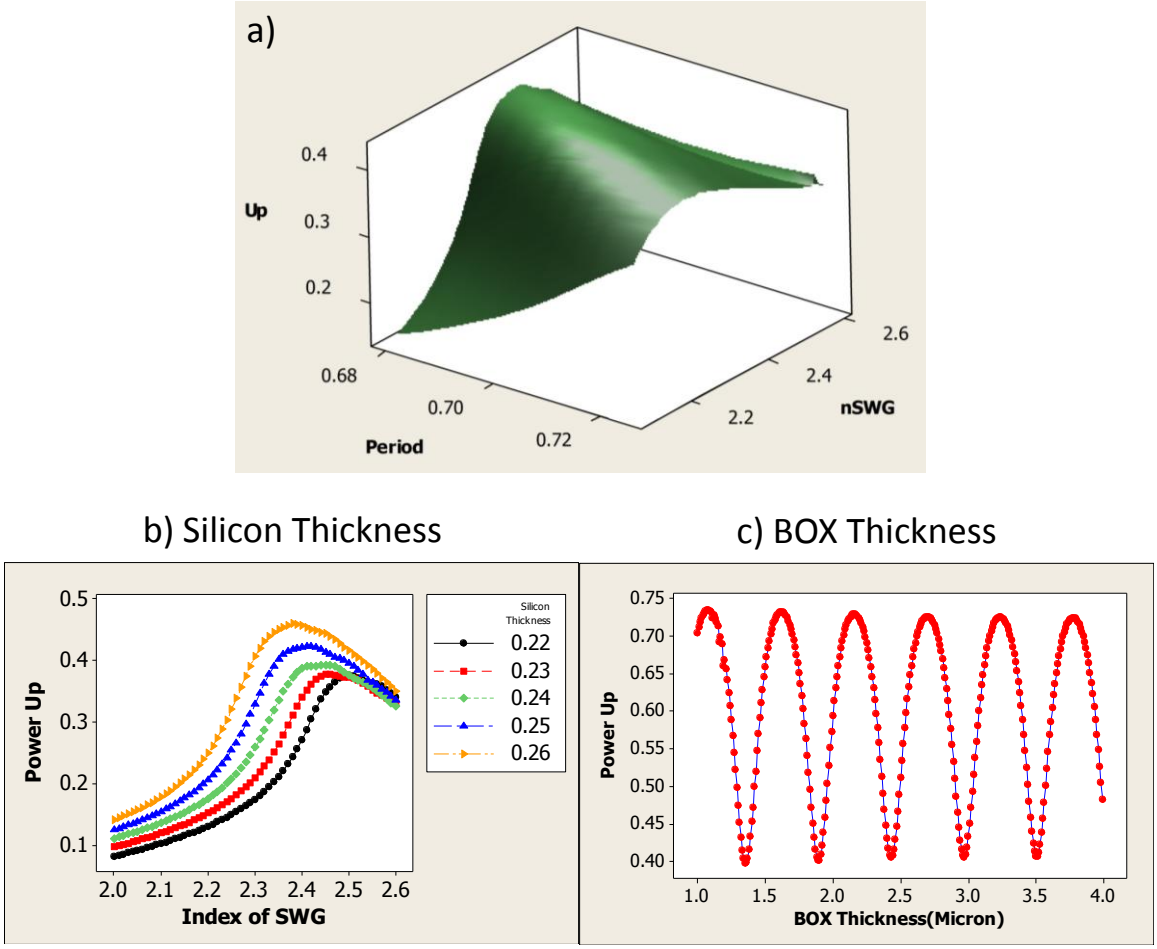

Figure 33-(a) Contour plot of varying grating period and n_{SWG} simultaneously to optimize the power emitted upwards. (b) Varying n_{SWG} with different silicon thicknesses. (c) Effect of BOX thickness on power emitted upwards.

The refractive index of the subwavelength region is engineered based on the Effective Material Theory (EMT) [3], which can calculate the refractive index of both TE and TM polarizations for a given structure. The zero order and second order equations for both TE and TM are shown below, where f_{swg} is the fill factor of the trench in the subwavelength region is defined as W_{SWG}/ Λ_{SWG}, n_{trench} is the refractive index of the material in the trench, n_{si} is the refractive index of silicon, and n_{eff} is the effective refractive index of the slab waveguide.

$$\frac{1}{n_{TE}^{(0)}} = \left(\frac{f_{swg}}{n_{trench}^2} + \frac{(1-f_{swg})}{n_{si}^2} \right)^{1/2}$$

$$n_{TM}^{(0)} = \left(f_{swg} n_{trench}^2 + (1-f_{swg}) n_{si}^2 \right)^{1/2}$$

$$n_{TE}^{(2)} = n_{TE}^{(0)} \left(1 + \frac{\pi^2}{3} \left(\frac{n_{eff} \Lambda_{swg}}{\lambda} \right)^2 f_{swg}^2 (1-f_{swg})^2 (n_{trench}^2 - n_{si}^2)^2 \left(\frac{n_{TM}^0}{n_{effTE}} \right)^2 \left(\frac{n_{TE}^0}{n_{trench} n_{si}} \right)^4 \right)^{1/2}$$

$$n_{TM}^{(2)} = n_{TM}^{(0)} \left(1 + \frac{\pi^2}{3} \left(\frac{n_{eff} \Lambda_{swg}}{\lambda} \right)^2 f_{swg}^2 (1-f_{swg})^2 \left(\frac{n_{trench}^2 - n_{si}^2}{n_{effTM} n_{TM}^{(0)}} \right)^2 \right)^{1/2}$$

Accordingly, we choose the trench width to be W_{SWG}=100nm, and Λ_{SWG}=394nm to achieve an n_{SWG}=2.15.

RESULTS AND DISCUSSION

Our SWG coupler is made using e-beam lithography and RIE etching. Afterwards, SU-8 2005 was spun on at 3000rpm and soft-baked to form the top cladding. An SEM picture of the grating region is shown below in Figure 34(a). We test our grating on the setup shown in Figure 34(b), in which 10° wedges are used to mount fiber chuck holders, and all mounted on an XYZ stage with a tilt stage as well to give us tenability in the fiber angle. Input coupling is done with a polarization maintaining fiber to ensure TE polarization. The output is collected by a single mode fiber. The transmission spectrum is shown in Figure 34(c). It can be seen that the peak coupling

efficiency is ~20%, with a peak wavelength centered around 1550nm and 3dB bandwidth of 53nm.We believe that the Fabry-Perot seen in the spectrum are due to reflections from the fiber facet and the top SU-8 cladding. The use of an index matching fluid would reduce or eliminate this. The peak efficiency of ~20% is not very high compared to published works, and this is due to the use of a top cladding. Previous works with an air cladding have a large index contrast between top cladding and bottom cladding, and it is this vertical asymmetry that enables more power emitted upwards. The use of a top cladding effectively reduces the vertical index contrast, by making the structure more vertically symmetric. As a result, the coupling efficiency is lower.

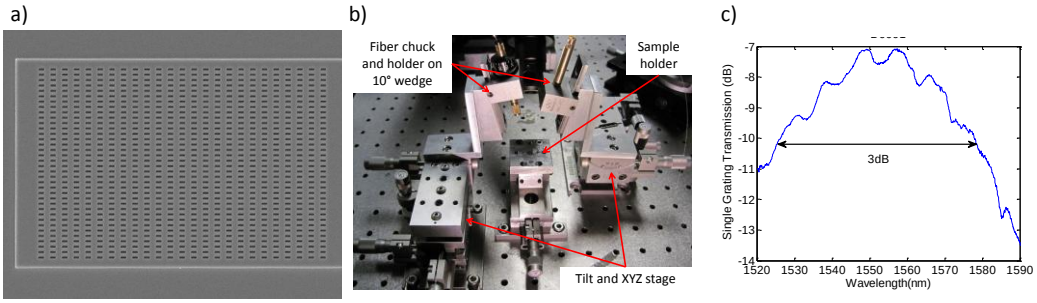

Figure 34-(a) SEM image of the SWG coupler region. (b) Setup for testing our grating with 4 degrees of freedom. (c) Output spectrum of a single SWG grating.

REFERENCES

[1]]D. Taillaert, "Grating couplers for coupling between optical fibers and nanophotonic waveguides," Jpn. J. Appl. Phys. 45, 6071-6077(2006)

[2] G. Roelkens, "High efficiency diffractive grating couplers for interfacing a single mode optical fiber with a nanophotonic silicon-on-insulator waveguide circuit," Appl. Phys. Lett. 92, 131101(2008)

[3] R. Halir et al, "Continuously apodized fiber-to-chip surface grating coupler with refractive index engineered subwavelength structure," Optics Letters 35, 3243-3245(2010)

Chapter 8: Corrugated Waveguide based Optical Phased Array with Crosstalk Suppression using 2D Photonic Crystal

INTRODUCTION

Optical phased arrays (OPAs) integrated on chip can provide agile and precise beam steering in free space without any mechanical parts. They can be used for a variety of beam steering applications, including LIDAR and other surveying or mapping applications or point-to-point communications in metropolitan regions or within high performance computing for board to board or chip to chip communications.

Recent optical phased arrays fabricated on silicon on insulator (SOI) achieve free space optical beam steering through wavelength tuning of shallow etched gratings, which reduces a silicon grating's inherently large index contrast in order to decrease the grating strength. This increases the effective aperture of the emitted optical signal, and ultimately results in narrow far field beam widths. However, shallow etched gratings not only require precise etching control, but the multiple lithography and etch steps that are required also increase fabrication complexity and cost. Acoleyen et al achieved a beam width of ~2.5° by shallow etching 70nm of the 220nm silicon device layer [1]. Doylend et al used a significantly thicker silicon layer of 500nm and shallow etched the output gratings by 75nm to achieve a beam width of 0.6° [2]. While using a thicker silicon layer can reduce the index contrast for a given etch depth, the disadvantage of this approach is the higher power consumption required to achieve thermo-optic phase shifting due to heating an increased waveguide volume. In addition, due to the thickness of the silicon layer, which supports multiple vertical modes, rib waveguides are needed for single mode propagation, thereby adding an additional patterning step. It is desirable to utilize a structure that requires only a single patterning step, and can also realize small index contrasts necessary for achieving narrow longitudinal beamwidths, while still using

single mode silicon device layers. In this work we present a 16 element OPA fabricated on SOI with a 250nm silicon device layer that uses laterally corrugated waveguides for free space coupling and realizes narrow far field beam widths. Furthermore, we also place 2D photonic crystal (PC) slabs between the array elements for optical crosstalk suppression.

DESIGN OF PHOTONIC COMPONENTS

A schematic of the OPA is shown in Figure 35(a) and consists of several key components as follows: a wideband subwavelength fiber to waveguide grating coupler for coupling light into the photonic circuit, cascaded 1x2 multimode interference (MMI) couplers for optical beam splitting, and the output corrugated waveguide gratings which emit to free space. All of these components are designed for Transverse-Electric (TE) polarization.

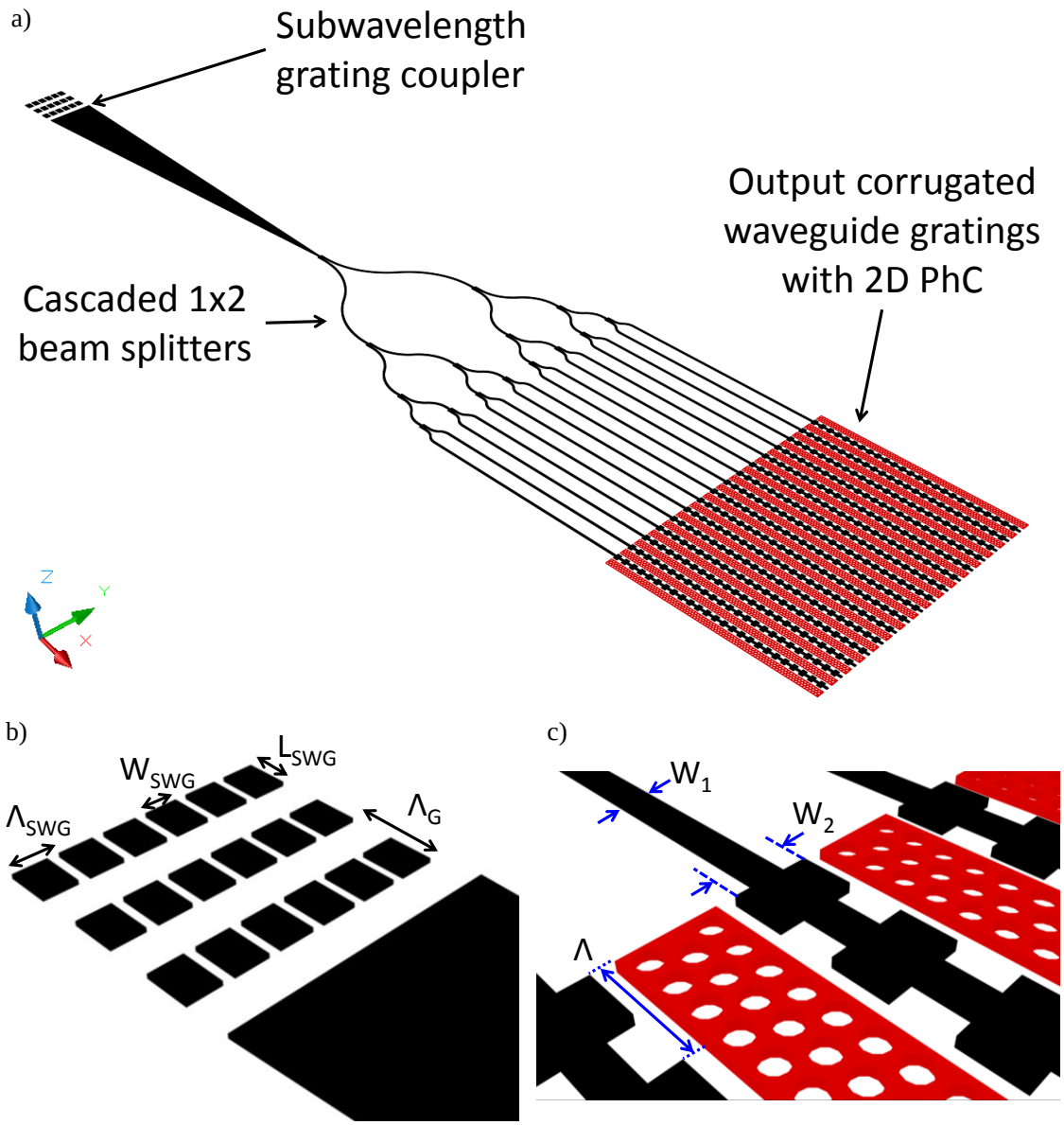

Figure 35-(a) Schematic of the grating coupled 16 element optical phased array consisting of corrugated waveguides separated by 2D photonic crystal. (b) Closeup view of the subwavelength grating coupler. (c) Closeup of the corrugated waveguides with 2D photonic crystal isolation.

Grating couplers provide advantages in larger misalignment tolerances compared to direct butt coupling or using lensed fibers while eliminating the need for facet preparation. Grating couplers using periodic subwavelength nanostructures (SWN) allow refractive index engineering to increase the coupling efficiency to a single mode fiber while allowing single step patterning. A schematic of the grating coupler with SWN is shown in Figure 35(b). The SWN can be treated as a homogeneous medium according to the effective medium theory (EMT) when the subwavelength period Λ_{SWG} is below the wavelength in the material. The refractive index of the SWN region n_{SWG} is an intermediate value between a high index material ($n_{high}=n_{si}=3.48$) and low index material ($n_{low}=n_{air}=1$), and is a function of the fill factor, which is defined as W_{SWG}/Λ_{SWG} according to EMT theory [3]. Typical demonstrated silicon based grating couplers have 3dB bandwidths of ~50nm, but our wavelength tuning range of 1480-1580nm necessitates grating couplers with larger bandwidth for wideband operation. By lowering the average effective index of the grating to reduce waveguide dispersion, one can increase the bandwidth [4]. The average effective index of the grating can be lowered by choosing the high index region of the grating as the subwavelength region, and the low index region as the cladding. Using 2D Finite Difference Time Domain (FDTD) simulations, we optimize the grating coupler to arrive at a design of grating period $\Lambda_G=1.3\mu m$ with $L_{SWG}=728nm$ and $n_{swg}=2.15$. We then use EMT theory to choose the subwavelength period $\Lambda_{SWG}=360nm$ with $W_{SWG}=290nm$.

The input light is split into 16 uniform outputs by 4 levels of cascaded 1x2 MMI couplers, which allow for equal output phase profiles due to the symmetry of the structure. These 16 outputs are then fed into the 16 element array composed of corrugated waveguides with 4μm spacing.

Laterally corrugated waveguides are essentially alternating waveguide sections with widths w_1 and w_2 periodically repeated by Λ, as shown in Figure 36(a). These corrugations can be fabricated in a single patterning step and allow the structure to function as a free space grating coupler, as shown in the cross sectional E_x field profile of the 3D FDTD simulation in Figure 36(b). The emission angle θ is governed by the phase matching condition, and is given by $\sin(\theta) = (n_{eff,avg} \cdot \Lambda - \lambda) / \Lambda \cdot n_{clad}$, where $n_{eff,avg}$ is the average effective index of the two corrugations, Λ is the grating period, λ is the free space wavelength, and n_{clad} is the refractive index of the cladding material. In addition, as the index contrast in the grating is controlled lithographically by the widths w_1 and w_2, very small index contrast can be precisely achieved by properly choosing the desired combination of w_1 and w_2, as seen in Figure 36(c). In our design, w_1=500nm, and w_2=600nm, and Λ=700nm.

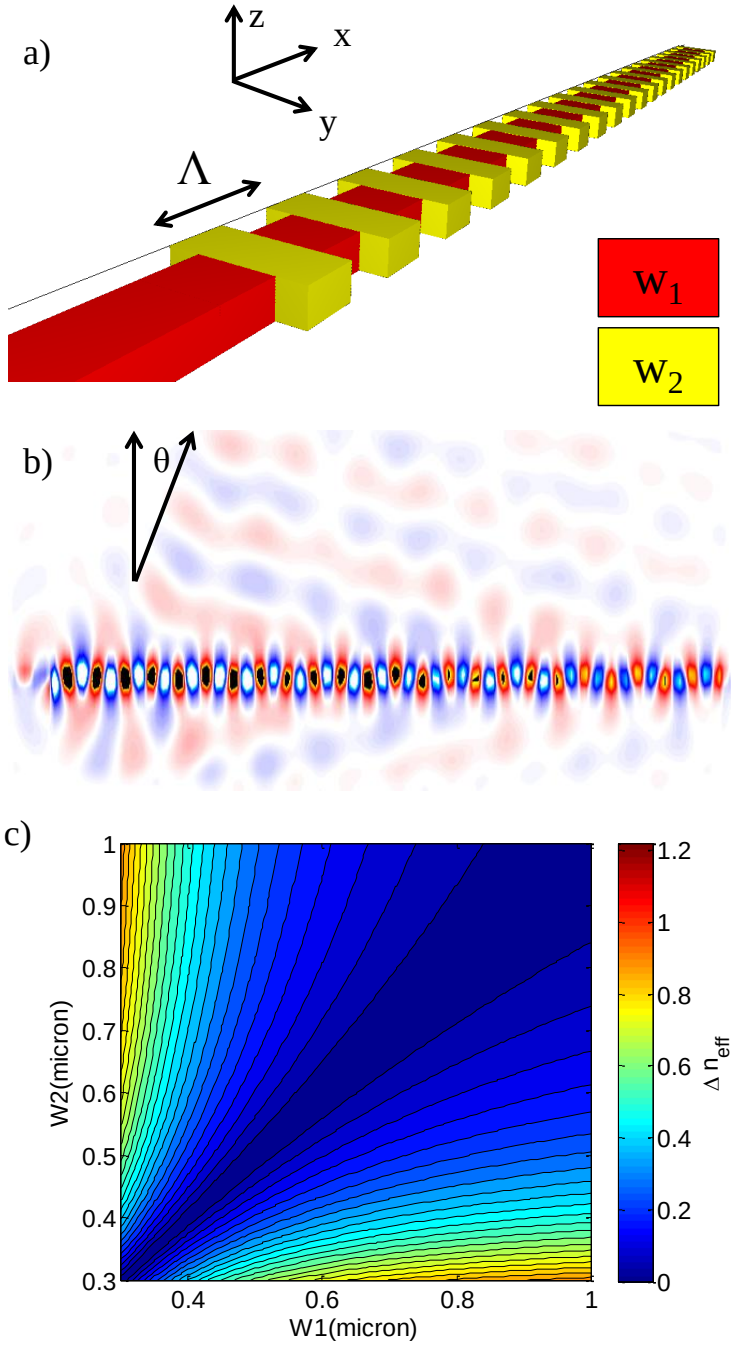

Figure 36-(a) Schematic of a single corrugated waveguide with period Λ and widths w_1 and w_2. (b) E_x field profile of a corrugated waveguide emission from a 3D FDTD simulation. (c) Contour plot of the differences in effective index between different values of w_1 and w_2 for the fundamental TE mode.

However, these lateral corrugations result in grating assisted coupling between adjacent waveguides [6], which results in optical cross talk between adjacent elements in the OPA and ultimately jeopardizes the far field pattern [7]. This optical crosstalk can be seen in the 2D FDTD simulation of Figure 37(a) where a single corrugated waveguide is excited and light is coupled via the corrugations to the adjacent waveguide 4μm away. This coupling between waveguides limits the minimum element spacing, but for large angle beam steering in OPAs, element spacings on the order of the emission wavelength are required. Thus, inter-element isolation is necessary to maximize the steering angle. In this work, 5 periods of a 2D photonic crystal are placed between adjacent array elements to prevent inter-element cross talk. The PC consists of a triangular lattice of air holes with a lattice constant a=612nm, a radius r=0.43a, and a photonic bandgap that covers 1300 to 1800nm, which is adequate for the 1480-1580nm range needed for our application. The transmission spectrum of a plane wave through 5 periods of this PC is shown in Figure 37(b) and clearly shows low transmission in the wavelength region of interest. Figure 37(c) shows the same 2D FDTD crosstalk simulation but with 5 periods of PC placed between the two waveguides. It can clearly be seen that the photonic crystal effectively suppresses the crosstalk between the waveguides. Using this crosstalk suppression scheme of placing PC between corrugated waveguide elements, we fabricate a 16 element OPA and compare it with an identical structure except without PC.

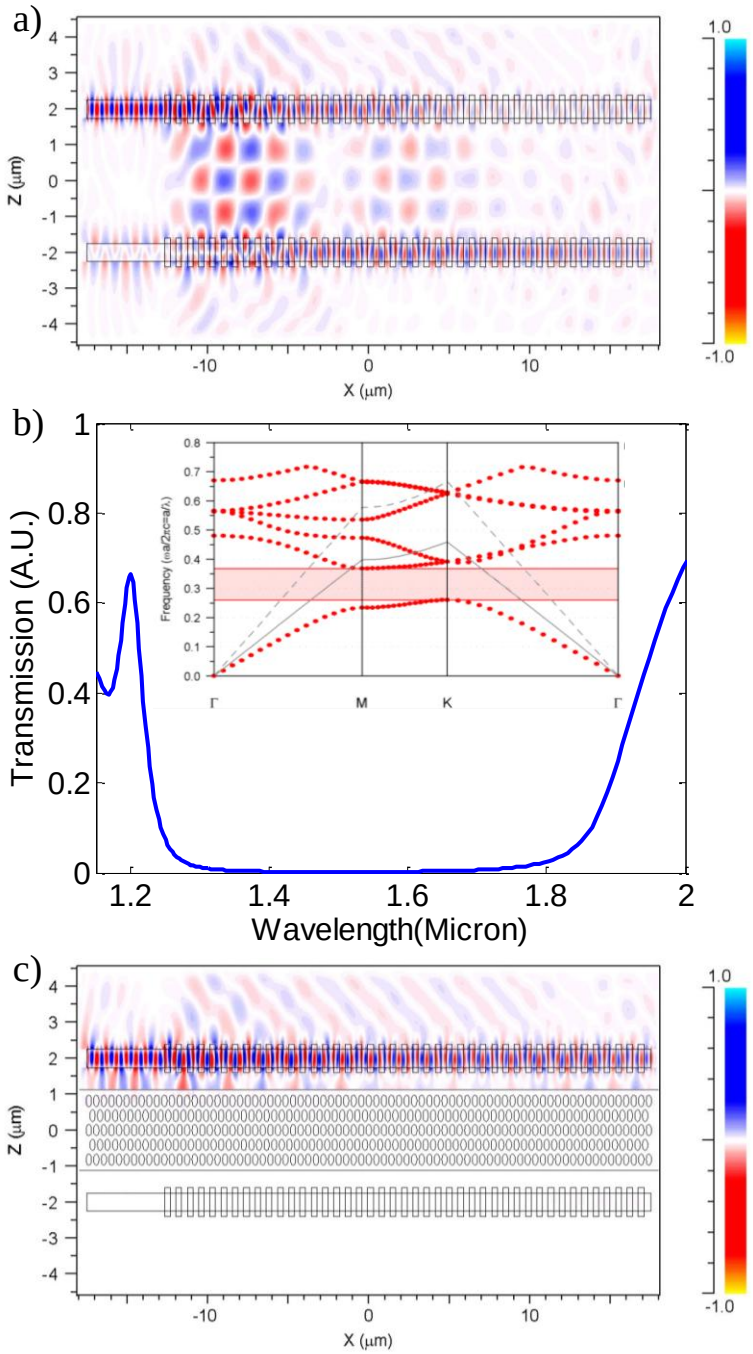
a)
Z (μm)
X (μm)
1.0
-1.0
b)
Transmission (A.U.)
Wavelength(Micron)
Frequency (ωa/2πc=a/λ)
Γ
M
K
Γ
c)
Z (μm)
X (μm)
1.0
-1.0

Figure 37-(a) 2D FDTD simulation of 2 corrugated waveguides spaced 4μm apart showing optical crosstalk between the excited waveguide on top and the waveguide on bottom via grating assisted coupling. (b) Transmission spectrum of a plane wave through 5 periods of the 2D photonic crystal slab, with inset showing the band diagram. (c) 2D FDTD simulation of the same structure but with 5 periods of 2D PC between the two corrugated waveguides showing effective crosstalk suppression.

FAR FIELD IMAGING RESULTS AND DISCUSSION

The device is fabricated on SOI with a top silicon layer of 250nm and 3μm Buried Oxide (BOX). The photonic circuit is patterned in a single step by electron beam lithography and reactive ion etching (RIE). Top down SEMs of the corrugated waveguide without and with photonic crystal are shown in Figure 38(a) and (b), respectively, while the top down SEM of the fiber to waveguide wideband input grating coupler is shown in Figure 38(c).

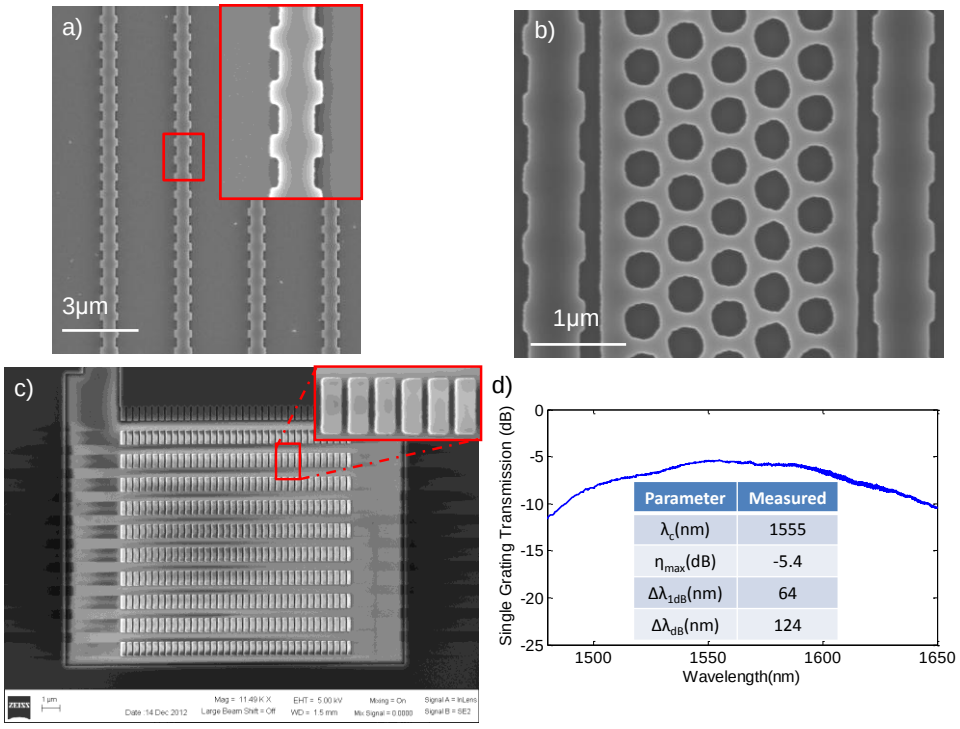

Figure 38-Top down SEM of the corrugated waveguide OPA (a) without and (b) with the 2D PC in between array elements. (c) Top down SEM of the input subwavelength grating coupler and (d) the input grating's transmission spectrum.

To characterize our device, TE polarized light from a polarization maintaining fiber (PMF) is coupled into the input grating coupler. The transmission spectrum of the input grating coupler is shown in Figure 38(d) and provides a 3dB bandwidth of 124nm with a maximum coupling efficiency η_{max}=-5.4dB at a central wavelength of λ_c=1555nm, which is sufficient to fully cover our wavelength tuning range. The far field pattern is directly observed on an IR CCD that is suspended above the device.

We first observe the far field pattern of a single corrugated waveguide, which forms the steering envelope for the array. By tuning the wavelength from 1480nm to 1580nm in 10nm steps, we observe the expected steering of the far fields as shown in the

IR images in Figure 39(a). The beam profiles in the longitudinal direction (θ) are shown in Figure 39(b), and the steering angle with the Full Width Half Maximum (FWHM) beam widths are shown in Figure 39(c). It can be seen that the average beam width in this steering range is ~0.3°, which is the smallest beam width for silicon based OPAs demonstrated to date.

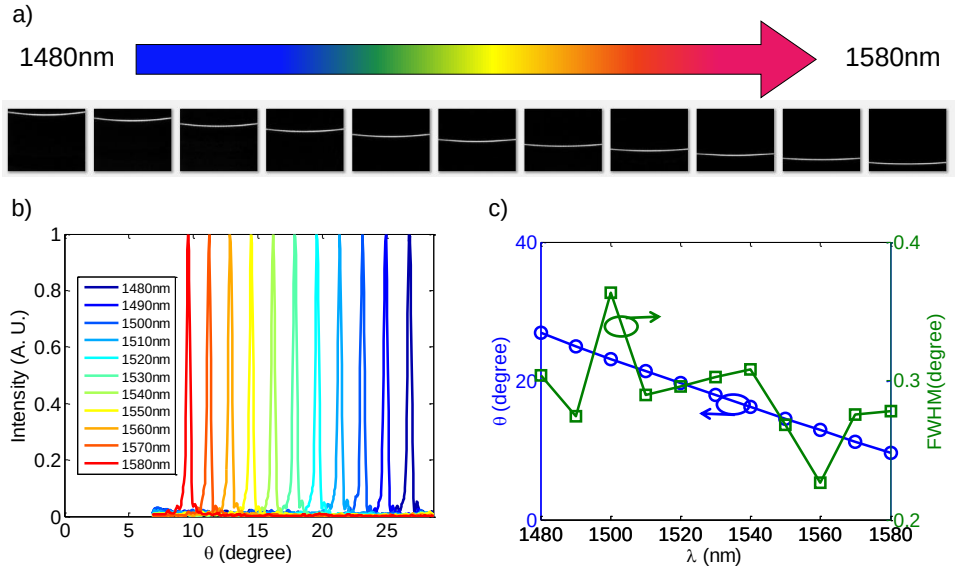

Figure 39-(a) IR CCD image of the far field of a single corrugated waveguide as the wavelength is tuned from 1480nm to 1580nm in 10nm steps. (b) Elevational beam profiles of the steered beam at different wavelengths. (c) Steered angle and FWHM beam width of the corrugated waveguide grating at different wavelengths.

The two OPAs with and without the photonic crystal isolators were then tested. Figure 40(a) shows the far field pattern of the 16 element OPA with 4 micron spacing without any photonic crystal in between. Multiple bands in the far field across θ are present and indicate light with different effective indices being emitted. This is due to optical crosstalk and the associated supermodes which have slightly different propagation constants from each other. According to the phase matching condition, these small

differences in effective refractive index will cause the light to be emitted at slightly different angles and ultimately scramble the far field pattern. Figure 40(b) shows the far field of an OPA with identical element spacing and 2D photonic crystal inserted between each array element. Only a single spot is present, which demonstrates that the photonic crystal is successful in blocking the laterally coupled light from the corrugated waveguides, thereby preventing optical crosstalk. The intensity profiles for the θ and ψ (XY plane) directions are shown in Figure 40(c), The presence of the small sidelobes in the ψ direction is due to phase errors from fabrication imperfections and can be reduced with thermo-optic phase tuning as demonstrated by [1-2].

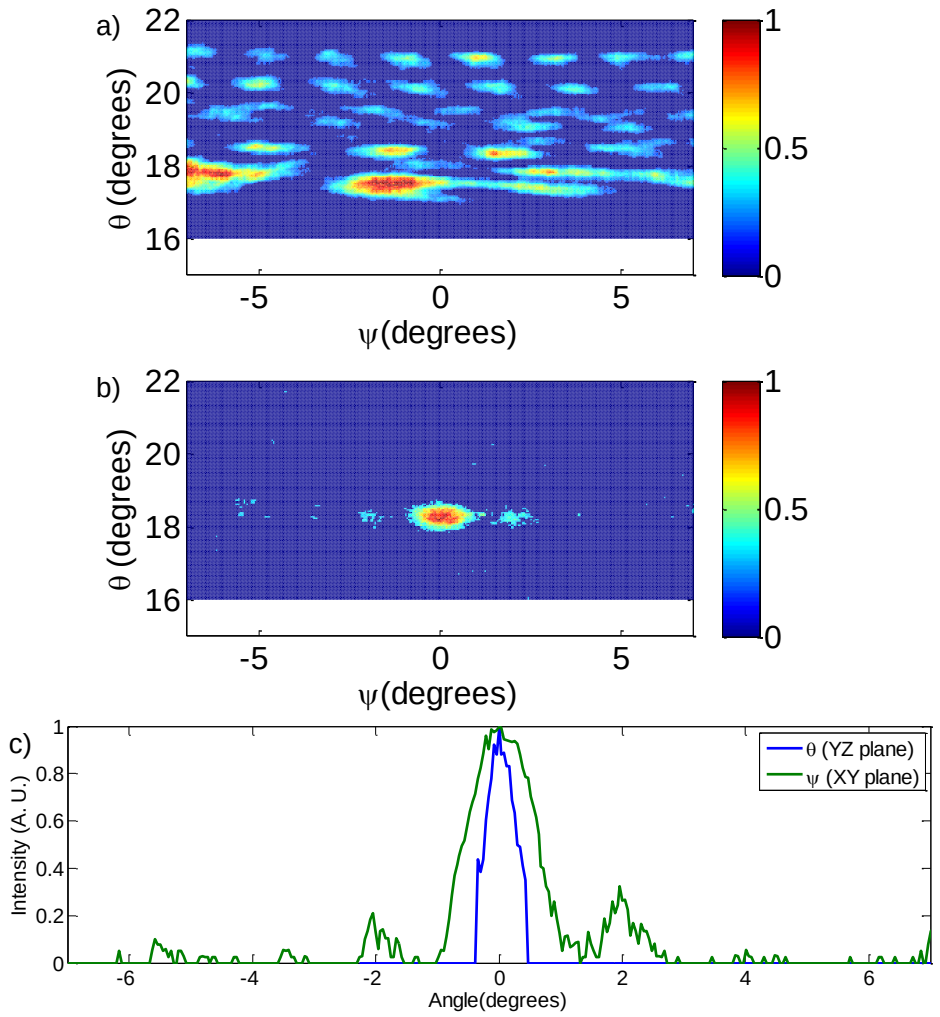

Figure 40-Far field of the 16 element corrugated waveguide array (a) without and (b) with 2D PC crosstalk suppression. (c) Azimuthal and elevational beam profiles of the far field with 2D PC.

SUMMARY

In conclusion, we present a grating coupler using corrugated waveguides whose index contrast is lithographically determined and can be fabricated in a single patterning step. Using wavelength tuning, we demonstrate 15° of steering with an average FWHM beam width of 0.3°, which is the lowest demonstrated to date. In addition, we demonstrate a novel method of suppressing the optical crosstalk from grating assisted

coupling between adjacent corrugated waveguide elements by placing 2D PC. This crosstalk isolation is demonstrated by the difference in far fields between a 16 element passive array with and without photonic crystal. Such a structure can be combined with thermo-optic phase shifters to achieve 2D beam steering with narrow beam widths and low power consumption.

REFERENCES

1. Karel Van Acoleyen, Wim Bogaerts, Jana Jágerská, Nicolas Le Thomas, Romuald Houdré, and Roel Baets, "Off-chip beam steering with a one-dimensional optical phased array on silicon-on-insulator," Opt. Lett. 34, 1477-1479 (2009).
2. J. K. Doylend, M. J. R. Heck, J. T. Bovington, J. D. Peters, L. A. Coldren, and J. E. Bowers, "Two-dimensional free-space beam steering with an optical phased array on silicon-on-insulator," Opt. Express 19, 21595-21604 (2011).
3. J. Sun, E. Timurdogan, A. Yacobi, E. S. Hosseini, and M. R. Watts, "Large scale nanophotonic phased array," Nature 493, 195-199 (2013).
4. W. Shi, X. Wang, W. Zhang, H. Yun, C. Lin, L. Chrostowski, and N. A. F. Jaeger, "Grating-coupled silicon microring resonators," Appl. Phys. Lett. 100, 121118 (2012)
5. Amir Hosseini, David Kwong, Yang Zhao, Yun-Sheng Chen, and Ray T. Chen, Unequally-spaced Waveguide Arrays for Silicon Nano-membrane-based Efficient Large Angle Optical Beam Steering, IEEE Journal of Selected Topics in Quantum Electronics, vol. 15, no. 5, 1439-1446, 2009.
6. Xia Chen, Ke Xu, Zhenzhou Cheng, Christy K. Y. Fung, and Hon K. Tsang, "Wideband subwavelength gratings for coupling between silicon-on-insulator waveguides and optical fibers," Opt. Lett. **37**, 3483-3485 (2012)

Chapter 9: Two Dimensional Beam Steering Using a Silicon Optical Phased Array with Polycrystalline Silicon Overlay

INTRODUCTION

Optical phased arrays (OPAs) can provide agile and precise free space optical beam steering free of any moving parts. Potential applications include free-space board-to-board optical interconnects [1] and light detection and ranging (LIDAR). By using the silicon-on-insulator (SOI) platform and leveraging existing CMOS fabrication processes and techniques, complex photonic circuits can be easily integrated on chip to reduce both the size and packaging complexity of silicon photonic devices. This enables compact silicon based OPAs to be realized.

Recent silicon based OPAs have used a combination of wavelength tuning and thermo-optic (TO) phase shifting to achieve two dimensional optical beam steering [2,3]. Free space emission was achieved using shallow etched surface gratings to reduce a silicon grating's inherently large index contrast, allowing for narrower longitudinal beam widths via larger emission apertures. However, precise control of the etch depth is required for shallow etched gratings. Acoleyen et al achieved a longitudinal beam width of ~2.5° by shallow etching 70nm of the 220nm silicon device layer [Acoleyen09]. Doylend et al used a significantly thicker silicon layer of 500nm and shallow etched the output gratings by 75nm to achieve a longitudinal beam width of 0.6°. While using a thicker silicon layer can reduce the index contrast for a given etch depth, a significant disadvantage is that the power consumption for TO phase shifting is increased due to the increased waveguide volume. In addition, as the silicon thickness now supports multiple vertical modes, rib waveguides are needed for single mode propagation, thereby adding additional patterning steps, which increases cost and complexity. Moreover, the etch depth still must be precisely controlled. It is desirable to use a free space coupling

structure that relaxes fabrication precision while still adhering to silicon device thicknesses of ~250nm that only support a single vertical mode.

In this work we demonstrate 2D beam steering using both wavelength tuning and TO phase shifting with a 16 element OPA fabricated on SOI with a 250nm silicon device layer. The output coupling structure incorporates a polycrystalline silicon (polysilicon) overlay with an oxide etch stop layer to realize narrow far field beam widths while eliminating the need for precise shallow etching.

DESIGN

A schematic of the device is shown in Figure 41(a), and consists of several key components: a fiber to waveguide grating coupler, cascaded 1x2 multimode interference (MMI) optical beam splitters, metal TO phase shifters, and finally the output grating couplers with a polysilicon overlay.

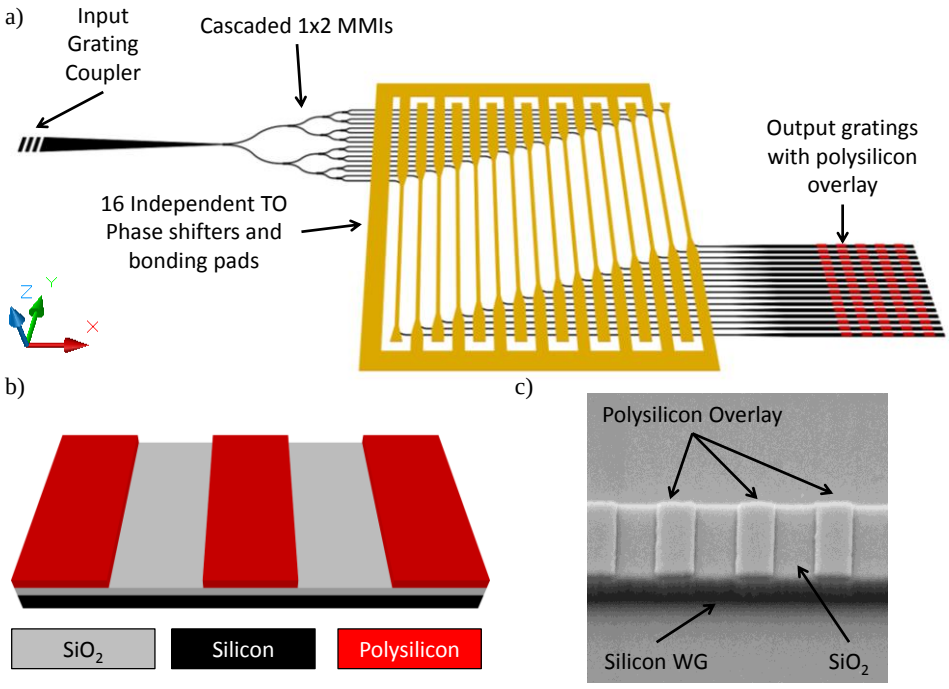

Figure 41 a) Schematic (not to scale) of the overall device. (b) Schematic and (c) SEM of a single waveguide grating with polysilicon overlay and oxide etch stop layer.

Light is first coupled into the photonic circuit using the input grating coupler. Compared to end fire coupling, grating couplers allow high coupling efficiency with large mis-alignment tolerances, while completely eliminating the need for any type of facet preparation. For this application, we have used subwavelength nanostructures in the grating couplers to reduce the index contrast in silicon gratings [4,5]. As our wavelength tuning range is from 1480-1580nm, it is important to utilize a grating coupler with a sufficiently wide bandwidth. This can be achieved by lowering the average effective index of the grating region in order to reduce the dispersion of the grating [5], such that the high index region of the grating is the subwavelength region and the low index region is the cladding.

Cascaded 1x2 MMI couplers are used to split the input light into 16 uniform outputs and provide a symmetric output phase profile such that the beam is steered at 0° without any thermal phase shifting. The 16 MMI outputswith 4μm spacing to 200μm spacing for TO phase shifting, and then a second 90° bend is used to reduce the waveguide separation back to 4μm for the OPA output. By using cascaded 1x2 MMI couplers and also keeping the optical path length the same for all array elements throughout the rest of the device, we allow for the array elements to have the same phase at the output, thereby ensuring the beam is steered at 0° without any thermal tuning.

Phase shifting is achieved using the thermo-optic effect in silicon (dn/dT=1.86E-4 K^{-1}), by placing metal heaters above the waveguide. The waveguide is separated from the metal heater by 1μm of silicon dioxide, which is sufficiently thick to prevent large absorption losses by isolating the guided mode from the metal. There are 16 independently controlled phase shifters to achieve resets with modulo 2π phase shifts, such that $2m\pi + \Delta\phi_i = \Delta\phi_i$, where *m* is an integer, and *i* is the channel number.

The output grating coupler shown in Figure 41(b) is an 800nm wide silicon waveguide covered with 20nm of silicon dioxide, which serves not only as an etch mask for patterning the silicon waveguide but also as an etch stop layer for patterning the 20nm polysilicon overlay due to the high selectivity of the silicon etch between silicon and silicon dioxide. This etch stop layer significantly relaxes the fabrication process in creating these surface gratings.

FABRICATION

The SOI has a 250nm silicon device layer with 3μm Buried Oxide (BOX) thickness. First, 20nm of silicon dioxide was deposited using Plasma Enhanced Chemical Vapor Deposition (PECVD). Next, 20nm of high quality amorphous silicon film was

deposited using Low Pressure Chemical Vapor Deposition (LPCVD) and was then subsequently annealed at 600°C for 10 hours, similar to our previous process in demonstrating ultra-low loss polysilicon films [6]. Standard electron-beam lithography and Reactive Ion Etching (RIE) were used to define the polysilicon grating lines, with the RIE etch stopping on the oxide layer below it due to the high selectivity of the silicon etch. After a Piranha clean for resist removal and substrate cleaning, ebeam lithography and RIE were used again to pattern the silicon device layer, which includes the input grating coupler, 1x2 MMIs ,and waveguides. A tilted SEM of the fabricated waveguide grating with the polysilicon overlay is shown in Figure 41(c). A top down SEM of the fiber to waveguide grating coupler using subwavlength nanostructures is shown in Figure 42(a). Afterwards, 1μm of LPCVD silicon dioxide was deposited for top cladding and passivation. The thermo-optic phase shifters were then patterned using lift-off of Cr/Au (5/150nm). Finally, the chip was mounted on a chip carrier to be plugged into a breadboard. Gold ball bonding was used to connect the bond pads on the chip with the electrical connections on the chip carrier. A microscope picture of the completed device, which measures 1mm X 9mm, is shown in Figure 42(b) and the wirebonded device on the chip carrier and breadboard is shown in Figure 42(c).

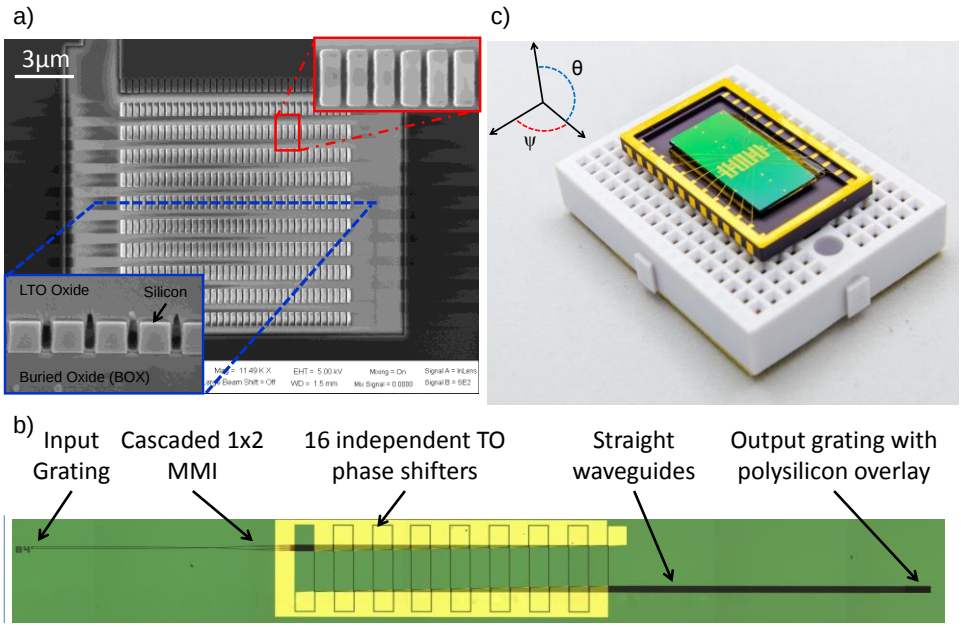

Figure 42 -(a) Top down SEM of the subwavelength grating coupler. Insets show magnified view (top right) and cross sectional view with oxide cladding (bottom left). (b) Microscope picture of the completed device. (c) Picture of the wirebonded device on the chip carrier plugged into a simple breadboard.

EXPERIMENTAL RESULTS AND DISCUSSION

The coupling efficiency of the subwavelength grating coupler was first determined by using input and output fibers to couple light in and out of two identical gratings connected by a straight waveguide. The transmission spectrum of a single grating coupler is shown in Figure 43(a), with a maximum coupling efficiency of η_{max}=-5.4dB at a central wavelength of λ_c=1555nm and a 3dB bandwidth of 124nm, which is large enough to cover our wavelength tuning range.

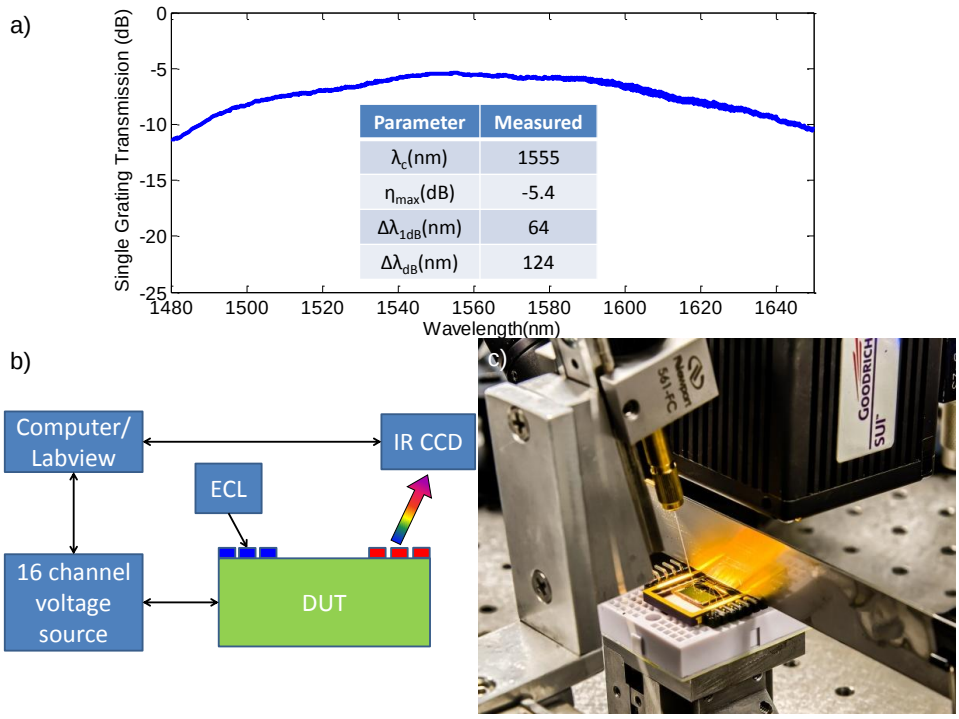

Figure 43-(a) Coupling efficiency of the wideband subwavelength grating coupler. (b) Schematic of the testing setup used to achieve 2D beam steering using the OPA. (c) Photograph of the testing setup showing the razor blade to block reflected light from entering the IR CCD.

To characterize the OPA beam steering and far field, the testing setup in Figure 43(b) is used. An external cavity laser (ECL) is used to couple light into the device via the input grating coupler. The emitted light from the output grating is directly imaged onto the IR CCD that is suspended above the device. A 16 channel independently controlled voltage source is used to control the phase of each array element. A LabVIEW equipped computer is used to optimize the applied voltage of each channel with continuous feedback from the IR CCD camera in order to achieve thermo-optically tuned beam steering. The figure of merit to be optimized is the emitted power efficiency, which is the power in the vicinity of the desired steering angle ψ compared with the total emitted power.

Before achieving active beam steering, we first use wavelength tuning to characterize the steering of a single waveguide grating, which forms the steering envelope of the array. The steering achieved by wavelength tuning is governed by the phase matching condition and is given by $sin(\theta) = \left(n_{eff,avg} \cdot \Lambda - \lambda\right)/(\Lambda \cdot n_{clad})$, where θ is the steered angle in the longitudinal direction, $n_{eff,avg}$ is the average effective index of the grating, Λ is the grating period, λ is the free space wavelength, and n_{clad} is the refractive index of the cladding. IR images of the steered beam as the wavelength is changed from 1480nm to 1580nm in 10nm steps are shown in Figure 44(a), along with the beam profiles in θ in Figure 44(b). The steering angle and Full Width Half Maxima (FWHM) beam width are shown in Figure 44(c). A total of 15° of steering was achieved with wavelength tuning, with an average beam width of ~0.5°, which is among the narrowest beam widths achieved to date, and indicates that our polysilicon overlay with the oxide etch stop layer is a more effective alternative to shallow etching.

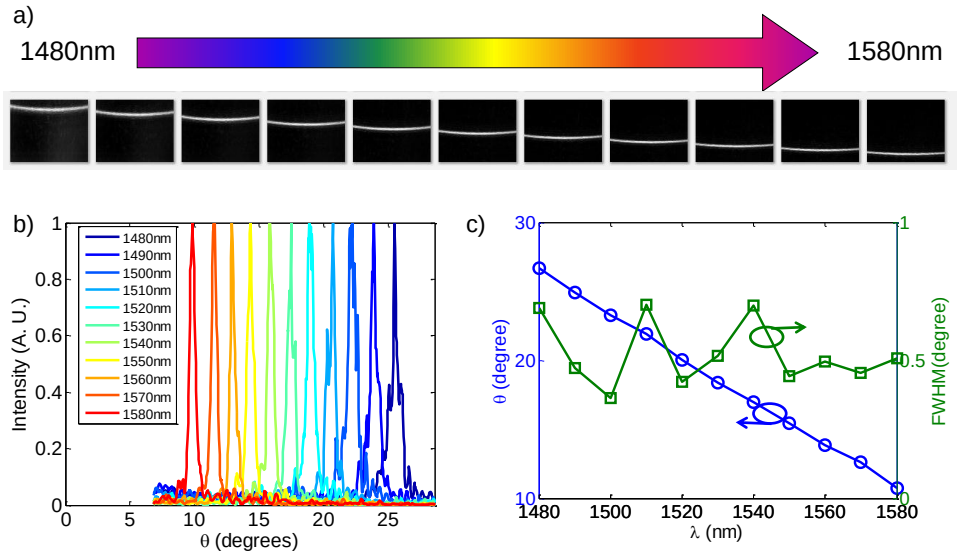

Figure 44- (a) IR CCD images of the single waveguide grating with polysilicon overlay as the wavelength is tuned from 1480nm to 1580nm. (b) Elevational beam profiles in θ of the steered beams. (c) Steering angle and FWHM beam width of the steered beam.

We also characterize the phase shifting properties of the metal heater by using a Mach-Zehnder Interferometer (MZI) with the same waveguide and heater dimensions as in the actual OPA. The switching power required for a π phase shift was determined to be P_π=20mW, as shown in Figure 45. In Figure 45(b) the transient response of the phase shifters was characterized, and a 10%-90% rise time was experimentally determined to be t_{rise}=48μs, corresponding to a 3dB modulation bandwidth of 7.3kHz.

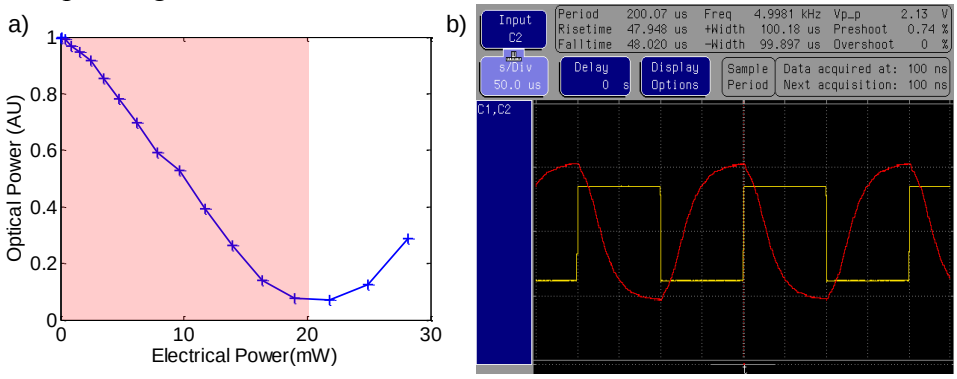

Figure 45- a) MZI transmission spectrum vs. electrical power to TO phase shifters. (b) Oscilloscope screenshot of MZI.

With the phase tuning efficiency of the heater characterized, it is now possible to achieve phase shifting in the azimuthal direction ψ. The steering in ψ for a uniform array is determined by $sin\psi = (\lambda\phi)/(2\pi d)$, where φ is the uniform phase difference between adjacent array elements, λ is the free space wavelength, and d is the element spacing. However, in the 16 element OPA, fabrication imperfections in the heaters can result in deviations of P_π from the previously determined value. It was therefore impractical to use the MZI heater characterization results for beam steering. A LabVIEW system with constant feedback between the 16 channel source and the IR CCD therefore provides a more feasible approach to beam steering.

At a wavelength of 1550nm, the OPA far field and line profile without any thermal phase shifting is shown in Figure 46(a) and (b), respectively. The presence of the main lobe at ~9° and additional side lobes indicates phase errors are present, despite attempts being made to reduce the phase errors through the use of cascaded 1x2 MMIs and equalized optical path lengths. It is believed that small, cumulative fabrication imperfections in the waveguides are inducing these phase errors. Therefore, thermal tuning is needed to correct these phase errors by using the LabVIEW eedback control system. The OPA far field and line profile after thermal tuning with a horizontal beam width of 1.1° is shown in Figure 46(c) and (d), and shows good agreement with the theoretical value of 1.2°.

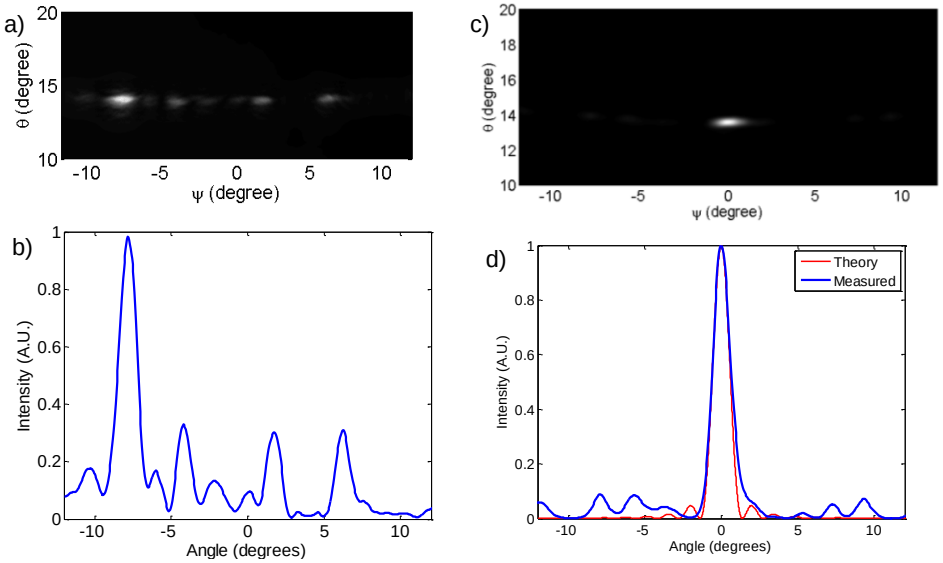

Figure 46-(a) OPA far field and (b) line profile without thermal tuning. (c) OPA far field and (d) line profile after thermal tuning.

Using the LabVIEW feedback control system, we steered the beam a total of 19.6° in the horizontal (ψ) direction, with a side lobe level (SLL) of more than 10dB throughout the steering range, as shown in Figure 47(a). In addition, the azimuthal and elevational beam widths are shown in Figure 47(b), with an average azimuthal beam

width of ~1.2°, and average elevational beam width of ~0.5°, which matches well with the single waveguide grating results.

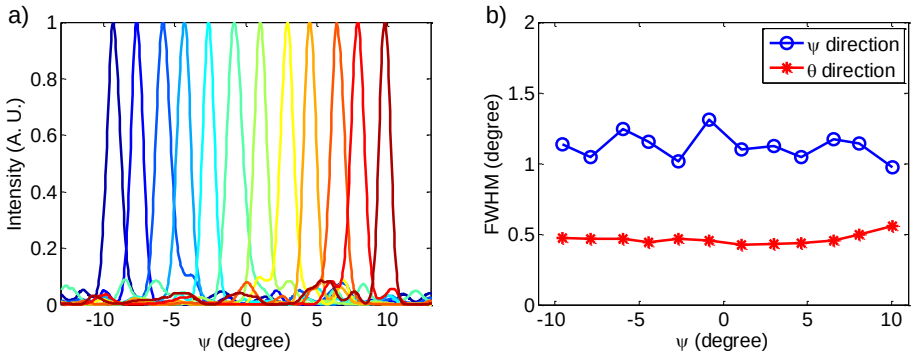

Figure 47-(a) 2D beam steering around a 20° X 15° field of view with SLL better than 10dB, and beam widths of 1.2° X 0.5°.

Combined with wavelength tuning, it is now possible to achieve 2D beam steering. This 2D beam steering can be seen in Figure 48, in which the beam is steered along the perimeter of the entire field of view, which is a rectangular area that is 20° in θ by 15° in ψ. The far fields of these steered beams are shown overlaid upon each other and show a SLL better than 10dB, with beam widths of 1.2° X 0.5°.

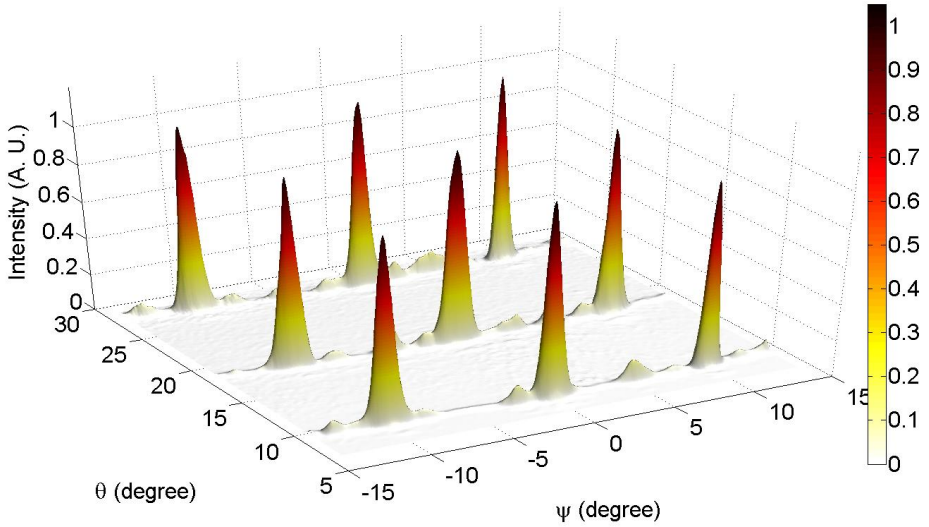

Figure 48-2D beam steering around a 20° X 15° field of view with SLL better than 10dB, and beam widths of 1.2° X 0.5°.

SUMMARY

In conclusion, we have demonstrated an integrated optical beam steering system using a 16 element optical phased array fabricated on SOI with a silicon device layer thickness of 250nm. 2D beam steering is achieved using a combination of wavelength tuning and TO phase shifting, with a maximum power consumption of $P_{2\pi}$=40mW per channel. The output coupling to free space is achieved using a thin polysilicon overlay. Compared to conventional shallow etched gratings, this structure removes the need for precisely controlled etching due to the built in oxide etch stop layer, thereby greatly simplifying the fabrication complexity. With this device, 2D steering across a 20° X 15° field of view has been demonstrated, with a SLL better than 10dB, and 1.2° X 0.5° beam widths.

REFERENCES

1. Henderson, C.J.; Leyva, D.G.; Wilkinson, T.D., "Free space adaptive optical interconnect at 1.25 Gb/s, with beam steering using a ferroelectric liquid-crystal SLM," *Lightwave Technology, Journal of* , vol.24, no.5, pp.1989,1997, May 2006
2. Karel Van Acoleyen, Wim Bogaerts, Jana Jágerská, Nicolas Le Thomas, Romuald Houdré, and Roel Baets, "Off-chip beam steering with a one-dimensional optical phased array on silicon-on-insulator," Opt. Lett. 34, 1477-1479 (2009)
3. J. K. Doylend, M. J. R. Heck, J. T. Bovington, J. D. Peters, L. A. Coldren, and J. E. Bowers, "Two-dimensional free-space beam steering with an optical phased array on silicon-on-insulator," Opt. Express 19, 21595-21604 (2011)
4. Xiaochuan Xu, Harish Subbaraman, John Covey, David Kwong, Amir Hosseini, and Ray T. Chen, "Complementary metal–oxide–semiconductor compatible high

efficiency subwavelength grating couplers for silicon integrated photonics," Appl. Phys. Lett. 101, 031109 (2012)

5. Xia Chen, Ke Xu, Zhenzhou Cheng, Christy K. Y. Fung, and Hon K. Tsang, "Wideband subwavelength gratings for coupling between silicon-on-insulator waveguides and optical fibers," Opt. Lett. 37, 3483-3485 (2012)
6. David Kwong, John Covey, Amir Hosseini, Yang Zhang, Xiaochuan Xu, and Ray T. Chen, "Ultralow-loss polycrystalline silicon waveguides and high uniformity 1x12 MMI fanout for 3D photonic integration," Opt. Express 20, 21722-21728 (2012)

Chapter 10: Summary and Future Work

A single layer large angle optical phased array has been designed and studied by my colleague Amir Hosseini. I have fabricated a low loss and high uniformity 1x12 MMI as one of the key components in the OPA. Thermo-Optic phase shifters have been designed and optimized to be integrated with the photonic layer. We experimentally demonstrate the silicon nanomembrane based large angle beam steering system.

Candidates for photonic materials suitable for multi-layer integration are studied. Hydrogenated amorphous silicon as a silicon photonic platform is optimized, and the loss of the material is characterized. A 1x12 MMI fabricated using amorphous silicon is presented for the first time. In addition, both double layer and 5 layer amorphous silicon slab waveguides are fabricated and initially found to be feasible for 3D integration. However, tool issues and the film instability prevented us from continuing to use amorphous silicon for a multi-layer OPA. We conclude that the film instability on hydrogenated amorphous silicon, specifically, the weakness of the Si-H bond and its effect on refractive index and propagation loss, is a limiting factor in making devices beyond simple waveguides, and that it is ultimately not suitable for our application.

Polysilicon was investigated as the next candidate for us. Through solid phase crystallization of LPCVD amorphous silicon, we obtain polysilicon films suitable for photonics. We experimentally find two regions of loss characteristics for polysilicon waveguides that depend on the waveguide width. In the single mode region, the loss is dominated by the bulk absorption loss, and larger waveguides with more confinement are more lossy than narrow waveguides with less confinement. The second region is interface

loss dominated, where larger waveguides experience less loss. This result vindicates the use of polysilicon for large devices such as MMIs. We also fabricate the first 1x12 MMI on polysilicon. More work is needed to not only optimize the 1x12 polysilicon MMI, but also to determine the exact mechanism for the loss dependence on waveguide width, specifically why there are two different regions of loss dominated by different effects.

Grating couplers for coupling of light from single mode fibers to nanophotonic silicon waveguides are also presented. Using subwavelength structures with SU-8 top cladding, we demonstrate a SWG coupler centered at 1550nm with a 3dB bandwidth of 53nm and a peak coupling efficiency of ~20%.

Methods towards achieving 2D beam steering without shallow etching have been explored. In the first approach, corrugated waveguides which are defined using a single etch step have been demonstrated for free space emission with ~0.3° longitudinal beam width, which is narrowest beam widths demonstrated to date using silicon photonic devices. To avoid the optical crosstalk and the formation of supermodes that scramble the far field when the spacing in an array of corrugated waveguides is reduced, 2D photonic crystal is placed between each corrugated waveguide. This photonic crystal has a bandgap which covers the wavelength region of operation (1480-1580nm), thereby providing optical isolation of each array element. This crosstalk suppression has been verified in a 16 element OPA of corrugated waveguides with 2D PC in between each element.

A second approach was also investigated and does not use shallow etching. In this approach, a polysilicon overlay is used to create a grating on top of a crystalline silicon

waveguide. Sandwiched between the polysilicon and crystalline silicon is a thin oxide layer, which serves as the etch stop layer for the polysilicon etch. This approach creates a surface grating similar to shallow etched grating, but the oxide etch stop layer negates the need for any precise etching. By depositing thin polysilicon layers, the index contrast in the grating can also be minimized, thereby increasing the effective emission aperture of the grating and thus resulting in narrow far field beam widths. With this approach, we demonstrate 2D beam steering using both wavelength tuning and thermo-optic phase shifting. Steering throughout a 20° x 15° field of view has been demonstrated, with horizontal and longitudinal beam widths of 1.2° and 0.5°, respectively.

The OPA presented here and other recently presented OPAs have demonstrated 2D beam steering for near-IR wavelengths, in the telecommunication band around 1550nm. Recent efforts have been made to extend the operating wavelength region of silicon photonics to the mid-IR region, from 3-7μm. In this region, the negative effects of two photon absorption (TPA) which include limited output power, and excess heat generation, are reduced. This is a significant advantage for defense applications, as they generally require high optical power for operation. In addition, the region from 3-5μm is an atmospheric transparency window, where molecular and particulate scattering is reduced compared to near-IR operations.

While silicon itself has a large transparency window from 1.1-9μm, the SOI platform is not suitable anymore. Silicon dioxide itself becomes absorptive around ~3.6μm, and substrate leakage also becomes increasingly important. An alternative is the silicon-on-sapphire (SOS) platform, as sapphire has optical transparency up to ~4.5μm.

Furthermore, as the entire substrate is sapphire, substrate coupling issues are eliminated. While the SOS platform is relatively new and perhaps less understood, it is expected that the learning achieved from SOI process technologies can be applied for SOS processing. Recent progress in mid-IR silicon photonic components includes basic components such as grating couplers, low loss waveguides, photonic crystals, and ring resonators. Other components that are present in our current OPA but currently not developed for mid-IR operation on SOS include low loss and high uniformity beam splitters using y-branches or MMIs, and thermo-optic modulators and switches.

A possible area of future work is therefore to create an optical beam steering system on SOS for mid-IR operation. Many of the photonic components can simply be redesigned for mid-IR wavelengths. One key advantage of moving to longer wavelengths is the device footprint also increases, thereby relaxing lithographic and other fabrication patterning challenges. The creation of such a system would further advance optical beam steering technologies based on integrated silicon photonics.

Bibliography

1. Stuart (Shizhuo) Yin, Jae Hun Kim, Fei Wu, Paul Ruffin, Claire (Fang) Luo, Ultra-fast speed, low grating lobe optical beam steering using unequally spaced phased array technique, Optics Communications, Volume 270, Issue 1, 1 February 2007, Pages 41-46.
2. Jarrahi, Mona; Pease, R. Fabian W.; Miller, David A. B.; Lee, Thomas H.; , "Optical switching based on high-speed phased array optical beam steering," Applied Physics Letters , vol.92, no.1, pp.014106-014106-3, Jan 2008.
3. McManamon, P.F.; Dorschner, T.A.; Corkum, D.L.; Friedman, L.J.; Hobbs, D.S.; Holz, M.; Liberman, S.; Nguyen, H.Q.; Resler, D.P.; Sharp, R.C.; Watson, E.A.; , "Optical phased array technology," Proceedings of the IEEE , vol.84, no.2, pp.268-298, Feb 1996
4. R. A. Meyer, "Optical Beam Steering Using a Multichannel Lithium Tantalate Crystal," Appl. Opt. 11, 613-616 (1972)
5. Ninomiya, Y.; , "Ultrahigh resolving electrooptic prism array light deflectors," Quantum Electronics, IEEE Journal of , vol.9, no.8, pp. 791- 795, Aug 1973
6. Amir Hosseini, David N Kwong, and Ray T. Chen, Wide steering angle optical phased array based on silicon nano-membrane, Proc. SPIE 7221, 72210T (2009)
7. Amir Hosseini, David N. Kwong, Che-Yun Lin, Beom Suk Lee, and Ray T. Chen, Output Formulation for Symmetrically-Excited one-to-N Multimode Interference Coupler, IEEE Journal of selected topics in quantum electronics, to appear (2010)
8. L. Soldano and E. Pennings, "Optical multi-mode interference devices based on self-imaging: Principles and applications," J. Lightw. Technol., vol. 13, no. 4, pp. 615–627, Apr. 1995.
9. Rajarajan, M., Rahman, B. M. A., And Grattan, K. T. V.: 'Accurate Numerical Analysis of Multimode-Interference-Based 3-dB Couplers', Appl. Opt., 1998, 37, pp. 5672-5678
10. Ulrich, R., And Kamiya, T.: 'Resolution of self-images in planar optical waveguides', J. Opt. Soc. Am., 1978, 68, pp. 583-592
11. Huang, J.Z., Scarmozzino, R., And Osgood Jr., R.M.: 'A new design approach to large input/output number multimode interference couplers and its application to low-crosstalk WDM routers', IEEE Photonics Technology Letters IEEE, 1998, 10, 9, pp. 1292-1294
12. Acoleyen, K.V., Bogaerts, W., Jágerská, J., Le Thomas, N., Houdré, R., And Baets, R.: 'Off-chip beam steering with a one-dimensional optical phased array on silicon-on-insulator', Opt. Lett., 2009, 34, pp. 1477-1479
13. Vlasov, Y., And Mcnab, S.: 'Losses in single-mode silicon-on-insulator strip waveguides and bends', Opt. Express, 2004, 12, pp. 1622-1631
14. Soldano, L., And Pennings, E.: 'Optical multi-mode interference devices based on self-imaging: principles and applications', J. Lightwave Technology, 1995, 13, 4, pp. 615–627
15. Hosseini, A., Kwong, D.N., Lin, C.Y., Lee, B. S., And Chen, R.T.: 'Output Formulation for Symmetrically-Excited one-to-N Multimode Interference Coupler', IEEE Journal of Selected Topics in Quantum Electronics, 2010, 6, 1, pp. 53-60
16. Y. Pétremand, P.-A. Clerc, M. Epitaux, R. Hauffe, W. Noell, and N. F. de Rooij, Proc. SPIE 6715, 671502 (2007).

17. P.F. McManamon, T. A. Dorschner, D. L. Corkum, L. J. Friedman, D. S. Hobbs, M. Holz, S. Liberman, H. Q. Nguyen, D. P. Resler, R. C. Sharp, and E. A Watson, Proc. IEEE 84(2), 268–298 (1996).
18. X. Wang, B. Wang, J. Pouch, F. Miranda, J. E. Anderson, and P. J. Bos, Opt. Eng. 43, 2769-2774 (2004).
19. X. Wang X., B. Wang B., P. Bos, P. F. McManamon, J. J. Pouch , F. A. Miranda, and J. E. Anderson, J. Appl. Phys. 98, 073101 (2005).
20. A. Hosseini, D. N. Kwong, Y. Zhao, Y. –S Chen, F. Crnogorac, R. F. W. Pease, and R. T. Chen, IEEE J. Sel. Topics Quant. elect. 15(5), 1439-1446 (2009).
21. M. Jarrahi, R. F. W. Pease, D. A. B. Miller, and T. H. Lee, J. Vac. Sci. Technol. B 26, 2124-2126 (2008).
22. K. V. Acoleyen, W. Bogaerts, J. Jágerská, N. Le Thomas, R. Houdré, and R. Baets, Opt. Lett. 34, 1477-1479 (2009).
23. A. Hosseini, H. Subbaraman, D. N. Kwong, Y. Zhang, and R. T. Chen, Opt. Lett. 35, 2864-2866 (2010).
24. D. N. Kwong, Y. Zhang, A. Hosseini, Y. Liu, and R. T. Chen, IET Electronics Letters, 46(18), 1281-1283, (2010).
25. I. M. Soganci, T. Tanemura, K. A.Williams, N. Calabretta, T. de Vries, E. Smalbrugge, M. K. Smit, H. Dorren, and Y. Nakano, IEEE Photonics Technology Letters, 22(3), 143-145 (2010).
26. A. Hosseini , D. N. Kwong, Ch.-Y. Lin,B. S. Lee, and R. T. Chen, IEEE J. Sel. Topics Quant. elect. 16(1), 61-69 (2010).
27. A. Hosseini, D. N. Kwong, Y. Zhang, A. Alu, and R. T. Chen, Appl. Opt. 50(13), 1822-1826 (2011).
28. Shiyang Zhu, G. Q. Lo, and D. L. Kwong, "Low-loss amorphous silicon wire waveguide for integrated photonics: effect of fabrication process and the thermal stability," Opt. Express **18**, 25283-25291 (2010).
29. S. Y. Zhu, Q. Fang, M. B. Yu, G. Q. Lo, and D. L. Kwong, "Propagation losses in undoped and n-doped polycrystalline silicon wire waveguides," Opt. Express 17(23), 20891–20899 (2009).
30. S. Y. Zhu, G. Q. Lo, J. D. Ye, and D. L. Kwong, "Influence of RTA and LTA on the optical propagation loss in polycrystalline silicon wire waveguides," IEEE Photon. Technol. Lett. 22(7), 480–482 (2010).
31. Q. Fang, J. F. Song, S. H. Tao, M. B. Yu, G. Q. Lo, and D. L. Kwong, "Low loss (~6.45dB/cm) sub-micron polycrystalline silicon waveguide integrated with efficient SiON waveguide coupler," Opt. Express 16, 6425-6432 (2008) .
32. S. K. Selvaraja, E. Sleeckx, M. Schaekers, W. Bogaerts, D. V. Thourhout, P. Dumon, and R. Baets, "Low-loss amorphous silicon-on-insulator technology for photonic integrated circuitry," Opt. Commun. 282(9), 1767–1770 (2009).
33. T. Lipka, A. Harke, O. Horn, J. Amthor, and J. Muller, "Amorphous waveguides for high index photonic circuitry," in Optical Fiber Communication Conference, OSA Technical Digest (CD) (Optical Society of America, 2009), paper OMJ2.

34. D. N. Kwong, Y. Zhang, A. Hosseini, Y. Liu, and R. T. Chen, "1x12 even fanout using multimode interference optical beam splitter on silicon nanomembrane,"IET Electronics Letters, 46(18), 1281-1283, (2010).
35. Shankar Kumar Selvaraja, Wim Bogaerts, Dries VanThourhout, and Marc Schaekers, "Thermal trimming and tuning of hydrogenated amorphous silicon nanophotonic devices," Appl. Phys. Lett. 97, 071120 (2010)
36. T. Lipka, A. Harke, O. Horn, J. Amthor, and J. Muller, "Amorphous Silicon as High Index Photonic Material," Proceedings Proc. SPIE 7366, 73661Z (2009)
37. N.H. Nickel, W.B. Jackson, I.W. Wu, C.C. Tsai, and A. Chiang, "Hydrogen permeation through thin silicon oxide films," Phys. Rev. B 52, 7791–7794 (1995).
38. Nicolás Sherwood-Droz and Michal Lipson, "Scalable 3D dense integration of photonics on bulk silicon," Opt. Express **19**, 17758-17765 (2011).
39. C. W. Holzwarth, J. S. Orcutt, H. Li, M. A. Popovic, V. Stojanovic, J. L. Hoyt, R. J. Ram, and H. I. Smith, "Localized Substrate Removal Technique Enabling Strong-Confinement Microphotonics in Bulk Si CMOS Processes," in Conference on Lasers and Electro-Optics/Quantum Electronics and Laser Science Conference and Photonic Applications Systems Technologies, OSA Technical Digest (CD) (Optical Society of America, 2008), paper CThKK5.
40. JoonHyun Kang, Yuki Atsumi, Manabu Oda, Tomohiro Amemiya, Nobuhiko Nishiyama and Shigehisa Arai, "Low-Loss Amorphous Silicon Multilayer Waveguides Vertically Stacked on Silicon-on-Insulator Substrate," Jpn. J. Appl. Phys. **50,** 120208 (2011).
41. Shiyang Zhu, G. Q. Lo, and D. L. Kwong, "Low-loss amorphous silicon wire waveguide for integrated photonics: effect of fabrication process and the thermal stability," Opt. Express **18**, 25283-25291 (2010).
42. Shankar Kumar Selvaraja, Wim Bogaerts, Dries VanThourhout, and Marc Schaekers, "Thermal trimming and tuning of hydrogenated amorphous silicon nanophotonic devices," Appl. Phys. Lett. **97**, 071120 (2010).
43. T. Kamins, Polycrystalline Silicon for Integrated Circuits and Displays, 2nd ed. (Kluwer, 1998).
44. Shiyang Zhu, Q. Fang, M. B. Yu, G. Q. Lo, and D. L. Kwong, "Propagation losses in undoped and n-doped polycrystalline silicon wire waveguides," Opt. Express **17**, 20891-20899 (2009).
45. Q. Fang, J. F. Song, S. H. Tao, M. B. Yu, G. Q. Lo, and D. L. Kwong, "Low loss (~6.45dB/cm) sub-micron polycrystalline silicon waveguide integrated with efficient SiON waveguide coupler," Opt. Express **16**, 6425-6432 (2008).
46. Kyle Preston, Bradley Schmidt, and Michal Lipson, "Polysilicon photonic resonators for large-scale 3D integration of optical networks," Opt. Express **15**, 17283-17290 (2007).
47. Kyle Preston, Sasikanth Manipatruni, Alexander Gondarenko, Carl B. Poitras, and Michal Lipson, "Deposited silicon high-speed integrated electro-optic modulator," Opt. Express **17**, 5118-5124 (2009).
48. L. Liao, D. R. Lim, A. M. Agarwal, X. Duan, K. K. Lee, and L. C. Kimerling, "Optical transmission losses in polycrystalline silicon strip waveguides: effects of waveguide

dimensions, thermal treatment, hydrogen passivation, and wavelength," J. Electron. Mater. **29**(12), 1380–1386 (2000).
49. Jason S. Orcutt, Sanh D. Tang, Steve Kramer, Karan Mehta, Hanqing Li, Vladimir Stojanović, and Rajeev J. Ram, "Low-loss polysilicon waveguides fabricated in an emulated high-volume electronics process," Opt. Express **20**, 7243-7254 (2012).
50. Hosseini, A.; Kwong, D.N.; Yang Zhang; Subbaraman, H.; Xiaochuan Xu; Chen, R.T., "1xN multimode interference beam splitter design techniques for on-chip optical interconnections," IEEE Jounal of Selected Topics in Quantum Electronics **17**, 510-515 (2011).
51. P. Dumon, W. Bogaerts, D. Van Thourhout, D. Taillaert, R. Baets, J. Wouters, S. Beckx, and P. Jaenen, "Compact wavelength router based on a Silicon-on-insulator arrayed waveguide grating pigtailed to a fiber array," Opt. Express **14**, 664-669 (2006).
52. Hatalis, Miltiadis K.; Greve, David W.; , "Large grain polycrystalline silicon by low-temperature annealing of low-pressure chemical vapor deposited amorphous silicon films," Journal of Applied Physics, **63,** 2260-2266, (1988).
53. Effiong Ibok and Shyam Garg, "A Characterization of the Effect of Deposition Temperature on Polysilicon Properties," J. Electrochem. Soc. **140**, 2927 (1993).
54. Yurii Vlasov and Sharee McNab, "Losses in single-mode silicon-on-insulator strip waveguides and bends," Opt. Express **12**, 1622-1631 (2004).
55. Mauro J. Kobrinsky, Bruce A. Block, Jun-Fei Zheng, Brandon C. Barnett, Edris Mohammed, Miriam Reshotko, Frank Robertson, Scott List, Ian Young, Kenneth Cadien, "On-Chip Optical Interconnects," Intel Technology Journal, **8**, 129-142 (2004).
56. Kwong, D.; Zhang, Y.; Hosseini, A.; Liu, Y.; Chen, R.T.; , "1 X 12 even fanout using multimode interference optical beam splitter on silicon nanomembrane," Electronics Letters, **46**, 1281-1283 (2010).
57.]D. Taillaert, "Grating couplers for coupling between optical fibers and nanophotonic waveguides," Jpn. J. Appl. Phys. 45, 6071-6077(2006)
58. G. Roelkens, "High efficiency diffractive grating couplers for interfacing a single mode optical fiber with a nanophotonic silicon-on-insulator waveguide circuit," Appl. Phys. Lett. 92, 131101(2008)
59. R. Halir et al, "Continuously apodized fiber-to-chip surface grating coupler with refractive index engineered subwavelength structure," Optics Letters 35, 3243-3245(2010)
60. Karel Van Acoleyen, Wim Bogaerts, Jana Jágerská, Nicolas Le Thomas, Romuald Houdré, and Roel Baets, "Off-chip beam steering with a one-dimensional optical phased array on silicon-on-insulator," Opt. Lett. 34, 1477-1479 (2009).
61. J. K. Doylend, M. J. R. Heck, J. T. Bovington, J. D. Peters, L. A. Coldren, and J. E. Bowers, "Two-dimensional free-space beam steering with an optical phased array on silicon-on-insulator," Opt. Express 19, 21595-21604 (2011).
62. J. Sun, E. Timurdogan, A. Yacobi, E. S. Hosseini, and M. R. Watts, "Large scale nanophotonic phased array," Nature 493, 195-199 (2013).
63. W. Shi, X. Wang, W. Zhang, H. Yun, C. Lin, L. Chrostowski, and N. A. F. Jaeger, "Grating-coupled silicon microring resonators," Appl. Phys. Lett. 100, 121118 (2012)

64. Amir Hosseini, David Kwong, Yang Zhao, Yun-Sheng Chen, and Ray T. Chen, Unequally-spaced Waveguide Arrays for Silicon Nano-membrane-based Efficient Large Angle Optical Beam Steering, IEEE Journal of Selected Topics in Quantum Electronics, vol. 15, no. 5, 1439-1446, 2009.
65. Xia Chen, Ke Xu, Zhenzhou Cheng, Christy K. Y. Fung, and Hon K. Tsang, "Wideband subwavelength gratings for coupling between silicon-on-insulator waveguides and optical fibers," Opt. Lett. **37**, 3483-3485 (2012)
66. Henderson, C.J.; Leyva, D.G.; Wilkinson, T.D., "Free space adaptive optical interconnect at 1.25 Gb/s, with beam steering using a ferroelectric liquid-crystal SLM," *Lightwave Technology, Journal of* , vol.24, no.5, pp.1989,1997, May 2006
67. Karel Van Acoleyen, Wim Bogaerts, Jana Jágerská, Nicolas Le Thomas, Romuald Houdré, and Roel Baets, "Off-chip beam steering with a one-dimensional optical phased array on silicon-on-insulator," Opt. Lett. 34, 1477-1479 (2009)
68. J. K. Doylend, M. J. R. Heck, J. T. Bovington, J. D. Peters, L. A. Coldren, and J. E. Bowers, "Two-dimensional free-space beam steering with an optical phased array on silicon-on-insulator," Opt. Express 19, 21595-21604 (2011)
69. Xiaochuan Xu, Harish Subbaraman, John Covey, David Kwong, Amir Hosseini, and Ray T. Chen, "Complementary metal–oxide–semiconductor compatible high efficiency subwavelength grating couplers for silicon integrated photonics," Appl. Phys. Lett. 101, 031109 (2012)
70. Xia Chen, Ke Xu, Zhenzhou Cheng, Christy K. Y. Fung, and Hon K. Tsang, "Wideband subwavelength gratings for coupling between silicon-on-insulator waveguides and optical fibers," Opt. Lett. 37, 3483-3485 (2012)
71. David Kwong, John Covey, Amir Hosseini, Yang Zhang, Xiaochuan Xu, and Ray T. Chen, "Ultralow-loss polycrystalline silicon waveguides and high uniformity 1x12 MMI fanout for 3D photonic integration," Opt. Express 20, 21722-21728 (2012)

Publications

JOURNAL PAPERS:

1. D. Kwong, J. Covey, A. Hosseini, Y. Zhang, X. Xu, and R. T. Chen, "Ultralow-loss polycrystalline silicon waveguides and high uniformity 1x12 MMI fanout for 3D photonic integration," Opt. Express 20, 21722-21728 (2012)
2. D. Kwong, A. Hosseini, Y. Zhang, R. T. Chen, "1x12 Unequally-Spaced Waveguide Array For Actively-Tuned Optical Phased Array On A Silicon Nanomembrane," Applied Physics Letters, Vol. 99, pp. 051104, 2011
3. D. Kwong, Y. Zhang, A. Hosseini, R. T. Chen "1x12 Even Fanout Using Multimode Interference Optical Beam Splitter On Silicon Nanomembrane," Electronics Letters, Vol. 46, No. 18, Pp. 1281-1283, 2010
4. Y. Zhang, D. Kwong, X. Xu, A. Hosseini, and R. T. Chen, "On-chip double-layer crystalline silicon nanomembane and inter-layer grating coupler for 3D photonic integration," to appear in Applied Physics Letters.
5. Y. Zou, S. Chakravarty, D. Kwong, W. Lai, X. Xu, Y. Guo, A. Hosseini, and R. T. Chen, "High yield high sensitivity silicon based photonic crystal microcavity biosensors," under review at Optics Express.
6. X. Xu, H. Subbaraman, J. Covey, D. Kwong, A. Hosseini, and R. T. Chen, "Complementary metal–oxide–semiconductor compatible high efficiency subwavelength grating couplers for silicon integrated photonics," Appl. Phys. Lett. 101, 031109 (2012)
7. X. Xu, H. Subbaraman, A. Hosseini, C.-Y. Lin, D. Kwong, And R. T. Chen, "Stamp Printing Of Silicon Nanomembrane Based Photonic Devices Onto Flexible Substrates With A Suspended Configuration," Optics Letter, Vol. 37, No. 6, Pp. 1020-1022, 2012
8. A. Hosseini, S. Rahimi, X. Xu, D. Kwong, J. Covey, And R. T. Chen, "Ultracompact And Fabrication-Tolerant Integrated Polarization Splitter," Optics Letters, Vol. 36, No. 20, Pp. 4047-4049, 2011
9. A. Hosseini, D. Kwong, Y. Zhang, A. Alu, And R. T. Chen, "Modeling And Experimental Observation Of On-Chip Two-Dimensional Far Field Interference Pattern," Applied Optics, Vol. 50, Pp. 1822-1826, 2011
10. A. Hosseini, D. Kwong, Y. Zhang, H. Subbaraman, X. Xu, R. T. Chen, "1xN Multimode Interference Beam Splitter Design Techniques For On-Chip Optical Interconnections," IEEE Journal Of Selected Topics In Quantum Electronics, Vol. 17, No. 3, Pp. 510-515, 2011
11. A. Hosseini, X. Xu, H. Subbaraman, D. Kwong, W. Jiang, And R. T. Chen, "On The Role Of Evanescent Modes And Group Index Tapering In Slow Light Photonic Crystal Waveguide Coupling Efficiency," Applied Physics Letters, Vol. 98, Pp. 031107, 2011
12. A. Hosseini, D. Kwong, Y. Zhang, S. A. Chandorkar, F. Crnogorac, A. Carlson, B. Fallah, S. Bank, E. Tutuc, J. Rogers, R. F. W. Pease, And R. T. Chen, "Three Dimensional Silicon-On-Insulator Based Optical Phased Array For Agile And Large

Angle Laser Beam Steering Systems," Journal Of Vacuum Science And Technology B, Vol. 28, C6o1, 2010

13. A. Hosseini, H. Subbaraman, D. Kwong, Y. Zhang, R. T. Chen, "Optimum Access Waveguide Width For 1xN Multimode Interference Couplers On Silicon Nanomembrane," Optics Letters, Vol. 35, No. 2864-2866, 2010
14. A. Ghaffari, A. Hosseini, X. Xu, D. Kwong, H. Subbaraman, And R. T. Chen, "Transfer Of Micro And Nano-Photonic Silicon Nanomembrane Waveguide Devices On Flexible Substrates," Optics Express, Vol. 18, No. 19, Pp. 20086-2009, 2010
15. A. Hosseini, J. Covey, D. Kwong, And R. T. Chen, " Tapered Multi-Mode Interference Couplers For High Order Mode Power Extraction," Journal Of Optics, Vol. 12, Pp. 075502, 2010
16. A. Hosseini, D. Kwong, C.-Y. Lin, B. S. Lee, And R. T. Chen, "Output Formulation For Symmetrically-Excited One-To-N Multimode Interference Coupler," IEEE Journal Of Selected Topics In Quantum Electronics, Vol. 16, No. 1, Pp. 61-69, 2010
17. A. Hosseini, D. Kwong, And R. T. Chen, "Unequally Spaced Waveguide Arrays For Silicon Nanomembrane-Based Efficient Large Angle Optical Beam Steering," IEEE Journal Of Selected Topics In Quantum Electronics, Vol. 15, No. 5, Pp. 1439-1446, 2009
18. Y. Zhao, Y.-S. Chen, A. Hosseini, D. Kwong And R. T. Chen, "Delay Time Enhanced Flat Band Photonic Crystal Waveguides With Capsule-Shaped Holes On Silicon Nanomembrane," IEEE Journal Of Selected Topics In Quantum Electronics, Vol. 15, No. 5, Pp. 1510-1514, 2009

CONFERENCE PAPERS:

1. D. Kwong, A. Hosseini, Y. Zhang, J. Covey, X. Xu, and R. T. Chen, "Steerable Free Space Optical Interconnect with Corrugated Waveguide Gratings Optically Isolated by 2D Photonic Crystal," to be presented at IEEE Optical Interconnects Conference.
2. D. Kwong, J. Covey, A. Hosseini, X. Xu, Y. Zhang, S. Chakravarty, and R. T. Chen, "Crosstalk Suppression of Corrugated Waveguides in an Optical Phased Array Using 2D Photonic Crystal Slab," to be presented at OSA CLEO.
3. D. Kwong, A. Hosseini, J. Covey, Y. Zhang, R. T. Chen, "Low loss polycrstyalline silicon waveguides and devices for multilayer on-chip optical interconnects," Proc. SPIE 8630, Optoelectronic Interconnects XIII, 863012 (February 27, 2013);
4. D. Kwong, J. Covey, A. Hosseini, Y. Zhang, R. T. Chen, "Feasibility of Multimode Polycrystalline Waveguides/Devices: Record Low Propagation Loss and Uniform 1x12 MMI Fanout," CLEO 2012 Proceedings of the Conference on Lasers and Electro-Optics CM3A.2 (2012)
5. D. Kwong, Y. Zhang, A. Hosseini, and R. T. Chen, "Integrated optical phased array based large angle beam steering system fabricated on silicon-on-insulator," SPIE Photonics West, Proc. SPIE 7943, 79430Y, 2011
6. D. Kwong, Y. Zhang, A. Hosseini, Yazhao Liu, and R. T. Chen, "Demonstration of Rib Waveguide Based 1x12 Multimode Interference Optical Beam Splitter on

Silicon-on-Insulator" IEEE/LEOS summer Topicals Meeting Series, pp. 221-222, 19-21 July 2010
7. D. Kwong, Y.-Z. Liu, A. Hosseini, C.-Y. Lin, B. S. Lee, and R. T. Chen, "Silicon-integrated photonic circuit for a single-stage large-angle beam steering optical phased array," SPIE Photonics West, 7607, 760713, 2010
8. X. Xu, H. Subbaraman, A. Hosseini, D. Kwong, C.-Y. Lin, R. T. Chen, "Stamp Printing of Silicon Nanomembrane Based Flexible Photonic Devices," CLEO 2012 Proceedings of the Conference on Lasers and Electro-Optics CM4A.7 (2012)
9. Y. Zhang, A. Carlson, S. Y. Yang, A. Hosseini, D. Kwong, J. Rogers, R. T. Chen, "Double-layer Photonic Devices Based on Transfer Printing of Silicon Nanomembranes for Three-dimensional Photonics,"CLEO 2012 Proceedings of the Conference on Lasers and Electro-Optics CTu1A.5 (2012)
10. Y. Zhang, A. Hosseini, J. Ahn, D. Kwong, B. Fallahazad, E. Tutuc, R. T. Chen, "Double-layer 1x12 Multimode Interference Coupler for Three-dimensional Photonic Integration," IEEE Optical Interconnects Conference, paper TuD4, 2012
11. A. Hosseini, B. FallahAzad, D. Kwong, E. Tutuc, and R. T. Chen, "A Platform for Three-dimensional On-chip Photonics," OSA CLEO:2011 - Laser Applications to Photonic Application, paper CThHH5, 2011
12. A. Hosseini, X. Xu, D. Kwong, H. Subbaraman, and R. T. Chen, "On the Mechanism of Efficient Coupling into Slow Light Photonic Crystal Waveguides," OSA Quantum Electronics and Laser Science Conference (QELS), paper JTuI4, 2011
13. (Invited) A. Hosseini, D. Kwong, Y. Zhang, and R. T. Chen, "Large Angle Beam Steering on Silicon Nanomembrane," IEEE Winter Topicals (WTM), 2011 IEEE , vol., no., pp.111-112, 2011
14. A. Hosseini, D. Kwong, Y. Zhang, and R. T. Chen, "Far-field approximation in two-dimensional slab-waveguides," SPIE Photonics West, Proc. SPIE 7943, 79430N, 2011
15. A. Hosseini, D. Kwong, H. Subbaraman, and R. T. Chen, "Demonstration of Compact 2x2 Multimode Interference coupler on Silicon Nanomembrane, IEEE Group IV Photonics GPF 2010, Beijing, P1.25, 2010
16. A. Hosseini, D. Kwong, and R. T. Chen, "On the Design of 1xN Multimode Interference Coupler for Photonic Integrated Circuits", IEEE/LEOS summer Topicals Meeting Series, pp. 195-196, 19-21 July 2010
17. A. Hosseini, D. Kwong, Y. Zhang, Yazhao Liu, and R. T. Chen, "On the Optimum Design for 1xN Multimode Interference Coupler based Beam Splitters," OSA/IEEE Integrated Photonics Research, Silicon and Nano Photonics (IPR), paper JTuB9, 2010
18. A. Hosseini, D. Kwong, Yazhao Liu, and R. T. Chen, "On the Design of Highly Dispersive Photonic Crystal Waveguides for Optical Delay Lines," IEEE/LEOS Winter Topicals Meeting Series, pp.120-121, 2010
19. A. Hosseini, D. Kwong, and R. T. Chen, "Analytical formula for output phase of symmetrically excited one-to-N multimode interference coupler," SPIE Photonics West, 7607, 760718, 2010

20. A. Hosseini, D. Kwong and R. T. Chen, “Low dispersion slow light in silicon-on-insulator photonic crystal waveguide,” SPIE Photonics West, 7609, 76091A, 2010
21. Y.-S. Chen, A. Hosseini, Y. Zhao, D. Kwong and R. T. Chen, “Modified Slab Photonic Crystal Structure for Delay Time Enhancement Using Capsule Shaped Holes”, 14th IEEE OptoElectronics and Communications Conference (OECC), 2009
22. A. Hosseini, D. Kwong and R. T. Chen, “Wide steering angle optical phased array based on silicon nanomembrane,” SPIE Photonics West, 7221, 72210T, 2009
23. A. Hosseini, Y.-S. Chen, D. Kwong and R. T. Chen “Silicon nano-membranes for efficient large angle optical beam steering,” IEEE/LEOS Winter Topicals Meeting Series, pp. 104-105, 2009